

Study of the X-ray Spectral Components in Narrow-Line Seyfert 1 Galaxies

Hiroaki TAKAHASHI

2013/02/26

Department of Earth and Space Science,
Graduate School of Science,
Osaka University, Japan

Abstract

We study Suzaku observations of Narrow Line Seyfert 1 Galaxies (NLS1s). Among the various X-ray spectral components in radio quiet Active Galactic Nuclei (AGNs), our main interest is its primary emission, i.e., power-law component and soft thermal emission from accretion disk. NLS1s could be good example of high accretion state of SMBHs.

We first present the results from Suzaku observation of the luminous NLS1, Ton S180. We obtained wide-band (0.25–55 keV) X-ray spectra for the first time and found the broad iron K line centered at 6.7 keV. We reproduced the soft X-ray excess component with a combination of the reflection model and the disk blackbody model. The inner disk temperature is obtained as 75 eV, which is much lower than previously considered, and a general problem that the disk temperature derived from a soft X-ray excess is too high is reconciled, at least in this source.

We next study three hard X-ray bright NLS1s with Suzaku. Measurement of the high energy cutoff in a power-law component is the aim of our observations. Among three, Mrk 110 and SWIFT J212745.6+565636 show the cutoff energies of 10–50 keV, which is significantly smaller than typical values of 100–300 keV for BLS1s, although IGR J16185–5928 in our sample show a cutoff energy higher than 240 keV. We show a trend that NLS1s (high accretion rate sources) have lower cutoff energies, i.e., electron temperatures of accretion corona, than BLS1s. In the framework of thermal Comptonization in a corona, this is interpreted as shorter cooling time at higher accretion rate.

We then perform quasi-simultaneous radio, optical, and X-ray observations of the radio loud NLS1 RX J1633+4718. The X-ray spectra are explained with two components; one is soft X-ray thermal component and the other is a power law component but with a cutoff energy of 3–5 keV. The former component and optical emission are simultaneously reproduced with a p -disk model of $p \sim 0.5$, which represents a slim disk. The luminosity of this component is super Eddington as is seen in some ULX sources, but for the first time in AGNs. On the other hand, the power-law with a cutoff component is difficult to explain with a Synchrotron self-Compton (SSC) model unless electrons are mono-energetic. We hence interpret this component with thermal Comptonization

in a corona, but with extremely low electron temperature. We speculate this source is an extreme case of NLS1 (i.e. high accretion rate) class. In this source reflection component is not apparent and the thermal disk component is observed in its bare form. These might be related the production of jets in this source.

These X-ray (and partly optical and radio) observations of NLS1s sources provide unique opportunity to study SMBH at high accretion rate.

Contents

1	Introduction	8
2	Review of Active Galactic Nuclei	10
2.1	Active Galactic Nuclei and Super Massive Black Hole	10
2.2	Classification of AGNs	11
2.2.1	Radio Quiet AGNs and Radio Loud AGNs	11
2.2.2	Seyfert Galaxies	12
2.2.3	Narrow Line Seyfert 1 Galaxies	13
2.3	X-ray Emission of AGNs	14
2.3.1	Power-Law Component and High Energy Cutoff in X-ray spectra of AGNs	15
2.3.2	Soft X-ray Excess of AGNs	16
2.3.3	X-ray Properties of NLS1s	17
2.4	Accretion Disk and Corona	18
2.4.1	Mass of SMBHs	19
3	Suzaku Observation of the Narrow Line Seyfert 1 Ton S180	21
3.1	Introduction	21
3.2	Observation & Data Reduction	24
3.3	Time Averaged Spectra	26
3.3.1	Hard X-ray Excess	28
3.3.2	Soft X-ray Excess	30
3.4	Variability Analysis	32
3.4.1	Light Curve	32
3.4.2	RMS Fractional Variability	32
3.4.3	Spectral Variability	33
3.5	Discussion	34
3.5.1	Long Term Variability and Eddington Ratio	34

3.5.2	Reflection Component and Soft X-ray Excess	35
3.5.3	Absorbers, Reflectors, and Primary Source	38
3.6	Summary	41
4	The Hard X-ray emission in Narrow Line Seyfert 1 Galaxies: Mrk 110, SWIFT J212745.6+565636, and IGR J16185–5928	50
4.1	Introduction	50
4.2	Observations	52
4.3	Spectral Analysis	54
4.3.1	2.5–12 keV X-ray Spectrum	54
4.3.2	2.5–40 keV X-ray Spectrum	54
4.3.3	0.25–40 keV X-ray Spectrum	55
4.4	Discussion	56
4.5	Summary in 3 NLS1s	63
5	Radio Loud Narrow-Line Seyfert 1 Galaxy RX J1633+4718	91
5.1	Introduction	91
5.2	Observation	94
5.2.1	X-ray	94
5.2.2	Radio	96
5.2.3	Near Infrared and Optical	97
5.3	Spectral Analysis	98
5.3.1	X-ray spectral analysis with Suzaku	98
5.3.2	From Infrared to Optical	100
5.4	Discussion	101
5.4.1	Less variable component from near infrared to soft X- ray band	101
5.4.2	Variable component in the X-ray band	103
5.4.3	Contribution of the thermal bremsstrahlung	105
5.4.4	What makes the X-ray spectra of RL-NLS1 RX J1633+4718 unique ?	105
5.5	Summary in RX J1633+4718	106
6	Summary	124
6.1	Future Prospects	127

List of Figures

3.1	Data/Model ratio in the 0.25–55 keV band of Ton S180	42
3.2	Fe band profile of Ton S180	42
3.3	The spectral fit to the 4–55 keV energy band of Ton S180	43
3.4	Time averaged (0.25–55 keV) Suzaku spectra of Ton S180 including the disk blackbody model	44
3.5	Time averaged (0.25–55 keV) Suzaku spectra of Ton S180 including the second power-law model	44
3.6	Time averaged (0.25–55 keV) Suzaku spectra of Ton S180 including the cutoff power-law model	45
3.7	Time averaged (0.25–55 keV) Suzaku spectra of Ton S180 including the Comptonized blackbody model	45
3.8	The light curve in the 0.2–12 keV and 15–40 keV	46
3.9	The RMS fractional variability of Ton S180	46
3.10	Comparison of TZ1 spectra (red) and TZ2 spectra (blue)	47
3.11	X-ray flux of Ton S180 measured in 1990–2006	47
3.12	0.25–55 keV X-ray spectra and reflection component model	48
4.1	The raw image of Mrk 110	64
4.2	HXD-PIN 12–70 keV spectra of 3 NLS1s	65
4.3	Data/Model ratios of 3 NLS1s	66
4.4	The Fe band profiles of 3 NLS1s	67
4.5	The 2.5–40 keV spectral fit of Mrk 110	68
4.6	The 2.5–40 keV spectral fit of SWIFT J212745.6+565636	69
4.7	The spectral profile of SWIFT J212745.6+565636 in the Fe band	69
4.8	The 0.25–40 keV X-ray spectra and the models extrapolating to lower energy band	70
4.9	The 0.25–40 keV X-ray spectrum and the best-fit model of Mrk 110 (1)	71

4.10	The 0.25–40 keV X-ray spectrum and the best-fit model of Mrk 110 (2)	72
4.11	The contour of reflection fraction R versus E_C of Mrk 110	72
4.12	The contour of E_C versus Γ of Mrk 110	73
4.13	The contour of optical depth τ versus electron temperature kT_e of Mrk 110	73
4.14	The 0.25–40 keV X-ray spectrum and the best-fit model of SWIFT J212745.6+565636	74
4.15	The contour of reflection fraction R versus E_C of SWIFT J212745.6+565636	74
4.16	The contour of E_C versus Γ of SWIFT J212745.6+565636	75
4.17	The contour of optical depth τ versus electron temperature kT_e of SWIFT J212745.6+565636	75
4.18	The 0.25–40 keV X-ray spectrum and the best-fit model of IGR J16185–5928	76
4.19	The contour of reflection fraction R versus E_C of IGR J16185–5928	76
4.20	The contour of E_C versus Γ of IGR J16185–5928	77
4.21	The contour of optical depth τ versus electron temperature kT_e of IGR J16185–5928	77
4.22	The typical SED of NLS1 and BLS1	78
4.23	Electron temperature versus photon index of Seyfert 1 galaxies (1)	78
4.24	Electron temperature versus Eddington ratio of Seyfert 1 galaxies (1)	79
4.25	Optical depth versus Eddington ratio of Seyfert 1 galaxies (1)	80
4.26	Compton y parameter versus Eddington ratio of Seyfert 1 galaxies (1)	81
4.27	Electron temperature kT_e versus luminosity ratio (1)	82
4.28	Electron temperature kT_e versus luminosity ratio (2)	83
5.1	The polarization of RX J1633+4718	107
5.2	The SDSS image of RX J1633+4718.	107
5.3	The 1st Suzaku XIS spectral profile of RX J1633+4718	108
5.4	The spectral profiles of RX J1633+4718	108
5.5	The spectra in the 0.25–12 keV and the best fit model	109
5.6	The overplot of RX J1633+4718 X-ray spectra	110

5.7	90% confidence contours for the disk inner radius versus the disk inner temperature	110
5.8	90% confidence contours for the cutoff energy E_C versus the photon index Γ	111
5.9	Near infrared to Optical SED of RX J1633+4718	111
5.10	Near-infrared to optical spectra of RX J1633+4718 with/without the galactic extinction	112
5.11	SDSS spectrum of RX J1633+4718	112
5.12	Near infrared to optical SED of SDSS J163323.53+471902.7	113
5.13	Far infrared to optical SED of RX J1633+4718	113
5.14	Radio to X-ray SED of RX J1633+4718	114
5.15	Near infrared to optical RX J1633+4718 nucleus spectrum	114
5.16	Optical to X-ray SED of RX J1633+4718 and blackbody (1)	115
5.17	Optical to X-ray SED of RX J1633+4718 and blackbody (2)	115
5.18	Optical to X-ray SED of RX J1633+4718 and blackbody (3)	116
5.19	Radio to X-ray SED of RX J1633+4718 and SSC model (1)	117
5.20	Radio to X-ray SED of RX J1633+4718 and SSC model (2)	118
5.21	The result of the spectral fit using 2 compTT model and disk blackbody model	119
6.1	Electron temperature versus photon index of Seyfert 1 Galaxies (2)	128
6.2	Electron temperature versus Eddington ratio of Seyfert 1 galaxies (2)	129
6.3	Compton y parameter versus Eddington ratio of Seyfert 1 galaxies (2)	130
6.4	Optical depth versus Eddington ratio of Seyfert 1 galaxies (2)	131
6.5	Electron temperature versus luminosity ratio (2)	132

List of Tables

3.1	The best-fit parameters of Ton S180 in the 0.25-55 keV band	49
4.1	The Suzaku NLS1 sample	84
4.2	The HXD-PIN count rates in the 15-40 keV band	84
4.3	2.5–12 keV spectral fit	84
4.4	2.5–40 keV spectral fit	85
4.5	0.25–40 keV spectral fit of Mrk 110	85
4.6	The best-fit parameter of Mrk 110 0.25–40 keV spectral fit	86
4.7	The best-fit parameter of SWIFT J2127.4+5654 0.25–40 keV spectral fit.	86
4.8	The best-fit parameter of IGR J16185–5928 0.25–40 keV spectral fit.	86
4.9	The observational parameters of 3 NLS1s	87
4.10	The observational parameters of referenced Seyfert 1 galaxies	88
4.11	The mean and weighted mean of kT_e , y , and τ	89
4.12	The input parameters of typical SED.	89
4.13	The list of central BH mass and luminosity	90
5.1	Suzaku observation log of RX J1633+4718	120
5.2	VLBI observation log of RX J1633+4718	120
5.3	Kanata observation log of RX J1633+4718	120
5.4	Kanata observation results	120
5.5	The galactic extinction determined in Schlafly & Finkbeiner (2011)	121
5.6	Near infrared to Optical flux of SDSS J163323.53+471902.7.	121
5.7	Spectral fit in the 0.25–12 keV band	122
5.8	The best-fitting parameters in the 0.25–12 keV band using p -free disk model	122
5.9	Parameters used to the models described in figure 5.19.	123

5.10	Parameters used to the models described in figure 5.20.	123
5.11	The best-fit parameters of the 2 Comptonization models and the disk blackbody model	123
6.1	The mean and weighted mean of kT_e , y , and τ for NLS1s and BLS1s.	127

Chapter 1

Introduction

Active galactic nuclei (AGN) is one of the most energetic objects in the Universe. The energy emitted by the nuclear source within 100 pc of the galaxy is 10^{11} times as luminous as the solar luminosity ($L_{\odot} = 3.8 \times 10^{33} \text{ erg s}^{-1}$). AGN host a super massive black hole (SMBH) at its center, of which mass is 10^{6-9} times as heavy as the solar mass ($M_{\odot} = 1.989 \times 10^{33} \text{ g}$). The radiation of AGN is released from material accreting onto the SMBH. Measurements of gas and stellar kinematics have shown that most galaxies have a SMBH hole at their center. These SMBH must be AGN some time ago. AGN are hence not only the target of study on accretion physics but also that on cosmological evolution of SMBH and their host galaxies.

In general, the AGN phenomenon is observed over a wide range from radio to X-ray. The X-ray flux has not only a significant fraction (5 – 40%) of the bolometric emission but also rapid variability thought to arise very close to the active nucleus. Thus the X-ray band is important coverage to study the accretion onto the SMBH. Although the X-ray emission region is too small to image with current instrumentation, spectroscopy and timing analysis offer ways to probe these regions indirectly. X-ray data includes not only the signature of the gas inflow and outflow at the heart of the accretion onto the SMBH but also the signatures of reprocessing in material within a few gravitational radii and the accretion disk at the vicinity of the SMBH.

In the case of Seyfert 1 galaxy, the X-ray spectrum is roughly approximated with a power-law model. This component has an energy cutoff around a few tens keV and thought to be the inverse Compton scattering with the low energy photons and the high energy electrons. In the case of the Seyfert 1 galaxy, the cutoff energy is estimated to be 230 keV (Dadina, 2008). However, there are a small sample that the cutoff energies are constrained significantly.

One of the main theme in this thesis is to measure the cutoff energies for narrow line Seyfert 1 galaxies (NLS1s), which are considered to have higher accretion rate than for broad line Seyfert 1 galaxies (BLS1s),

In 1985, Arnaud et al. (1985) reported that the excess component from the power-law below 1 keV was detected in Mrk 841. This component is so-called "soft X-ray excess". This excess is particularly prevalent in NLS1s (Boller et al., 1996). In the past the soft excess had often been associated with the high-energy tail of the thermal emission of the disk, but it was recently argued that the temperature of the disk should be nearly constant ($kT \sim 0.1 - 0.2$ keV), regardless of the mass and luminosity of the AGN (Gierliński & Done, 2004). This result implies that some other mechanism is at work, as the temperature of the disk should depend on both the mass of the BH and the accretion rate. Several models have been brought forward in order to explain the soft excess observed in the X-ray band. However, the origin of the soft X-ray excess has been still an open issue. In this thesis, we study the NLS1s in which the soft X-ray excess is prominent. We employ Suzaku for the X-ray observations of the NLS1s in this thesis. Suzaku is the fifth Japanese X-ray astronomy satellite launched on July 10, 2005. The main instruments of Suzaku are the X-ray Imaging Spectroscopy (XIS; Koyama et al. (2007)) and the Hard X-ray Detector (HXD; Takahashi et al. (2007)). The former covers the 0.2–12 keV range with 3 front-illuminated (FI) CCDs and 1 back-illuminated (BI) ccd. The latter covers the 12–500 keV with silicon PIN diodes and GSO well-type Phoswich counter. Since the X-ray spectrum of AGN has some characteristics from a few ten eV to a few hundred keV, Suzaku is able to observe simultaneously this important band with lower background level than previous satellites.

This thesis is organized as follows. In the next chapter, we briefly review AGN, in particular, Seyfert 1 Galaxy (Sy1) and its subclass Narrow Line Seyfert 1 Galaxy (NLS1) and their X-ray spectral components. In chapter 3, 4, and 5, we present the individual observations, analyses, results and discussions for Ton S180, 3 NLS1s (Mrk 110, SWIFT J212745.6+565636, IGR J16185–5928), and RX J1633+4718, respectively. The summary and conclusions of this thesis is described in chapter 6.

Chapter 2

Review of Active Galactic Nuclei

In this section, we shortly review active galactic nuclei (AGN) and their X-ray emissions. This could include vast range of topics, and number of text books (e.g. Peterson (1997); Beckmann & Shrader (2012)) and reviews (e.g. Turner & Miller (2009)) are available. We hence focus on the topics directly related to our studies in this paper, i.e., narrow line Seyfert 1 (NLS1) galaxies among various classes of AGNs, and a soft X-ray excess and a hard X-ray cutoff among spectral features observed in the X-ray spectra of AGN.

2.1 Active Galactic Nuclei and Super Massive Black Hole

Carl Seyfert, in 1940's, first found some galaxies host additional strongly emitting component in their center, which are now called as active galactic nuclei (AGN) (Seyfert, 1943). He obtained optical spectra of those galaxies, showing high-excitation emission lines from the nuclear region superposed on a normal star-like spectrum (Seyfert, 1943). It was not until 1960's when the nature of the AGNs was regarded as accretion of matters onto a super massive black hole (SMBH). This idea was originally proposed to account for huge radiation energy emitted from compact regions. Evidence supporting this SMBH hypothesis has been accumulated by measurements of the motions of stars and gases at the center of galaxies, not only in active ones but also in normal ones.

It is widely believed that almost all the galaxies host a SMBH ($10^5 - 10^{10} M_{\odot}$) in their center (Salpeter, 1964; Zel'dovich & Novikov, 1964; Lynden-Bell, 1969). For example, our Galaxy has a SMBH of $2.6 \times 10^6 M_{\odot}$ (Reid et al.,

1999). Its luminosity is about 10^{-9} of its Eddington limit, while there is a suggestion that the SMBH was very active hundreds years ago (Koyama et al., 1996). Number density of luminous AGNs, i.e., quasars peaks at redshift of $z \sim 2-3$, suggesting they were growing rapidly at that time and remain as dormant SMBHs in the present day Universe. The growth of SMBHs is at least partly due to accretion processes in these activities. Nevertheless, their origin is still an open question, one of the most important ones in present-day astronomy. On this point, there found a tight correlation between the mass of SMBHs and the velocity dispersion of their host galaxies, known as the $M_{BH}-\sigma$ relation (*e.g.* Ferrarese & Merritt (2000); Gebhardt et al. (2000); Merritt & Ferrarese (2001); Tremaine et al. (2002); Ferrarese & Ford (2005); Graham (2008); Gültekin et al. (2009)). This suggests that the origin of SMBHs should have close relation to those of galaxies regardless of difference in their scale by orders of magnitudes.

2.2 Classification of AGNs

Emission from AGNs ranges over wide wave-length band, radio to γ -rays. Since observational properties in each wave-length band are used solely or mutually as clues to classify AGNs, a lot of classification scheme are present for AGNs, as described in the text books Peterson (1997); Beckmann & Shrader (2012). Note that the clues of the classifications are not only based on different aspects of observational properties but also not necessarily well defined. Furthermore, there are exceptional sources as for any other classifications. Therefore, one AGN can belong to various AGN classes depending on literature.

2.2.1 Radio Quiet AGNs and Radio Loud AGNs

Radio loudness is usually defined as $R = f_{5\text{GHz}}/f_{2500\text{\AA}}^\circ$, where $f_{5\text{GHz}}$ is the radio flux at 5GHz and $f_{2500\text{\AA}}^\circ$ is the optical flux at 2500 \AA , $f_{2500\text{\AA}}^\circ$ is sometimes replaced with the flux at different wave length (*e.g.* X-rays). Radio loud AGNs (*e.g.* $R > 10$) typically have large (up to Mpc) scale jet structures. Among them, the sources of which jets are oriented toward us are called blazars and are characterized with smooth non-thermal continuum spectral energy distributions (SEDs) from radio to TeV γ -rays.

On the other hand, the SED of radio quiet AGNs is rather complex and consists of many components. In addition to the fact that radio emission is weak, by its definition, high energy γ -rays are seldom detected in the radio quiet AGNs. This suggests contribution of relativistic electrons, which play important role in the radio loud AGNs, is small. The origin of relatively clear difference between radio loud AGNs and radio quiet AGNs is one of the important unresolved issues in AGN study, although the spin of SMBH is sometimes claimed for it as a key parameter.

2.2.2 Seyfert Galaxies

Seyfert galaxies were the first AGNs, to be precise, galaxies hosting AGNs, identified as such. As mentioned above, galaxies in this class are characterized with a bright core and high-excitation emission lines from it. According to the spectra of high-excitation emission lines, Seyfert galaxies are classified into type 1 and type 2. In the type 1 objects, Balmer lines (H_α , H_β , and H_γ , etc.) are broader (typically thousands km/s) than forbidden lines such as [OII], [OIII], which are typically have line width of hundreds km/s. On the other hand, the type 2 objects show similar line width for both lines, typically hundreds km/s.

The difference between the type 1 and type 2 Seyfert galaxies are interpreted in so called the unified scheme of Seyfert galaxies (or AGNs, Urry & Padovani (1995)). The emission lines are assumed to come from two kinds of regions, broad line regions (BLRs) and narrow line regions (NLRs). The BLRs are closer to the SMBH, typically $10^{-3} - 1$ pc, and their gas density is higher, while the distance to the NLRs is typically 100 pc and their density is low enough for the forbidden lines can be emitted from. Emission lines both from the BLRs and the NLRs are the type 1, while those only from the NLRs are observed in the type 2. In the unified scheme of Seyfert galaxies, a molecular torus is assumed to cover the central engine surrounding a SMBH, and the BLRs reside inside the torus while the NLR outside. Evidence of this view was clearly presented by polarimetry observations of NGC 1068, prototypical Type 2, by Antonucci & Miller (1985). They detected broad lines in the spectrum of the polarized light which represents scattered light. X-ray observations put forward this scheme further (e.g. Awaki et al. (1991)) followed by lots of observational evidence. This unified scheme is now widely believed, while debates are still continuing. In the simplest form of the unified scheme,

the difference between the type 1 and 2 is only due to the viewing angle from observers. There might be intrinsic difference in the central engine between that of the type 1 and type 2. Extensive studies have been made to test this scheme (e.g. Singh et al. (2011); Kazanas et al. (2012)).

Note that Seyfert galaxies are usually radio quiet. It does not mean radio silent. Small jet like structures or evidence of outflow are found at least in some Seyfert galaxies (Doi et al. (2007); Gu & Chen (2010); Doi et al. (2011)).

2.2.3 Narrow Line Seyfert 1 Galaxies

The sub set of Seyfert 1 galaxies of which H_β line width is relatively narrow is called as narrow line Seyfert 1 (NLS1) galaxies. Typical definition of the NLS1 is as follows (Osterbrock & Pogge, 1985):

1. the width (FWHM) of H_β line is less than 2000 km/s
2. the ratio of line intensity $[OIII]/H_\beta$ is less than 3

The NLS1 class can be described as the sources in which the widths of the emission lines from BLR are relatively narrow. As this notation is a little confusing, the term BLR and NLR might better be replaced with High Density Regions (HDR) and Low Density Regions (LDR). We, however, adopt the standard terminology here. The Seyfert 1 galaxies of which width (FWHM) of H_β line is greater than 2000 km/s are called broad line Seyfert 1 (BLS1) galaxies. Fraction of NLS1s among Seyfert 1 galaxies is 46% for soft X-ray selected sample (Grupe & Mathur, 2004), and 19% for optically selected sample (Xu et al., 2007).

The sub class NLS1 had not been extensively focused before their distinctive X-ray properties are found by Boller et al. (1996), who systematically studied soft X-ray properties of the NLS1s with the ROSAT. We will shortly summarize the X-ray properties of the NLS1s separately in the following. Those X-ray properties together with results from other attempts (e.g., SMBH mass estimation through M - σ relation, empirical relation between the line width and the SMBH mass) suggests that the NLS1s have lower mass ($M_{BH} \sim 10^{6-7} M_\odot$) and higher accretion rate ($L_{bol}/L_{Edd} \sim 1$) SMBHs than BLS1s (e.g. concisely reviewed by Komossa & Xu (2007)), though extensive studies are still in process on this issue.

On the other hand, the answer to the question why the BLR line widths in NLS1s are narrower than those in BLS1s has not yet been established.

One possibility is inclination effect, i.e., NLS1 might have a pole-on geometry orbits of BLR clouds viewed from observers. The several attempts so far made suggest the inclination is not the major cause of various unique properties of NLS1s, but it is not clear whether the small SMBH masses can solely explain the narrow line widths or not (see Komossa & Xu (2007)).

One thing we should note here is the detection of several radio loud NLS1s in GeV γ -rays. Most of the GeV γ -ray extragalactic sources detected with the Fermi LAT are blazars, as expected. On the other hand, recent detection of several radio loud NLS1s had been unexpected. Since NLS1s (and Seyfert galaxies in general) are usually radio quiet, radio loud ones are rare, observational properties of radio loud NLS1s hence have not yet established. However, the radio loud NLS1s may demonstrate special phase (or geometry) of the NLS1 activity. We will study one of radio loud NLS1 in chapter 5, in which strange X-ray spectra are obtained.

2.3 X-ray Emission of AGNs

Several years after the beginning of X-ray astronomy, X-rays from the AGNs, Cyg A and M87, were detected (Buram et al.1966). In the first X-ray all sky survey with the Uhuru satellite a dozens of AGNs were detected (Forman et al., 1978), among nearly 340 sources listed in the 4th Uhuru catalog. X-ray imaging instruments, first systematically employed in the Einstein satellite launched in 1979, revealed that significant fraction of the cosmic X-ray background is resolved into X-ray sources. Recent Chandra observations with long exposures indicate that more than 80% of the CXB is resolved into discrete sources, predominantly AGNs. It means that the X-ray sky is dominated by AGNs.

X-ray spectra of AGNs were approximated with a simple power law with photon index of 1.68 ± 0.15 (e.g. Mushotzky (1984)). However, there found various spectral features on the power law continuum since 1980's thanks to new instruments with better energy resolution and higher sensitivity. The spectral features include absorptions in various forms (cold absorber, partial absorber, warm absorber), a soft X-ray excess, iron K lines, a hard X-ray hump, and so on.

Among these, iron K lines are interpreted as fluorescent X-rays by irradiation of power law continuum to matter surrounding a SMBH, for example, an

accretion disk or torus. Therefore, iron K lines and their associated continuum have been employed as an excellent tool to diagnose the matter and geometry surrounding a SMBH (e.g. Awaki et al. (1991), Tanaka et al. (1995)). In particular, broad iron K lines are one of the most important evidence of strong gravity expected for a SMBH. This line of studies are extensively pursued with Suzaku and other currently available X-ray satellites. The interpretation of the iron K lines and their associated continuum is, however, also a topic of extensive debates, and alternative interpretations have been proposed. Absorption features are also useful to investigate the amount and status of matter surrounding a SMBH.

X-ray emission from AGNs show variability of various time scales and amplitude. The X-ray variability is usually more prominent than that in longer wave length bands, most likely reflecting phenomena occurring at the vicinity of a central SMBH. Therefore, study of the X-ray variability is as important as X-ray spectral analysis. Sometimes spectral change is observed in accordance with intensity increase or decrease, from which additional information on the X-ray emission region and its surroundings can be extracted.

2.3.1 Power-Law Component and High Energy Cutoff in X-ray spectra of AGNs

Primary (or intrinsic) X-ray emission from the vicinity of the SMBH in (radio quiet) AGNs is usually assumed to be a simple power law with a high energy cutoff. Note that X-ray spectra observed are not a simple power law, since spectral features mentioned above are imprinted on and added to it. The photon index of the power law ranges $\Gamma \sim 1.5 - 2.0$, though it depends on sources, their states and also on the models of secondary emissions (e.g. reflection component) and absorption assumed. Hard X-ray to soft γ -ray observations of some bright radio quiet AGNs showed the spectra have a cutoff at 100-300 keV (e.g. Zdziarski et al. (2000); Petrucci et al. (2001); Dadina (2008)). This result leads to a widely adopted interpretation that the power law component is generated in an accretion corona of which temperature is tens to hundreds keV through inverse Compton scattering of soft photons from optically thick accretion disk.

In recent X-ray studies of radio quiet AGNs, attention is primarily paid to the diagnostic of the matter and geometry around a SMBH, and not necessarily as much to the origin of the *intrinsic* power-law. This is partly

due to the difficulty in measuring high quality spectra at hard X-ray band in many sources. One of the aims of our study is to extract the power-law component and its high energy cutoff for NLS1 sources, as will be shown in the chapter 4.

2.3.2 Soft X-ray Excess of AGNs

As mentioned above, the X-ray spectra of AGNs were reproduced with a simple power law of $\Gamma \sim 1.5 - 2.0$. However, Historically, the soft X-ray excess was first noted in observations of AGNs with the EXOSAT (Arnaud et al., 1985). Later, NLS1 galaxies are identified to show distinctive soft X-ray components. That trend was first expressed as anti correlation between soft X-ray slope and the H_β width in Boller et al. (1996).

There found a bump at UV band in the SED of AGNs, called as UV bump. The UV bump is considered to be thermal emission from an accretion disk of AGNs. In fact, assuming optically thick standard disk model (Shakura & Sunyaev, 1973) for a SMBH of $10^8 M_\odot$ radiating at its Eddington limit, the temperature at the disk inner radius is 2.1×10^5 K, which corresponds to the UV emission. Therefore, authors first tried to explain the soft X-ray excess as the high energy end of the thermal emission from an accretion disk. One of the difficulty in this model is the temperature is too high for the SMBH. If we employ multi-color-disk model (diskbb), the temperatures distribute in very narrow range around 200 eV (Gierliński & Done, 2004), while expected temperature of the disk inner radius is 6.8×10^5 K even for a $10^6 M_\odot$ SMBH. Another difficulty of this interpretation is the narrowness of the temperature range observed. There should be larger scatter reflecting SMBH mass and/or accretion rate.

Sophistication of the accretion disk model so as to solve this discrepancy has been extensively pursued (e.g. Mineshige et al. (2000)). In parallel, alternative interpretations for the soft X-ray excess have been proposed. If the spectral shape of the soft X-ray excess is predominantly determined by atomic physics not accretion disk temperature, it account for the canonical spectral shape observed. One of such alternative interpretations is a possibility that the soft X-ray excess component can be a collection of emission lines, such as thin thermal emission from hot plasma, that cannot be resolved with low energy resolution instruments. Nevertheless, high resolution spectroscopy with grating instruments rejected this possibility at least in some sources

(Mrk 478, NGC 5548, Marshall (1994)); the soft X-ray excess is a smooth continuum with some absorption features.

Another alternative model is the reflection model (George & Fabian, 1991), in which soft X-ray excess is reflection component from a irradiated disk and extremely blurred by its rotation around a SMBH. This model has succeeded in reproducing the soft X-ray excess and the broad iron K line at the same time at least for some sources (Crummy et al., 2006). In fact, we will show that including this model the soft X-ray excess of Ton S180 is explained. Another interpretation in which outflowing absorber is employed was proposed by Middleton et al. (2007), though detailed spectral analysis showed difficulty in reproducing the observed spectra (Miniutti et al., 2009b).

2.3.3 X-ray Properties of NLS1s

As mentioned above, NLS1s form a subclass of Seyfert 1 galaxies classified with their optical emission line properties and they are distinguished from typical BLS1s. The X-ray properties of NLS1 are of particular interest. Boller et al. (1996) systematically analyzed 46 NLS1s with ROSAT observation and found that most of them have the steep soft X-ray slope (from ~ 1.6 to ~ 5). Leighly (1999a,b) analyzed 23 NLS1s with ASCA observation and found that the hard X-ray photon index is steeper at more than 90% confidence in this sample of NLS1s compared with that of BLS1s. They also reported that the soft X-ray excess emission was detected in 17 of 19 objects that had no significant absorption and approximated with a blackbody model of $kT \sim 100 - 200$ eV, a result that demonstrates that soft X-ray excess appear considerably more frequently in NLS1s than BLS1s. From the results of the steep photon index and the strong soft X-ray excess, there were suggestions that NLS1s resemble the fastest accreting states (high states) of X-ray binaries (Pounds et al., 1995). NLS1s also show the rapid and large amplitude time variability (Boller et al., 1996; Leighly, 1999a). The rapid X-ray variability of the NLS1s sometimes lead to the hypothesis that the NLS1s have lower mass BH than the BLS1s (Hayashida, 2000; Wang & Lu, 2001; Kawaguchi, 2003). The iron line equivalent width appears to be similar among NLS1s and BLS1s (from 100 eV to 1.3 keV). This could mean that reprocessing occurs with similar geometry in both classes of objects (Leighly, 1999b). For the hard X-ray observation, Panessa et al. (2011) studied a sample of 14 NLS1s selected at hard X-ray ($E > 20$ keV) from the fourth INTEGRAL/IBIS catalog and

reported that the 20–100 keV spectra show hard X-ray photon indices flatly distributed (Γ_{20-100} ranging from ~ 1.3 to ~ 3.6) with an average value of $\langle \Gamma_{20-100} \rangle = 2.3 \pm 0.7$, compatible with a sample of hard X-ray BLS1 average slopes ($\langle \Gamma_{20-100} \rangle = 2.0 \pm 0.2$). In addition, they confirmed that the fraction of NLS1s in the hard X-ray sky is likely to be $\sim 15\%$, in agreement with estimates derived in optically selected NLS1 samples ($\sim 19\%$, Xu et al. (2007)) and that the association of NLS1s with small black hole masses with a peak at $10^7 M_\odot$ in the distribution, however, hard X-ray NLS1s seem to occupy the lower tail of the Eddington ratio distribution of classical NLS1 galaxies.

2.4 Accretion Disk and Corona

Extensive theoretical and computational studies have been made on accretion phenomena onto black holes, stellar mass BHs and SMBHs. They are beyond the scope of the review here, and should be referred to textbooks (e.g. Kato et al. (2008)). We briefly mention widely accepted view of an accretion disk and a corona in AGNs.

As mentioned above, the standard optically thick geometrically thin accretion disk by Shakura & Sunyaev (1973), is accounted for the optical to UV bump emission as a baseline. The temperature at the inner radius of the standard accretion disk is expressed as

$$T = \left(\frac{3}{8\pi\sigma} \frac{GM_{\text{BH}}\dot{M}}{r^3} \right)^{1/4} \left(1 - \frac{r_{\text{in}}}{r} \right)^{1/4} \quad (2.1)$$

where M_{BH} is the black hole mass, \dot{M} is the mass accretion rate, r_{in} is the disk inner radius, and σ is the Stefan-Boltzmann constant, respectively. Note that the innermost stable orbit is $6 r_g$ for a non-rotating BH, and $1.23 r_g$ for an extreme Kerr BH. The luminosity of the disk is expressed as

$$L_{\text{disk}} = 4\pi r_{\text{in}}^2 \sigma T_{\text{in}}^4 \propto \frac{D^2}{\cos \theta} [\text{erg s}^{-1}], \quad (2.2)$$

where r_{in} , T_{in} , D and θ are the disk inner radius, temperature, the distance to the source and the inclination of the disk, respectively. Equation (2.1) and

(2.2) are written as

$$T = 6.24 \times 10^5 \left(\frac{r}{2r_g} \right)^{-3/4} \left(1 - \sqrt{\frac{r_{in}}{r}} \right)^{1/4} \left(\frac{M_{\text{BH}}}{10^8 M_{\odot}} \right)^{-1/4} \dot{m}^{1/4} [\text{K}], \quad (2.3)$$

and

$$L_{\text{disk}} = 4.72 \times 10^{45} \left(\frac{\eta}{1/12} \right) \left(\frac{\dot{M}}{1 M_{\odot} \text{year}^{-1}} \right) [\text{erg s}^{-1}], \quad (2.4)$$

where r_g and η are the gravitational radius ($= GM_{\text{BH}}/c^2$), and the radiative efficiency, respectively. $\dot{m} \equiv \dot{M}/\dot{M}_{\text{Edd}}$ is the scaled accretion rate, with the Eddington rate defined as $\dot{M}_{\text{Edd}} \equiv L_{\text{Edd}}/(\eta c^2)$.

Apparently this standard accretion disk alone cannot account for the X-ray emission, especially the power-law component. For it, higher temperature optically thin material is needed. One of such is an accretion corona. The temperature of the corona is assumed to be 10^9 K, and their location is either above the accretion disk (horizontal separation) or inner region very close to the central SMBH where disk is truncated (vertical separation). Haardt & Maraschi (1991) demonstrated that substantial fraction of energy is dissipated within a corona, whereas most of accreting material is retained within the main body of a disk. They introduced a parameter f , which represents a fraction of the gravitational energy dissipated in a corona via buoyancy and reconnection of magnetic fields out of the disk main body. To account for the absorbed power law component in X-ray band, they show f should be close to unity.

Theoretical and computational studies have been developed on the accretion corona (e.g. Meyer-Hofmeister et al. (2012); Liu et al. (2012)). Comparison with observations is performed by examining the photon index of the power-law component and the high energy cutoff. However, the latter has been limited to bright sources mainly BLS1s. One of the aims of our study is to obtain hard X-ray spectra for NLS1s of which quality is high enough to measure the high energy cutoff.

2.4.1 Mass of SMBHs

One of the goals of AGN (plus stellar BHs) studies is to understand and reorganize variety of accretion phenomena observed with limited number of

fundamental parameters. As well known, a BH can have only three parameters, mass, angular momentum, and charge. Accretion onto a BH should be controlled by accretion rate. Viewing angle may be observationally important.

The mass of a BH is the most important, but not necessarily well defined for AGNs. For stellar mass BHs in binary systems, the mass is generally constrained with a small error owing to inclination angle of the orbit. The mass of SMBHs in nearby normal galaxies and active galaxies have been measured precisely by motions of gas (e.g. Miyoshi et al. (1995)) or stars. For AGNs with BLRs, observational efforts called reverberation mapping have been extensively performed, in which the delay time of the variability in the intensity of the emission lines to that of the continuum emission is employed (e.g. Peterson (1993)). When these dynamical methods can be applied, the SMBH mass is accurately evaluated. If not applicable, we have to employ estimation based on empirical relation calibrated with some sources in which dynamical method is valid. Photo-ionization model for the BLR have been used for such a case (Kaspi et al., 2000). X-ray variability have been also used (e.g. Hayashida et al. (1998); McHardy et al. (2004)). Sometimes $M_{\text{BH}}-\sigma$ relation is employed.

Nevertheless, we should note that calibration of these empirical relation is needed, in particular when we discuss about a new class of AGNs. We study NLS1 sources in this thesis. None of the sources have dynamical mass estimates, and should be systematic uncertainty for them, and resultant L_{Edd} .

Chapter 3

Suzaku Observation of the Narrow Line Seyfert 1 Ton S180

3.1 Introduction

The X-ray spectra of active galactic nuclei (AGN) consist of several components, i.e., a power-law continuum, iron emission lines, a hard X-ray hump, and a soft X-ray excess. The power-law component is usually assumed to be the primary emission produced near central black holes (BHs), while the iron emission lines and the hard X-ray hump are the reprocessed emission from surrounding matter such as an accretion disk. Various kinds of absorbers, cold or warm, patchy or fully covered, also imprint features on emergent spectra. These X-ray spectral components and features are one of the best tools to probe the matter around the central BH. In some cases, however, observed X-ray spectra are not necessarily uniquely modeled, and various combinations of spectral models lead to different interpretations.

Narrow-Line Seyfert 1 galaxies (NLS1s) form a subclass of Seyfert 1 galaxies classified with their optical emission line properties and they are distinguished from typical broad-line Seyfert 1 galaxies (BLS1s). The NLS1s have distinctive X-ray properties, i.e., rapid and large amplitude variability and an enhanced soft X-ray excess, compared with those of the BLS1s (Leighly, 1999a,b). The rapid X-ray variability of the NLS1s sometimes lead to the hypothesis that the NLS1s have lower mass BH than the BLS1s (Hayashida, 2000; Wang & Lu, 2001; Kawaguchi, 2003). The enhanced soft X-ray excess component is usually fitted with a blackbody or a multi-color disk with temperature of $kT = 0.1 - 0.2$ keV, and is often considered as evidence of high accretion rate of this class by analogy to stellar mass BHs at high state

(Pounds et al., 1995). Nevertheless, the temperature of $kT = 0.1 - 0.2$ keV is too high for the emission from the standard optically thick accretion disk around super massive BHs of $M = 10^{6-8} M_{\odot}$. Various sophisticated models of accretion disk have been proposed to explain the soft X-ray excess component (Mineshige et al., 2000). Alternatively, blurred reflection (Fabian et al., 2002) or absorption (Middleton et al., 2007) can make the soft X-ray component. Steeper slope of the power-law continuum of the NLS1s than that of the BLS1s is another point of differences between these two subclasses (Boller et al., 1996; Brandt et al., 1997). The difference might reflect the properties of the accretion corona, though hard X-ray observations of the NLS1s so far have been limited to judge it. Observations of the NLS1s with Suzaku are expected to extend our knowledge on this subclass and with wide energy range coverage above 10 keV, and with good energy resolution at low energy band below 1 keV, as was shown for PG 1211+143 (Reeves et al., 2008), and NGC 4051 (Terashima et al., 2009).

Ton S180 (PHL 912) is a bright NLS1 galaxy at $z = 0.0620$, of which $H\beta$ line width is 900 km s^{-1} (Wisotzki et al., 1995). Low Galactic absorption toward the object ($N_H = 1.55_{-0.13}^{+0.27} \times 10^{20} \text{ cm}^{-2}$; Dickey & Lockman (1990)) allows us to observe extreme ultra violet (EUV) to soft X-ray spectrum of this source. In fact, this source is one of the brightest extragalactic sources detected with the EUV explorer (Wisotzki et al., 1995), and identified with a bright X-ray source detected in the ROSAT all sky survey (Fink et al., 1997). X-ray observations of this source were made also with Beppo-SAX (Comastri et al., 1998), ASCA (Turner et al., 2002; Romano et al., 2002), Chandra (Turner et al., 2001; Rózańska et al., 2004), XMM-Newton (Vaughan et al., 2002; Murashima et al., 2005), and RXTE (Murashima et al., 2005). These observations showed that Ton S180 has the soft X-ray excess emission below 2 keV and a steep power-law index in the 2–10 keV band. X-ray variability of factor of 2 or larger with a time scale of less than 1000 s was observed. These properties are consistent with common features of the NLS1s.

Turner et al. (2002) presented the multi-wavelength spectral energy distribution (SED) of Ton S180 from infrared to X-rays, indicating the most of the energy is emitted in the 10–100 eV band, in contrast to the fact that BLS1s typically have peak emission at UV band known as UV bump. The central BH mass of Ton S180 has not yet been measured with the reverberation method (Peterson, 1993). Referring the empirical relation between the luminosity at

5100 Å and the BH mass (Peterson et al., 2000), Turner et al. (2002) estimate the BH mass of Ton S180 as $2 \times 10^7 M_{\odot}$ with a factor of 2 uncertainty. Turner et al. (2002) also provide the unabsorbed luminosity in the 0.5 eV to 10 keV regime as $5.4 \times 10^{45} \text{ erg s}^{-1}$ with $H_0 = 75 \text{ km s}^{-1} \text{ Mpc}^{-1}$ and $q_0 = 0.5$, which corresponds to $6.6 \times 10^{45} \text{ erg s}^{-1}$ with $H_0 = 70 \text{ km s}^{-1} \text{ Mpc}^{-1}$, $q_0 = 0.0$, and $\lambda_0 = 0.73$. It means that this object emits the radiation at around the Eddington limit.

The soft X-ray excess component of Ton S180 has been extensively studied. Comastri et al. (1998) showed a double power-law model with the photon indices (Γ) of 2.3 and 2.7 is adequate for the 0.1–10 keV spectra obtained with Beppo-SAX in 1996. Vaughan et al. (2002) employed the same model but with slightly different indices 3.1 and 1.5 to the X-ray spectra obtained with XMM-Newton in 2000. Murashima et al. (2005) proposed a model consisting of a $\Gamma = 2.3$ power-law and a $\Gamma = 2.1$ power-law suffered by exponential cut off with 0.4 keV. On the other hand, Turner et al. (1998) showed that the ASCA spectra of the target in 0.6–10 keV is fitted with a power-law model with $\Gamma = 2.5$ plus a broad Gaussian line centered on the rest frame energy of 0.82 keV. Blackbody or multi-color disk models have been also employed to fit the spectra. The soft X-ray excess component in the ASCA spectra obtained in 1999 are fitted with a blackbody of $kT = 0.13 \text{ keV}$ or a second power-law of $\Gamma = 5.2$ by Murashima et al. (2005). According to Vaughan et al. (2002), the soft X-ray component of the XMM-Newton spectra is fitted with blackbody models of three temperatures $kT = 33, 103, \text{ and } 248 \text{ eV}$. Turner et al. (2001) showed the Chandra LETG spectrum of this source is approximated with a blackbody model with $kT = 158 \text{ eV}$ plus a power-law model. These controversial results may imply difficulties in determining the soft X-ray excess spectral model in this source or in general. Nevertheless, since high resolution grating spectroscopies indicate that the soft X-ray emission of Ton S180 is not originated in collection of narrow emission lines and absorption features are not so strong (Turner et al., 2001; Vaughan et al., 2002; Rózańska et al., 2004), it is worth studying the soft X-ray excess component with CCD resolution.

The iron K emission of Ton S180 has also been of special interest, since Comastri et al. (1998) and Turner et al. (1998) discovered an evidence of iron K emission line from ionized matter. Comastri et al. (1998) modeled the iron K emission line in the 1996 Beppo-SAX spectra as a narrow Gaussian line centered on $7.11 \pm 0.16 \text{ keV}$ (rest-frame), while Turner et al. (1998) modeled

the ASCA 1996 spectra with two narrow Gaussian lines, one at 6.4 keV and the other at $7.01_{-0.21}^{+0.24}$ keV. Similar double Gaussian model was also applied to the ASCA 1999 spectra by Romano et al. (2002), one broad line at 6.58 keV and the other narrow line at 6.81 keV. Vaughan et al. (2002) showed the iron K line centered at 7.0 keV is detected in the XMM-Newton 2000 spectra of this source. Since the center energy of the iron K emission detected in these observations are almost consistent with that of hydrogen-like iron, the source has most likely have ionized reflector. Reflection component is commonly observed in the X-ray spectra of Seyfert galaxies, but highly ionized case is not so common. For example, among the 26 Seyfert galaxies observed by XMM-Newton for which Nandra et al. (2007) examined iron K lines, 4 objects show the line center energies significantly (68% confidence range) higher than 6.5 keV. The 4 objects consist of 2 BLS1s and 2 NLS1s. Statistical argument whether NLS1s or BLS1s preferentially have highly ionized iron K lines is interesting, but difficult to be answered with this small sample.

The X-ray spectra of Ton S180 above 10 keV was obtained only with RXTE but up to 15 keV (Murashima et al., 2005). It is not certain how the power-law component extends above 10 keV and whether the reflection hump is observed in NLS1s or not. Suzaku is good for this purpose with its wide energy coverage. Good energy resolution of the Suzaku XIS is expected to provide new insights on the soft X-ray component and iron K emission of Ton S180, too. In this paper, we report the results of the Suzaku observation of this source. We adopt the cosmological parameters of $H_0 = 70 \text{ km}^{-1} \text{ Mpc}^{-1}$, $q_0 = 0.0$, and $\lambda_0 = 0.73$.

3.2 Observation & Data Reduction

Ton S180 was observed by Suzaku (Mitsuda et al., 2007) from 2006 December 9 at 13:29 UT until December 12 at 08:36 UT (OBSID=701021010). The observation was carried out with the X-ray Imaging Spectrometer (XIS: Koyama et al. (2007)) and the Hard X-ray Detector (HXD: Takahashi et al. (2007); Kokubun et al. (2007)). The target was placed at the nominal center of the XIS field of view. The XIS consists of four CCD cameras, three (XIS0, XIS2, XIS3) with front illuminated (XIS-FI) CCDs and one (XIS1) with a back illuminated (XIS-BI) CCD, XIS2 was not available after 2006 November 9, the other three CCDs were used in our observation. The normal full-window

clocking mode with the spaced-row charge injection (SCI: Uchiyama et al. (2009)) was employed. The XIS edit mode was 3×3 and 5×5 , and the data of both modes were combined in our analysis. The HXD was operated normally in the observation.

We reprocessed the XIS and HXD data by using the latest CALDB as of 2009 May. The same data selection criteria as that used for archived cleaned event lists were employed. We further restricted the time interval in which both the XIS and HXD data were available simultaneously for our analysis. This selection led to total effective exposure time of 108 ks. The software packages of HEASoft v.6.7 and v.6.8 were used in our data reduction and analysis.

Standard reduction procedures were applied to the XIS data. In the XIS field of view there found no sources with comparable brightness to the target, Ton S180. Referring the XMM Serendipitous Source Catalog (2XMMi DR3 Version; Watson et al. (2009)), in fact, the second brightest source to Ton S180 within the $30'$ radius from it is 2XMMJ 005653.2–221549, whose 0.2–12 keV band flux is $5 \times 10^{-13} \text{ erg s}^{-1} \text{ cm}^{-2}$ about 1/50 of Ton S180 recorded in the same catalog. We thus extracted the XIS source products from the circular regions of $4'.3$ radius centered on the source, while the background products from the annular regions with the inner and outer radius of $4'.3$ and $6'.9$, respectively. The redistribution matrices and the ancillary response files for spectral analysis were made for each XIS using `xisrmfgen` and `xissimarfgen`, respectively. XIS spectra from two FI CCDs were combined by `mathpha`. Correspondingly, the redistribution matrices and ancillary response files for the FI CCDs were combined by using `addrmf` and `addarf`, respectively. The source spectra were grouped such that each spectral bin contains at least 40 counts in the spectral fitting.

We followed standard data reduction procedure for the Si PIN diode (HXD-PIN) data, including dead time corrections. For the HXD-PIN non-Xray Background (NXB), a simulated event file supplied by the HXD team based on the LCFITDT model (Fukazawa et al., 2009) were used. Because the HXD-PIN count rate is dominated by the NXB (not by the X-rays from the source in our case), the uncertainty of the NXB is crucial to our analysis. We examine its uncertainty with our data in the following section by referring the description in Fukazawa et al. (2009). We also have to evaluate and subtract the Cosmic X-ray Background component (CXB). We used the empirical model by Boldt

(1987), i.e., $9.412 \times 10^{-3} (E/1 \text{ keV})^{-1.29} \exp(-E/40 \text{ keV}) \text{ photons cm}^{-2} \text{ s}^{-1} \text{ keV}^{-1} (2^\circ \times 2^\circ)^{-1}$. We simulated the CXB component with this spectral model and the HXD response file for this uniform diffuse emission and added to the NXB component to make the total background spectrum. The HXD-PIN response file for a point source at the XIS nominal position, `ae_hxd_pinxinome3_20080129.rsp`, was used in the spectral analysis.

We also reduced the GSO scintillates (HXD-GSO) data by following a standard procedure. The net counting rate (data – NXB) is -0.2% and $+1.1\%$ of the NXB, in the 50–100 keV and 100–200 keV range, respectively. Fukazawa et al. (2009) states that 1σ systematic uncertainty of the HXD-GSO NXB model in 50–100 keV is less than 1%. Therefore, we regard no significant source flux was detected with HXD-GSO for Ton S180 and would mention the results only from the HXD-PIN in the following sections.

3.3 Time Averaged Spectra

In this section, we study the time averaged spectra of Ton S180 obtained with Suzaku. We fitted the XIS-FI, XIS-BI and HXD-PIN spectra simultaneously using `XSPEC` v12. All errors quoted in the text and tables are at 90% confidence level unless otherwise noted, while the ones quoted in figures are at 1σ confidence level. We fixed the Galactic absorption and red shift at $N_{H,Gal} = 1.55 \times 10^{20} \text{ cm}^{-2}$ and $z = 0.062$, respectively. We noticed the energy range of 0.4–12 keV, 0.25–8 keV, and 15–55 keV for the XIS-FI, XIS-BI, and HXD-PIN spectra, respectively. The XIS spectra between 1.8 keV and 1.9 keV were ignored because of the calibration uncertainty.

The quantum efficiency of the XIS is affected by contaminations on the OBF (Koyama et al., 2007). The effect has been monitored and modeled in the tool, `xissimarfgen`. We checked its validity by applying the same data reduction procedure to the XIS-BI data of RXJ 1856.5–3754, observed in 2006 October and 2007 October.

The isolated neutron star RXJ 1856.5–3754 has been observed with various missions and is considered to be one of the standard candles in the soft X-ray regime (Burwitz et al., 2003). Nevertheless, we found a significant residual in the XIS-BI spectra of this source below 0.3 keV when we employ the spectral model of this source written in Burwitz et al. (2003). The residual is most likely indicating the contamination model in the current `xissimarfgen` is

not perfect. A significant fraction of the residual is, however, removed by introducing additional absorber consisting of H, C, and O. This absorber is an empirical one to adjust small error in the current contamination model, and negative column density is allowed. We obtained the column densities of H, C, and O needed for compensate the residual in the XIS-BI spectra of RXJ 1856.5–3754 observed in 2006 October and 2007 October. Values for the data in 2006 December (Ton S180) are determined by interpolation; the equivalent column densities of 6.79, -3.12 , and 2.29 for the H, C, O, respectively, in the unit of 10^{20} cm^{-2} .

We also used the gain offset of -3.1 eV and -9.4 eV for the XIS-FI and the XIS-BI spectrum, respectively. These offset values determined so as to minimize residuals around instrumental edge structures of C and O are within the calibration uncertainty. Residuals at 0.3 keV seen figures 3.4–3.7 are instrumental one, most likely small error in the energy resolution in low energy band, as similar residuals is remained for the spectra of RXJ 1856.5–3754. Normalization of the XIS-BI to the XIS-FI was set as a free parameter, while that of the HXD-PIN to the XIS-FI was fixed at 1.16 according to the cross calibration results with the Crab nebula.

We start the spectral analysis by fitting the $2.5\text{--}10 \text{ keV}$ band spectra with a simple power-law suffered by the Galactic absorption. This fit gives $\chi^2 = 868.6$ for degrees of freedom (dof) = 859, indicating the spectra in this middle energy band are approximated with a simple power-law with a photon index of $\Gamma = 2.24 \pm 0.03$. Extrapolating the model to the whole energy ($0.25\text{--}55 \text{ keV}$) band, however, shows that the spectra have a soft X-ray excess and a hard X-ray excess, as shown in figure 3.1.

The spectral ratio plot also shows an emission line like feature at 6.3 keV and an absorption line like structure around 7.4 keV in observers' frame. Those features are more evident in the zoom up version of the spectral ratio as shown in figure 3.2. The emission feature is approximated with a Gaussian line centered at $6.7_{-0.2}^{+0.1} \text{ keV}$ (source rest frame) with width σ of $0.4_{-0.1}^{+0.3} \text{ keV}$ and the Equivalent Width (EW) of $190_{-146}^{+150} \text{ eV}$. The $K\alpha$ line from neutral iron, is not apparent. We find the 90% upper limit for the EW of a narrow emission line at 6.4 keV as 35 eV . On the other hand, the absorption feature is fitted with a Gaussian line centered at $7.90 \pm 0.06 \text{ keV}$ (source rest fame) with width σ of $<0.1 \text{ keV}$. We note the absorption line energy in observers' frame is close to that of Ni $K\alpha$ line, which is prominent in the XIS background spectra.

However, since the absorption feature is evident even if we changed the radius of the source extraction region from $4'.3$ to $1'.4$, with which background contribution to the flux from the source is much smaller, the structure is most likely in the incident spectra.

3.3.1 Hard X-ray Excess

We next search for the model to reproduce the hard X-ray excess by concentrating the spectra in the 4–55 keV range. Before proceeding to a fitting process, we evaluate the systematic uncertainty in the HXD-PIN flux. The dead-time corrected counting rate in the 15–40 keV band is $0.324 \pm 0.002 \text{ count s}^{-1}$, where 1σ statistical error is shown, while that of the NXB model and the CXB model is $0.293 \text{ count s}^{-1}$ and $0.016 \text{ count s}^{-1}$, respectively. These lead to a net flux from the source of $0.015 \pm 0.002 \text{ count s}^{-1}$, corresponding to $5.1 \pm 0.7\%$ of the NXB. According to Fukazawa et al. (2009), the systematic uncertainty of the LCFITDT NXB model is 2.1–2.7% by referring the sky observation data for the Cygnus Loop and E0102.2–7219, while significantly smaller systematic error of 0.34% is reported for the dark earth observations with long (40 ks) exposures. However, when we apply the same background (NXB and CXB) model to three sky observations, the Lockman Hole field in 2006 (Obsid=101002010), the same field in 2007 (Obsid=102018010), and NGC 4472 on 2006 December (Obsid=801064010), the net counting rate (observed – NXB – CXB) in the 15–40 keV band is $1.69 \pm 0.68\%$, $3.16 \pm 0.70\%$, and $-2.72 \pm 0.60\%$ of the NXB, respectively.

We also checked that the net counting rate of the HXD-PIN above 60 keV, where contribution from the source is less likely, is $0.7 \pm 1.8\%$ for the Ton S180 observation. On the other hand, those for other three observations are $1.0 \pm 2.4\%$, $1.4 \pm 2.2\%$, and $0.6 \pm 1.9\%$, respectively. It implies that there is not an apparent problem in the NXB model for either of these data. Therefore, we consider that the systematic uncertainty of 2.1–2.7% is reasonable for our case and adopt the systematic error of 2.7% of the NXB. Considering the CXB fluctuation (0.7% of the NXB; Fukazawa et al. (2009)) and the statistical error, we estimate the 1σ error is 2.9% of the NXB. Since Ton S180 15–40 keV flux is 5.1% of the NXB, we conclude that Ton S180 was detected with the HXD-PIN in 15–40 keV band with confidence level of about 90%. Although it should be regarded as a marginal detection, we proceed to a fitting process.

If the primary emission is a power-law, as usually assumed, the hard X-ray

excess above 10 keV can be modeled either with a reflection component or with partial absorption. The reflection component from ionized matter is a primary candidate, since the broad iron emission line is centered at 6.7 keV. We employed the `reflionx` model by Ross & Fabian (2005) with relativistic blurring `kdblur`. The model is schematically expressed as `wabs × gabs × {powerlaw + kdblur × reflionx}`. The fit to the 4–55 keV range spectra is acceptable with $\chi^2 = 586.8$ for $\text{dof} = 590$. The best fit parameters for the reflection component is the disk inner radius R_{in} of $250_{-230}^{+150} r_g$, where $r_g = GM/c^2$ is the gravitational radius, the disk inclination angle of $88_{-88}^{+2} \text{ }^\circ$, the ionization parameter ξ of 209_{-35}^{+1374} . Note that we fixed the disk outer radius R_{out} of $400 r_g$ and the emissivity index q of 3. The ionization parameter is defined as $\xi = L/nr^2$, where L is the ionizing luminosity, n is the electron number density, and r is the distance between the primary continuum source and the reflecting material. High ionization parameter of 209 is consistent with the iron line energy. The disk inner radius of $250 r_g$ is significantly larger than typical cases like the disk line from the vicinity of the central BH in MCG–6-30-15 (Miniutti et al., 2007). Nevertheless, these parameters were not well constrained in the current range of the spectra, and we would discuss in the following section in which full energy band spectra are employed.

The spectral fit result with this model, a power-law component plus the relativistically blurred reflection component, is shown in figure 3.3. Although this model is acceptable in terms of χ^2 value, figure 3.3 indicates the model underestimates the data by about a factor of 2 above 10 keV. In the same figure we show the HXD-PIN spectra for which the NXB model over/underestimated by 3% is applied to illustrate systematic uncertainties. The discrepancy between the model and the HXD-PIN spectrum increases with the -3% NXB, while the HXD-PIN spectrum using the +3% NXB is reproduced with the reflection model.

In order to improve the fit in the 15–55 keV band, we considered to include a partial absorption. By adjusting thickness and covering fraction of the partial absorber, we can reproduce the hard X-ray excess observed in the 15–55 keV energy band with little affecting the spectra below 10 keV, if the absorber is cold. There are various possible combinations of reflectors and absorbers, we here assume the cold partial absorber resides in the outside of the region where the primary power-law and the reflection component are produced. We assume the iron emission line at 6.7 keV is originated in the

reflection component. The model expression here is `wabs` \times `gabs` \times `zpcfabs` \times { `powerlaw` + `kdblur` \times `reflionx` }. The fit provided $\chi^2 = 577.0$ for dof=588 and succeeded in reproducing the HXD-PIN spectra with the nominal NXB model. Based on the best fit parameters, the partial absorber has extremely high column density of $5.0 \times 10^{24} \text{ cm}^{-2}$ and the covering factor of 0.61. The heavily absorbed component is visible only above 10 keV. Considering the systematic uncertainty in the HXD-PIN flux mentioned above, however, significance of this heavily absorbed component is not necessarily high. We have to consider possible contribution of the neutral iron K line from this absorber and the correction factor for the intrinsic luminosity of this source. We will discuss these issues in section 3.5.3.

We here mention on the absorption feature around 7.9 keV again, for which we employed a Gaussian profile. We tried to fit this feature by extra absorption by highly (photo) ionized matter with Doppler velocity using `warmabs` model of `xstar` v2.2. The feature is reproduced with highly ionized ($\log \xi = 4.4_{-1.5}^{+0.4}$) matter with column density of 10^{24} cm^{-2} (upper bound of the model parameter), where we fix the abundances of metals as those of the solar values. The absorber has a outflowing velocity of 38000 km s^{-1} . As we will discuss in section 3.5.3, these kinds of outflowing absorber are observed in many sources.

3.3.2 Soft X-ray Excess

We next focus on the emission models to reproduce the soft X-ray excess by using the 0.25–55 keV full energy band spectra. We first examined whether we were able to reproduce the spectra without introducing an extra component in addition to the model used in the previous section. In fact, the reflection from ionized accretion disk has a significant soft X-ray emission and was proposed as the origin of the soft X-ray excess (Fabian et al., 2002). When we employed the same model determined in the fit to the 4–55 keV spectra, significant soft excess remains. Even if we repeat the fit with making model parameters free, the fit is not acceptable, $\chi^2 = 2457.4$ for dof of 2096. The best fit power-law index in this model is 2.72, significantly steeper than the index of 2.17 determined with the 4–55 keV spectra. Therefore, the model fails to reproduce the hard X-ray excess. The contribution of the reflection component at iron K band is about 1/20 of the total model flux, which fails to reproduce the observed iron K line, either. We further tested a model

in which two kinds of reflection components with different parameters are included, obtaining $\chi^2 = 2256.3$ for $\text{dof} = 2091$. We thus concluded that an extra component is needed to reproduce the soft X-ray excess.

We tested a disk blackbody model (`diskbb`), power-law model (`powerlaw`), cutoff power-law model (`cutoffpl`), and Comptonized blackbody model (`compbb`) for the extra component to reproduce the soft X-ray excess. The model, for example the disk blackbody case, is expressed as `wabs` \times `gabs` \times `zpcfabs` \times { `diskbb` + `powerlaw` + `kdblur` \times `reflionx` }. The fitting results are summarized in table 3.1 and figures 3.4, 3.5, 3.6, and 3.7. We allowed the parameters for the `gabs` free; the absorption line center energy was determined as 7.44 ± 0.06 keV in the observers' frame, i.e., 7.9 keV in the source rest frame, for all the cases. For the reflection component, the disk outer radius was fixed at $400 r_g$, while the disk inner radius was determined in the fits as $20\text{--}27 r_g$. The best fit value for the disk inner radius is smaller than that determined in the 4–55 keV spectral fit but consistent with each other with taking into account of the error. The best fit value for the disk inclination was $86^\circ\text{--}90^\circ$, indicating nearly edge on. This large inclination angle is responsible for making the line emissions broad even with relatively large disk inner radius. The ionization parameters were obtained as 288–1142, indicating the reflection comes from highly ionized matter, as is suggested from the iron K line energy. We also note that the broad line feature of OVIII appeared around 0.6 keV (observers' frame) in the reflection model is consistent with the spectra observed. In fact, the feature is visible in the spectral ratio plot in figure 3.1.

On the other hand, the column density of the partial absorber is as high as $2\text{--}6 \times 10^{24} \text{ cm}^{-2}$ except for the model with the Comptonized blackbody component, in which the hard X-ray excess is reproduced with a flat spectrum of the Comptonized blackbody with the electron temperature of 68 keV and $\tau = 0.16$. Correspondingly, the photon index of the (primary) power-law component in this model is 2.65 ± 0.02 , while that in the other three models ranges from 2.24 to 2.38.

The reduced χ^2 is the smallest for the model with the disk blackbody component ($\chi^2/\text{dof} = 1.059$) and the largest for the model with the Comptonized blackbody component ($\chi^2/\text{dof} = 1.081$). The null hypothesis probability for the disk blackbody model is 3% and that for the Comptonized blackbody model is 0.5%. We can reject the model with the Comptonized blackbody

component and that with the power-law component with a significance level as 2%. The model with the cutoff power-law component provides a similar χ^2/dof value as the disk blackbody model. We thus adopt these two models to reproduce the time averaged spectra of Ton S180. We conclude that the soft X-ray excess in Ton S180 is modeled with a combination of the relativistically blurred reflection from highly ionized matter plus the extra component, either of the disk blackbody model with the inner disk temperature of 75_{-3}^{+2} eV or the cutoff power-law model with the photon index of $3.2_{-0.2}^{+0.3}$ and the cutoff energy of $1.0_{-0.2}^{+0.6}$ keV.

In both cases, the observed flux between 2–10 keV is dominated by the (direct) power-law component; the contribution of the reflection component is about one order of magnitude smaller than the power-law component. On the other hand, below 0.5 keV, the three components, i.e., the power-law, reflection, and disk blackbody or cutoff power-law components contribute to the total flux comparably, as shown in figures 3.4 and 3.6.

3.4 Variability Analysis

3.4.1 Light Curve

We show background-subtracted light curves of Ton S180 in two energy bands (figure 3.8). The 0.2–12 keV light curve shows that the source has random flux variability of thousands seconds with amplitude of about 20% or less. We also note that there is a systematic flux drop at 9×10^4 s of about 30%. We labeled the time zone before and after this flux drop as TZ1 and TZ2, for which we examined the spectral drop in section 3.4.3. TZ1 and TZ2 have effective exposure time of 39 ks and 69 ks, respectively. Although the flux variability is found in the HXD-PIN light curve, this might be due to systematic error of the NXB model, since the variability pattern has an one day periodicity.

3.4.2 RMS Fractional Variability

We next examined the RMS fractional variability of each energy band, which is a flux normalized root mean square variability where statistical fluctuation is subtracted. We made the RMS fractional variability from the X-ray light curves of 7 energy bands with the time bin size of 512 s, as shown in figure 3.9. The RMS fractional variability for the HXD-PIN was not well determined,

and the 1σ upper limit is shown in the figure. Except for this point, the RMS fractional variability of Ton S180 shows little energy dependence, while the variability is slightly larger in lower energy band.

Based on the results of the spectral fit presented in the previous section, 2–10 keV energy band is dominated by the power-law component. Therefore, the variability in the same energy band (about $r_{var} \sim 0.15$) should be regarded as that of the power-law component. The slight energy dependence, larger variability in lower energy band, might indicate that the fractional variability is larger for the other spectral components, i.e., the reflection component, the disk blackbody or the cutoff power-law component. Another possibility is that the power-law slope gets steeper when the flux gets larger. We would examine these possibilities in the next section.

3.4.3 Spectral Variability

We investigated the X-ray spectral variability of Ton S180 by comparing the spectra of the two time zones, TZ1 and TZ2. Note that the flux difference between them is not so large; the XIS-BI counting rate in the TZ2 is about 20% smaller than that in TZ1. We performed the simultaneous fit to the TZ1 and TZ2 spectra based on the model including the disk blackbody model as the extra soft X-ray component, which reproduces the time averaged spectra best in the previous section. We considered the following four possible cases in which the spectral variability between TZ1 and TZ2 is due to (A) change in the normalization and the temperature of the disk blackbody component, (B) change in the normalization and the index of the power-law component, (C) change in the normalization and the ionization parameter of the reflection component, (D) change in the covering fraction of the partial absorber. We allowed parameters specified above to change but made other parameters tied. Some of the model parameters, such as, absorption line parameters of `gabs`, the disk inner and outer radius and the emissivity index for the `kdblur`, the column density of the partial absorber `zpcfabs` were fixed as the values determined for the time averaged spectra (table 3.1).

The value of χ^2 obtained in the fit for each case is (A) 5789.3 for dof = 3248, (B) 3453.3 for dof = 3246, (C) 3480.0 for dof = 3245, and (D) 3394.9 for dof = 3246. For reference, we also tried a model using the cutoff power-law model as an extra component and made the normalization and the photon index of the parameter change. This case (A') fails to reproduce the

spectral variability, $\chi^2 = 4404.7$ for $\text{dof} = 3246$. The case (D), in which only the covering fraction changes between TZ1 and TZ2, provides a marginally acceptable fit (the model is not rejected with a significance level smaller than 2.9%), while the other models fail to reproduce the spectral change between TZ1 and TZ2. We show the spectra of TZ1 and TZ2 unfolded with the case (D) model in figure 3.10. The covering fraction for the TZ1 spectra is $0.37_{-0.21}^{+0.07}$, while that for the TZ2 spectra is $0.50_{-0.15}^{+0.06}$. As shown in the figure 3.10, the shape of the XIS spectra in TZ1 and TZ2 are similar each other but their normalizations seem different. Change in the covering fraction makes such spectra without affecting the HXD-PIN spectra.

We examined the other case (E) in which the spectral parameters of the TZ1 and TZ2 are set common except for the global normalization. This model provides comparable goodness of fit ($\chi^2 = 3366.5$ for $\text{dof} = 3246$) as that of (D). Variability of the HXD-PIN spectra is the key to confirm which model (D) or (E) is better description of the spectral variability of Ton S180. However, the statistical errors of the HXD-PIN spectra are too large to resolve the issue.

3.5 Discussion

We studied the X-ray spectra and variability of Ton S180 observed with Suzaku. The wide-band (0.25–55 keV) spectra are reproduced with a model consisting of three components, the power-law component, the reflection from highly ionized disk component, and the extra soft component which is explained with either of disk blackbody or cutoff power-law. The broad iron emission line centered at 6.7 keV and the hump corresponding to the OVIII line are consistently reproduced with the reflection model. We also found an absorption feature at 7.9 keV. We detected the hard X-ray (above 15 keV) emission of this source for the first time but with a marginal confidence level of 90%. In order to explain the hard X-ray excess, we introduced a Compton-thick partial absorber.

3.5.1 Long Term Variability and Eddington Ratio

Ton S180 was observed with previous missions repeatedly. We summarize the X-ray flux measured so far in figure 3.11 for two energy bands, 0.5–2 keV and

2–10 keV. Some of the data points were converted from the flux in different energy bands reported in the literature. The plot indicates that the flux variation is smaller than $\pm 30\%$ around the mean. It contrasts with dramatic behavior found in some other NLS1 cases. For example, NGC 4051 exhibited a switch-off state in which direct component was extremely faint (Uttley et al., 1999). Mrk 335 showed a long term variation with amplitude of more than one order of magnitude since 1970’s (Grupe et al., 2008). In the case of PG 1211+143, long term decline by about one order of magnitude over 30 years was found (Bachev et al., 2009).

We evaluate the 1–10 keV unabsorbed (corrected for the Galactic absorption) luminosity of Ton S180 is $9.0 \times 10^{43} \text{ erg s}^{-1} \text{ cm}^{-2}$. That for 0.25–1.0 keV band is $1.9 \times 10^{43} \text{ erg s}^{-1}$. According to multi-wavelength observation of Ton S180 by Turner et al. (2002), 0.5 eV–10 keV luminosity, which should be regarded as approximately the bolometric luminosity, is 82 times of the 1–10 keV luminosity. Therefore, we estimate the 0.5 eV–10 keV luminosity is $7.4 \times 10^{45} \text{ erg s}^{-1}$. As mentioned earlier, since the BH mass of Ton S180 is estimated to be $2 \times 10^7 M_{\odot}$, Ton S180 has the Eddington ratio of 2.7. If we consider the fact that about half of the emission is covered by the Compton-thick absorber in our model, the intrinsic luminosity is doubled, leading to the Eddington ratio of 5.

The Eddington ratio larger than 1 might partly be due to the error in the BH mass (note the mass estimate is based on an empirical method) and/or to the error in the bolometric correction factor. Nevertheless, the long term stability mentioned above is suggestive to a view that Ton S180 is radiating at around the Eddington limit. We expect dynamical methods, such as reverberation mapping, will be applied to this source to obtain more accurate BH mass of this source.

3.5.2 Reflection Component and Soft X-ray Excess

One of our motivations to observe this source was to understand the nature of the soft X-ray excess and the iron K emission line from highly ionized matter. We found a broad iron emission line centered at 6.7 keV in the spectra of Ton S180. The line center energy higher than 6.4 keV is consistent with previous observations of this source with ASCA (Turner et al., 1998), Beppo-SAX (Comastri et al., 1998), and XMM-Newton (Vaughan et al., 2002), although modeling the emission line feature is not exactly the same in these studies. We

modeled it as a part of reflection component from ionized disk. The same reflection component contributes to significant fraction of the soft X-ray excess emission.

We adopted the relativistically blurred reflection model from ionized disk, `kdblur` \times `reflionx`. This reflection model succeeds in reproducing not only the ionized iron K line but also a hump around 0.6 keV as OVIII emission line. Reflection continuum models, such as `pexriv`, are not sufficient for our purpose. Detailed analysis of the Chandra LETG spectrum of Ton S180 is presented in Róžańska et al. (2004). They fitted the soft X-ray spectrum with several narrow absorption lines and a few emission disk lines. An emission line at 0.63 keV with EW of 13.5 eV was identified as OVIII line in their analysis using a `diskline` model, though the parameters are not necessarily consistent with those listed in our case (table 3.1). On the other hand, deviation from a simple power-law spectrum fit around 0.5–0.6 keV was suggested in the XMM-Newton RGS spectrum by Vaughan et al. (2002). But they attributed it to a possible instrumental feature. We thus expect high resolution spectroscopy with large effective area instruments in future will give firmer results on the low energy line emission features. We note that the relativistic blurring must be mild to be the feature visible. Relatively large inner disk radius, $20 r_g$ obtained in our fit (table 3.1), is needed to the OVIII line and also the iron K line are found in the spectra.

In our interpretation, the soft X-ray excess is made of two components in addition to the power-law component; one is the reflection component mentioned above, and the other is the extra component, for which we showed the disk blackbody model or the cutoff power-law model almost equally reproduce the observed spectra. If this interpretation is correct, previous discussions on the origin of the soft X-ray excess of Ton S180 in which the reflection component was not taken into account, e.g., Vaughan et al. (2002) and Murashima et al. (2005), need to be reconsidered. Even if the cutoff power-law model is one of our solutions for the extra soft X-ray excess component, relative contribution to the total flux is smaller for our model than that by Murashima et al. (2005).

When we adopt the disk blackbody model as an extra soft X-ray excess component, the inner disk temperature of 75^{+2}_{-3} eV is significantly lower than that previously considered. Difficulty in explaining the soft X-ray excess with blackbody emission from optically thick accretion disk, not only for this source

but also for other Seyferts, is in its high temperature. Therefore, the lower temperature may relax the condition for this interpretation. The inner disk radius r_{in} is $7 \times 10^6 / \sqrt{\cos(i)}$ km, where i is the disk inclination angle. This corresponds to $0.23 / \sqrt{\cos(i)} r_g$ for a $2 \times 10^7 M_\odot$ BH. If the disk is edge on, as is suggested in the reflection model fit (table 3.1), the inner radius can be close to, for example, the last stable orbit $1.24 r_g$ for the extreme Kerr case. If this object is radiating around the Eddington limit as we suggested above, the accretion disk is not likely the standard geometrically thin disk. Theoretically different solutions, such as the slim-disk, are favored. Mineshige et al. (2000) provided the expected disk temperature as $2 \times 10^6 (M/10^5 M_\odot)^{-1/4} (r/2r_g)^{-1/2}$ (K). This yields 60 eV for $r = 1.24 r_g$ and BH mass of $2 \times 10^7 M_\odot$. This value is not so different from 75 eV we obtained. We need some cautions here; firstly, the fitting parameters of the disk blackbody component, since contributions of the three components below 1 keV are comparable and coupled strongly, secondly, the reflection component is based still on a simplified assumptions, thirdly, more sophisticated models have been proposed for the slim-disk model than that in Mineshige et al. (2000), for example, Comptonization effect or electron/ion temperature separation etc. Nevertheless, it is worth emphasizing that optically thick emission from the accretion disk can be an explanation of the extra soft X-ray excess component.

We also considered the effect of electron scattering (Comptonization) on the continuum spectrum of accretion disk. Some researchers have stressed the importance of scattering effects (Czerny & Elvis, 1987; Wandel & Petrosian, 1988; Ross et al., 1992; Shimura & Takahara, 1993; Yamada et al., 1994; Done et al., 2012). When we consider the standard accretion disk, the temperature which electron scattering becomes important is written as the following equation (Czerny & Elvis, 1987; Wandel & Petrosian, 1988):

$$T_{\text{Comp}} = 1.3 \times 10^5 \left(\alpha \frac{M_{\text{BH}}}{10^8 M_\odot} \dot{m} \right)^{-4/17} \text{ K}, \quad (3.1)$$

where α is a viscosity parameter and we assumed $\alpha = 0.3$. In the case of Ton S180, when we assumed the central BH mass and the accretion rate to be $M_{\text{BH}} = 2 \times 10^7 M_\odot$ and $\dot{m} = 1$, we obtain $T_{\text{Comp}} \sim 2.5 \times 10^4$ K, which corresponds to $kT_{\text{Comp}} \sim 22$ eV, from equation (3.1). This temperature is much smaller than 75 eV obtained by the spectral analysis. Then, in order to take into account the electron scattering, we examine the true effective maximum

temperature by introducing the color temperature correction formula (Davis et al., 2006; Done et al., 2012):

$$f_{\text{col}} \sim \left(\frac{72}{kT/1\text{keV}} \right)^{1/9}. \quad (3.2)$$

When we applied the equation (3.2) to Ton S180, we obtain $f_{\text{col}} \sim 2.1$. This is close to the result of $f_{\text{col}} \sim 2.4$ reported in Ross et al. (1992). Calculating the true maximum effective temperature of Ton S180 with $f_{\text{col}} = 2.1$, we obtain $kT \sim 35$ eV, which agrees with the inner disk temperature of the standard accretion disk of $M_{\text{BH}} = 2 \times 10^7 M_{\odot}$ and $\dot{m} = 1$. Thus the soft X-ray excess of Ton S180 might be composed of the reflection component and the disk component where Comptonization of the disk emission could occur in the surface of the disk.

We obtained the result that the inclination angle of the disk 86.5° from the 0.25–55 keV spectral fit. Then we examined where the inclination angle is constrained with changing only the inclination angle. Figure 3.12 shows the comparison of the reflection model where the inclination angle is 30° , 60° , and 86.5° . There are differences among models in the 6–7 keV and 0.5–0.7 keV band. In this analysis, we found that Ton S180 has broad emission lines, He-like iron K and OVIII, which are modeled with the reflection component. Thus, in the case of Ton S180, the inclination angle is constrained by these two emission lines.

3.5.3 Absorbers, Reflectors, and Primary Source

We have obtained the emission models which reproduce the observed spectra of Ton S180 in the wide energy band of 0.25–55 keV, as summarized in table 3.1 and figure 3.4 and 3.6. The models consist of three components plus two kinds absorbers.

We attributed the absorption feature at 7.9 keV as an absorption by H-like iron with outflow velocity of $0.13c$, column density of $N_H \geq 10^{24} \text{ cm}^{-2}$, and the ionization parameter $\log \xi = 4.4_{-1.5}^{+0.4}$. Similar absorption features of highly ionized fast outflows were found in a number of sources, such as PG 1211+143 (Reeves et al., 2008) and PDS 456 (Reeves et al., 2009). For Ton S180, FUV absorption lines of OVI with FWHM of 2600 km s^{-1} were detected (Turner et al., 2002), but their blue shift velocity is 490 km s^{-1} much smaller than $0.13c$. The origin of the fast and highly ionized outflowing matter might be

the wind launched from the accretion disk, as is proposed in (Reeves et al., 2009) for PDS 456. However, the quality of our Ton S180 data is not sufficient to set firm upper limit of the absorption line width and its profile. At least in the case of PG 1211+143, the absorption profiles and energies changed in time. Therefore, repeated observations of Ton S180 might provide further clue to the origin of the absorber.

We introduced another absorber, Compton-thick partial absorber, to account for the hard X-ray excess observed with the HXD-PIN. As noted in section 3.3.1, the presence of such absorber is marginal, considering the systematic uncertainty of the HXD NXB modeling. We note, however, that similar hard X-ray excess was observed in other AGNs with Suzaku, e.g., 1H 0419–577 (Turner et al., 2009) and PDS 456 (Reeves et al., 2009), for which Compton-thick partial absorber was considered as a most likely origin of the feature. If the absorber is cold and Compton-thick, irradiation of the continuum emission must make fluorescence lines, particularly, iron K. We can roughly estimate the expected line intensity by integrating the photon flux absorbed above iron K edge as was done for MCG–6-30-15 by Reynolds et al. (2009). In our case, the absorbed photon flux integrated in 7.08–20 keV (source rest frame) range is 1.79×10^{-4} count s⁻¹. Multiplying the fluorescence yield of 0.35 makes expected iron K line flux of 0.63×10^{-4} count s⁻¹. This corresponds to the EW of neutral iron K line of 448 eV. According to Miller et al. (2009), based on their arguments on the MCG–6-30-15, the above calculation overestimate the line flux by about 6. Considering such a factor, the neutral iron K line flux expected is about twice the observed upper limit of 35 eV. This inconsistency is resolved, for example, the Compton-thick absorbers are preferentially located along the light of sight. We showed that the fractional variability has little energy dependence. That was found in the XMM-Newton observation of this source. As we described in the previous section, covering of the source by Compton-thick absorbers along the line of sight is one explanation for the spectral variability we observed.

The Compton-thick partial absorber might not be cold nor at rest. In particular, it is worth considering a possibility that patchy outflow of ionized matter unify the two kinds of absorbers we considered into one. Such a case can be tested with the XSPEC model `zxicpf`, which is based on `xstar v2.2`. We fitted the 0.25–55 keV spectra with a model in which `zpcfabs` and `gabs` in the first model (`diskbb` case) of table 3.1 are replaced with `zxicpf`. The

best fit parameters of $\log \xi = 6_{-1.6}^{+0.0}$, redshift $z = -0.06 \pm 0.01$, the column density $N_H = 381_{-310}^{+119}$ and the covering fraction $f = 1.0_{-0.6}^{+0.0}$ are obtained with $\chi^2/\text{dof} = 2238.8/2095$, which is larger than that in table 3.1. As the covering fraction of 1.0 means the absorber is uniform, the **zxipcf** model in this case should be equivalent to the **warmabs** model. In fact, their parameters are almost consistent with those obtained with **warmabs** model we tested at the end of section 3.3.1. The high ionization parameter of this absorber makes no apparent iron K edge nor hard X-ray hump. In fact, the **zxipcf** model with the parameters above can not reproduce the hard X-ray excess we observed. We need less ionized absorber for that. The absorber is not necessarily cold as we modeled with **zpcfabs**, though higher quality spectra will be required for detailed discrimination.

In the arguments above, however, the contributions of neutral iron K line from distant matter such as the absorption torus or the broad line clouds is neglected. Since Seyfert 1 galaxies almost universally have iron K emission from neutral matter (e.g., Nandra et al. (2007)), no detection (the upper limit of 35 eV) of the neutral iron K line in Ton S180 should be regarded as a special case. The strong ionization flux from the central source ionizes the clouds close to the central source is sometimes used as an explanation of the narrowness of the (optical) broad line in the NLS1 class. The small EW of the narrow neutral iron K line can be explained toward this direction. However, it requires the height of the accretion torus must be smaller in Ton S180 than typical Seyfert galaxies, too. It implies that the unification model of Seyfert galaxies may not be appropriate for this source at least in its exact form.

Relative intensity of the reflection component and the power-law component should be determined by the geometry. The normalization of the reflection component **reflionx** is, however, difficult to be directly compared with the power-law component. We thus refer the relative model fluxes at 30 keV as a rough measure of the contribution. The ratio of the reflection component flux to the power-law component flux is 0.46 in our model including the disk blackbody component (figure 3.4). Magdziarz & Zdziarski (1995) demonstrated the reflection flux strongly depends on the viewing angle in their calculation of the reflection from neutral matter with semi-infinite slab geometry. They studied reflection spectra with viewing angle of 18.2° , 63.3° , 75.5° , and 87.1° . Referring their study, we know the flux ratio at 30 keV of 0.46 is obtained with the viewing angle between 63.3° and 75.5° . On the other

hand, the viewing angle of 87.1° leads to the ratio at 30 keV of about 0.11. If the inclination angle close to 90° (edge-on geometry) obtained in the spectral fit (table 3.1) is correct, the intensity of the reflection is factor of 4 higher than expected. We note that the flux ratio reflection/power-law at 30 keV is about 2 in the case of MCG–6-30-15 (Reynolds et al., 2009). We might need more sophisticated geometry of source and reflector, too.

We finally mention on the power-law component, usually assumed as the primary emission. The component is sometimes assumed to be from accretion corona located above the disk via thermal Comptonization. We found the power-law photon index Γ is 2.2–2.4, relatively steeper than the typical value for BLS1s. The equation $\Gamma = \sqrt{9/4 + 4/y} - 1/2$ (e.g. section 7.7 of Rybicki & Lightman (1979)) leads to $y \equiv 4kT_e/(m_e c^2) \text{Max}(\tau, \tau^2) = 0.72$. In this expression, T_e is the electron temperature of the corona, which should be determined from the high energy cutoff in the hard X-ray spectrum. We could not get firm value for Ton S180 in our observations. However, if kT_e is around 100 keV, the optical depth of the corona is $\tau = 0.92$, almost unity.

3.6 Summary

The wide-band (0.25–55 keV) X-ray spectra of Ton S180 observed with Suzaku is modeled with three components, the power-law component, the reflection from highly ionized disk component, and the extra soft component either of disk blackbody or cutoff power-law. The reflection component accounts for the broad iron K line centered at 6.7 keV, and some fraction of the soft X-ray excess, including the OVIII line emission. The last two components contribute comparably to the soft X-ray excess. Consequently, when we take the disk blackbody model as the extra soft component, the disk inner radius temperature becomes 75 eV, much smaller than previously considered, and feasible as a model if we base on the slim-disk model and assuming edge-on geometry. Hard X-ray flux above 15 keV was detected for the first time but marginally. To account for the hard X-ray spectrum, we introduced Compton-thick partial absorbers. Absence of the neutral iron K line requires those absorbers must be preferentially located along the line of sight.

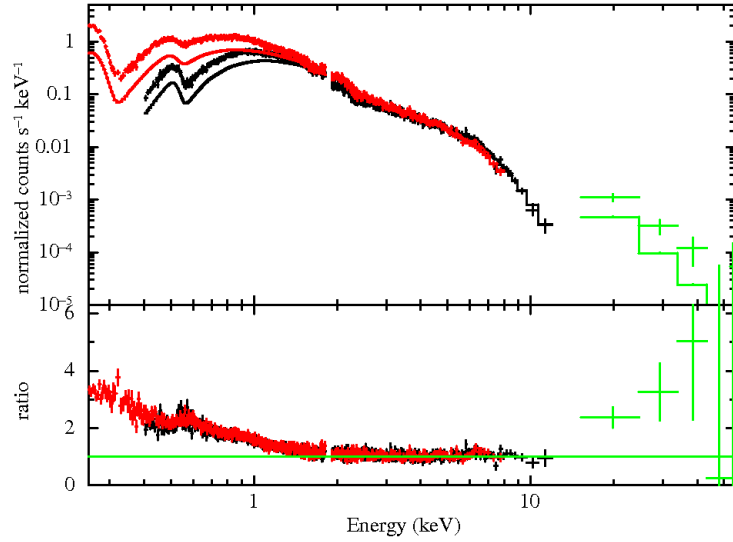


Figure 3.1: Time averaged (0.25–55 keV) Suzaku spectra of Ton S180. Data from the XIS-FI, XIS-BI, and HXD-PIN are shown in black, red, and green, respectively. A simple power-law model fitted in 2.5–10 keV range is compared. The upper panel shows the photon spectra, while the lower one shows the spectral ratio to the simple power-law model. Excess emission over the simple power-law model is clearly visible below 2 keV and above 10 keV. An emission line and an absorption feature are also visible in the 6–8 keV range.

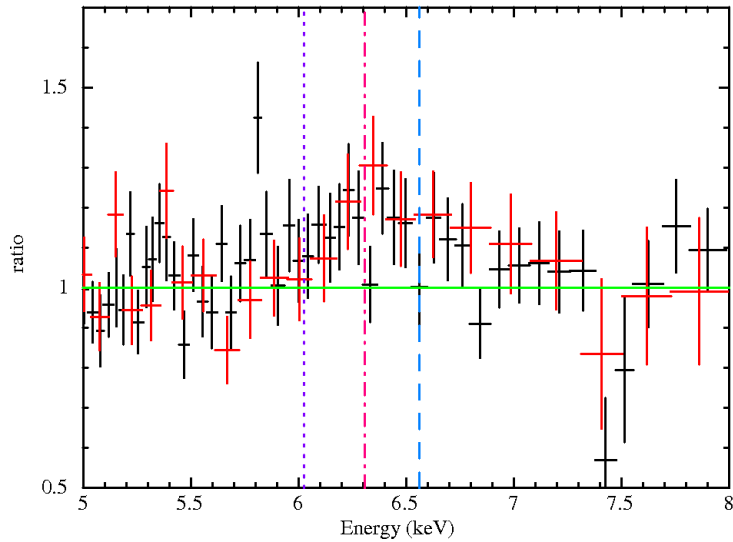


Figure 3.2: Iron K band spectra of Ton S180. The figure is a 5–8 keV zoom in of the spectral ratio plot shown in the lower panel of figure 3.1. XIS-FI and XIS-BI data are represented in black crosses and red ones, respectively. The expected energies of the neutral (purple dotted line), He-like (light red dat-dashed line), and H-like (light blue dashed line) iron are indicated.

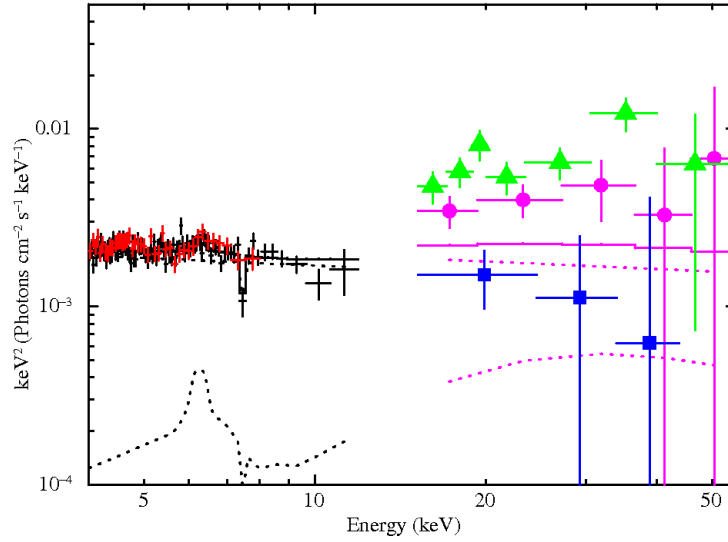


Figure 3.3: The spectral fit to the 4–55 keV energy band spectra with a model consisting of a power-law component plus the relativistically blurred reflection component. The unfolded spectra multiplied by energy squared are shown. Data from the XIS-FI, XIS-BI are shown in black and red, respectively. Filled circles in magenta are the HXD-PIN spectrum from which the CXB and the nominal NXB are subtracted. Blue squares and green triangles are the HXD-PIN spectra for which NXB model with alternate normalization by -3% and $+3\%$ of the NXB, respectively, in order to see systematic uncertainty. The reflection component model underestimates the HXD-PIN spectrum at least with the nominal NXB model or the -3% NXB model.

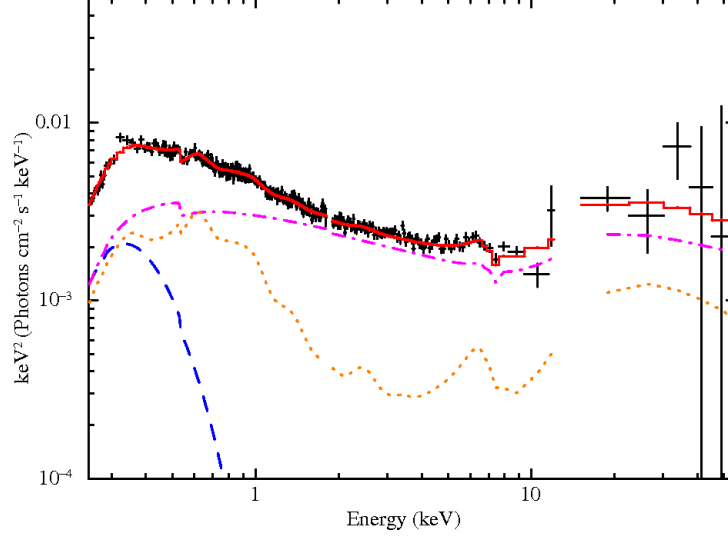


Figure 3.4: Time averaged (0.25–55 keV) Suzaku spectra of Ton S180 fitted with the model including the disk blackbody component. The unfolded spectra in the form of $E^2I(E)$ are displayed. Black points with error bars are the data from the XIS and the HXD-PIN. Spectra are rebinned for display, and the XIS-BI spectrum above 1.9 keV and the XIS-FI spectrum below 1.8 keV are not displayed for clarity. The model curve for the total is plotted in red lines (solid), while the power-law continuum in magenta (dot-dashed), the disk blackbody component in blue (dashed), and the reflection component in orange (dotted). The best-fit parameters are listed in the column labeled `diskbbin` in table 3.1.

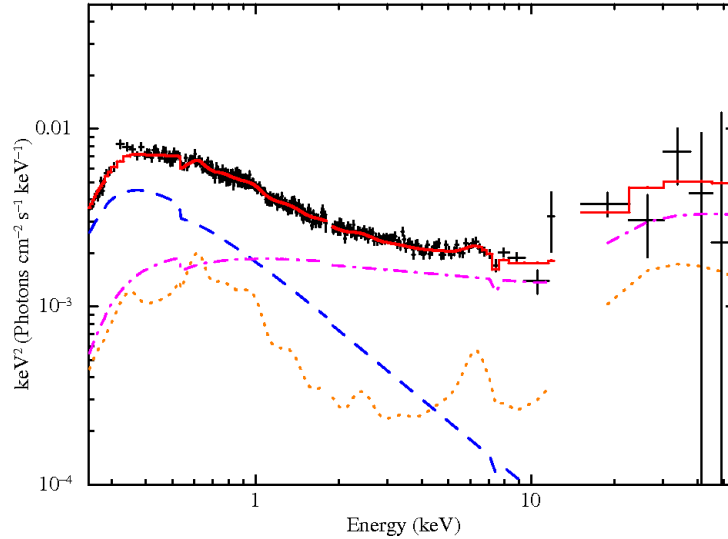


Figure 3.5: Time averaged (0.25–55 keV) Suzaku spectra of Ton S180 fitted with the model including the second power-law component. The unfolded spectra in the form of $E^2I(E)$ are displayed. The same colors and lines are used as in figure 3.4, except that the second power-law component is plotted in blue dashed line. The best-fit parameters are summarized in the column labeled `powerlaw` in table 3.1.

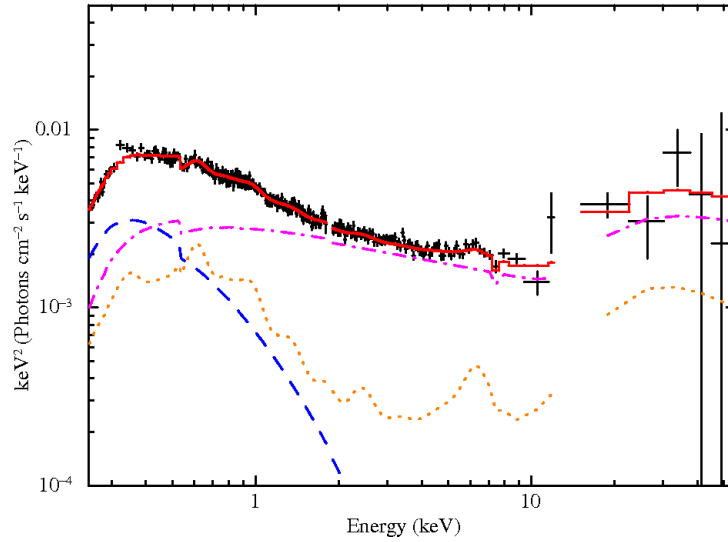


Figure 3.6: Time averaged (0.25–55 keV) Suzaku spectra of Ton S180, with unfolded spectrum in $E^2 I(E)$. We use the power-law with high energy cutoff model for the soft X-ray excess. The same colors and lines are used as in figure 3.4, except that the cutoff power-law component is plotted in blue dashed line. The best-fit parameters are summarized in the column labeled `cutoffpl` in table 3.1.

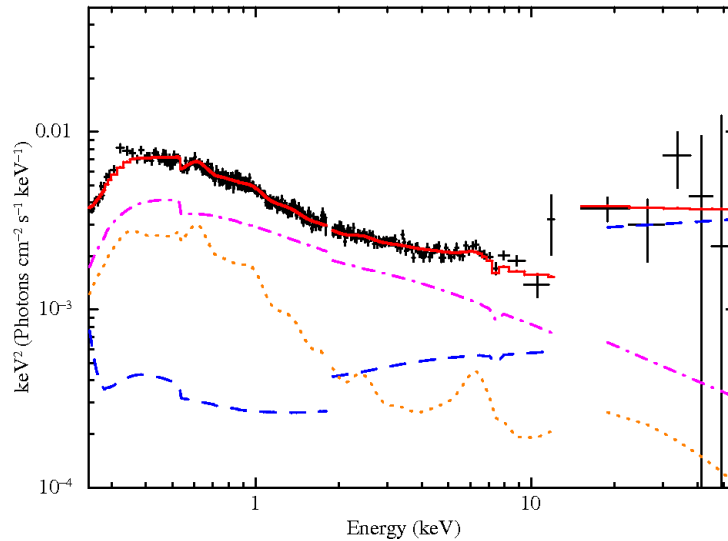


Figure 3.7: Time averaged (0.25–55 keV) Suzaku spectra of Ton S180, with unfolded spectrum in $E^2 I(E)$. We use the Comptonized blackbody model for the soft X-ray excess. Symbols are the same as figure 3.4 except that the Comptonized blackbody is plotted in blue dashed line. The best-fit parameters are summarized in the column labeled `compbb` in table 3.1.

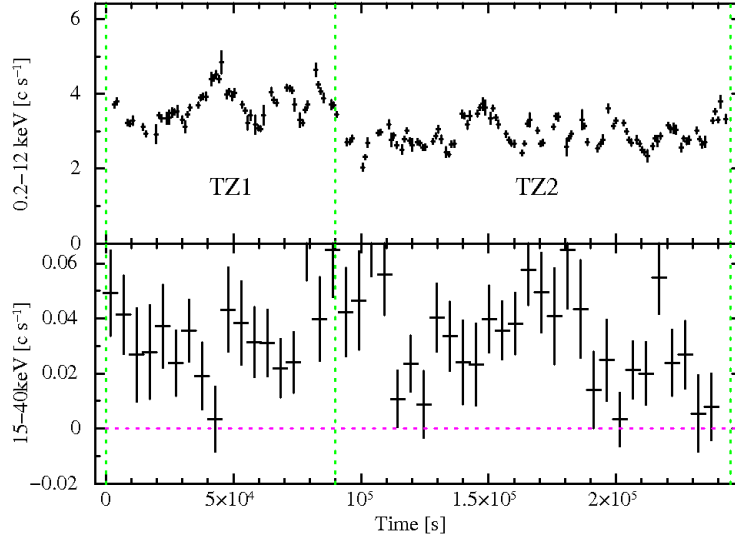


Figure 3.8: The light curve in the 0.2–12 keV band obtained from the XIS and in the 15–40 keV band obtained from the HXD-PIN. The time bin size is 1024 s for the XIS light curve, while that for the HXD-PIN is 5120 s. The background subtracted counting rates from the three XIS(0,1,3) sensors are combined to make the XIS light curve. The data from the HXD-PIN is dead time corrected, and background (NXB and CXB) subtracted. The origin of the time is MJD of 54078.5747. We divided the whole time span into two time zones, TZ1 and TZ2.

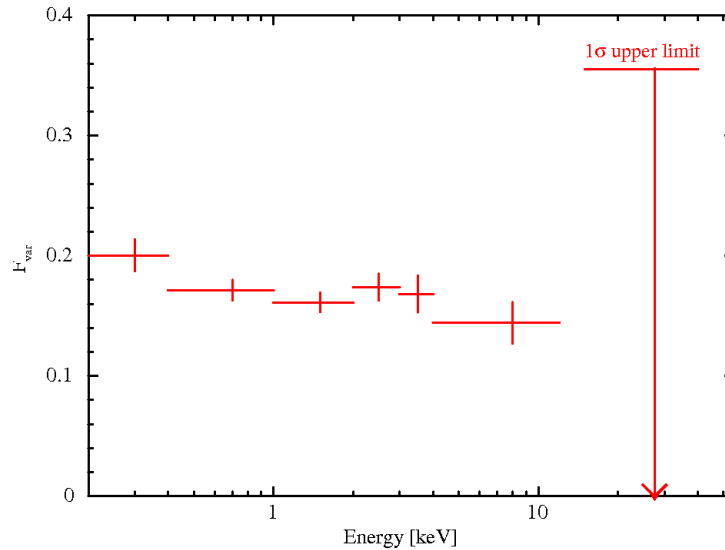


Figure 3.9: The RMS fractional variability of Ton S180 over the entire observation. The time bin size of the light curves was 512 s. The RMS fractional variability of the 15–40 keV band is not well constrained, and the 1σ upper limit is shown in the figure.

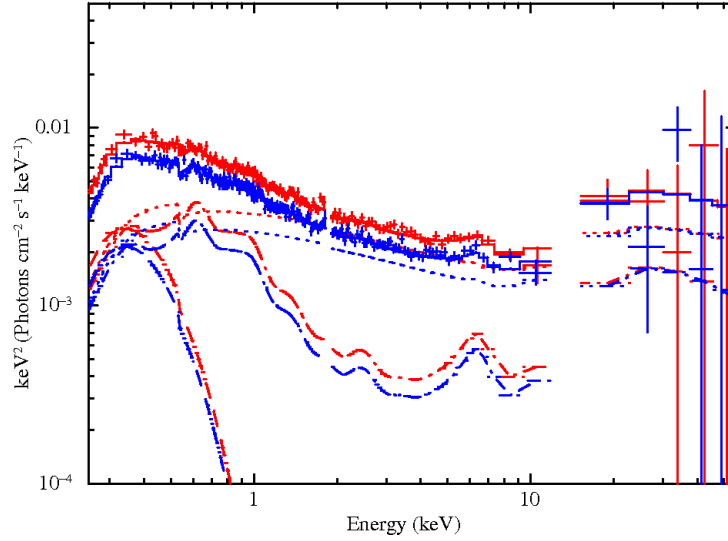


Figure 3.10: Comparison of TZ1 spectra (red) and TZ2 spectra (blue). The emission model is $wabs \times gabs \times zpcfabs \times \{ diskbb + powerlaw + kdblur \times reflionx \}$, used in figure 3.4, but with different partial covering fractions, $0.37^{+0.07}_{-0.21}$ for the TZ1 and $0.50^{+0.06}_{-0.15}$ for the TZ2. Dotted lines, dot dashed lines, and dashed lines indicate the power-law, reflection and disk blackbody component, respectively.

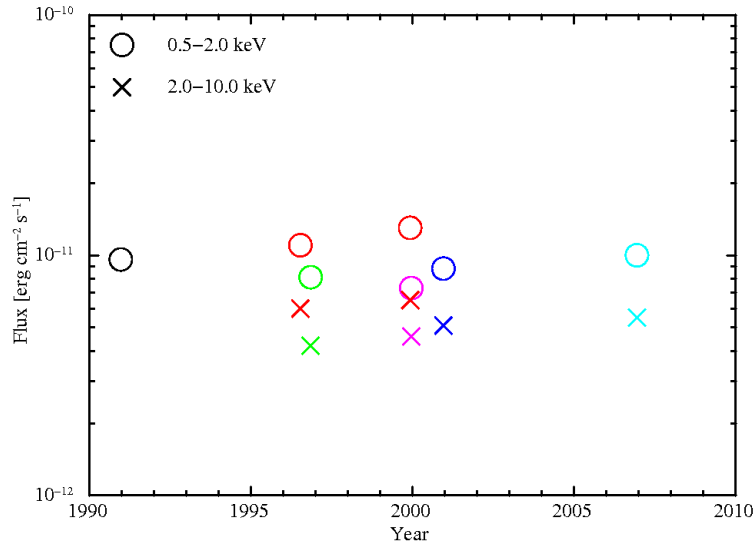


Figure 3.11: X-ray flux of Ton S180 measured in 1990–2006. Unabsorbed fluxes in 0.5-2 keV (open circles) and 2-10 keV (crosses) are plotted. Data point from ROSAT (Fink et al., 1997) is colored in black, ASCA (Turner et al., 1998, 2001; Romano et al., 2002) in red, Chandra (Rózańska et al., 2004) in magenta, Beppo-SAX (Comastri et al., 1998) in green, XMM-Newton (Vaughan et al., 2002) in blue, and Suzaku in cyan.

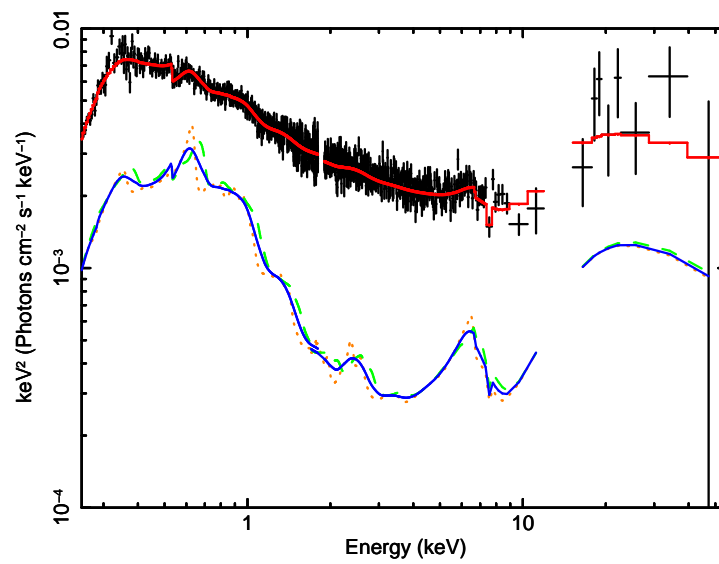


Figure 3.12: The 0.25–55 keV X-ray spectra (black crosses) and the reflection component model. The red solid curve is the same as figure 3.4. The blue solid curve, orange dotted curve, and green dashed curve represent the reflection model in which the inclination angle are 86.5° (`diskbb` in table 3.1), 30° , and 60° , respectively.

Table 3.1: Spectral fit to the time-averaged wide-band (0.25–55 keV) spectra of Ton S180. Extra components are tested in addition to the spectral model employed in section 3.3.1 to reproduce the soft X-ray excess. The model is schematically expressed as $\text{wabs} \times \text{gabs} \times \{ \text{extra component} + \text{powerlaw} + \text{kdblur} \times \text{reflionx} \}$, where extra component is either diskbb , powerlaw , cutoffpl , or compbb .

Model	Parameter	Unit	extra component Model			
			diskbb	powerlaw	cutoffpl	compbb
diskbb	T_{in}	keV	$0.075^{+0.002}_{-0.003}$
powerlaw	Γ_{soft}		...	$3.29^{+0.11}_{-0.07}$
cutoffpl	Γ_{soft}		$3.2^{+0.3}_{-0.2}$...
	E_{cut}	keV	$1.0^{+0.6}_{-0.2}$...
compbb	kT_e	keV	68^{+22}_{-18}
	kT_{ph}	keV	$0.01(\text{fix})$
	τ		$0.16^{+0.07}_{-0.06}$
zpcfabs	N_H	10^{22} cm^{-2}	...	664^{+803}_{-287}	550^{+1086}_{-301}	5.6 ± 1.1
	CvrFract		$0.58^{+0.08}_{-0.10}$	$0.63^{+0.12}_{-0.26}$	$0.67^{+0.11}_{-0.16}$	0.24 ± 0.03
powerlaw	Γ_{hard}		$2.38^{+0.01}_{-0.02}$	$2.24^{+0.06}_{-0.04}$	2.29 ± 0.03	2.65 ± 0.02
kdblur	$R_{in}(\text{G})$		20^{+5}_{-4}	27^{+19}_{-4}	25^{+8}_{-5}	25^{+8}_{-5}
	Incl	deg	$86.5^{+0.8}_{-0.2}$	90^{+0}_{-33}	$86.8^{+0.0}_{-0.4}$	90^{+0}_{-34}
reflion	Fe/solar		$1.06^{+0.10}_{-0.12}$	1.3 ± 0.3	1.0 ± 0.1	0.9 ± 0.1
	ξ	ergs $\text{s}^{-1} \text{ cm}$	488^{+28}_{-46}	288^{+27}_{-20}	406^{+104}_{-70}	1142^{+165}_{-172}
	χ^2/dof		$2215.8/2092$	$2229.5/2092$	$2216.9/2091$	$2260.9/2091$

Chapter 4

The Hard X-ray emission in Narrow Line Seyfert 1 Galaxies: Mrk 110, SWIFT J212745.6+565636, and IGR J16185–5928

4.1 Introduction

X-ray spectra of radio quiet active galactic nuclei (AGN) show complex spectral features over a baseline continuum. The spectral features are originated in absorption or reprocessing processes occurring in matters surrounding a central super massive black hole (SMBH), and hence useful to diagnose them from observations. The primary emission is, on the other hand, usually assumed to be a simple primary power-law with a high energy cutoff. There is a widely accepted belief that this primary emission is due to thermal Comptonization of soft photons from an accretion disk via thermal electrons of about 10^9 K in an accretion corona. The temperature of the electrons is evaluated from high energy cutoff observed in bright Seyfert galaxies.

Zdziarski et al. (2000) investigated 50–500 keV hard X-ray spectra obtained with the Oriented Scintillation Spectroscopy Experiment (OSSE) aboard the Compton Gamma Ray Observatory (CGRO). They averaged spectra of Seyfert 1 galaxies (except for NGC 4151) and Seyfert 2 galaxies, respectively. They obtained the cutoff energy E_C of 60–340 keV for Seyfert 1 and 80–350 keV for Seyfert 2, where the fitting model of $F(E_X) = N \times E_X^{-\Gamma} \exp(-E_X/E_C)$ was employed. The photon index Γ is constrained to 1.5–2.2 for Seyfert 1 and 1.5–1.9 for Seyfert 2. Note that this e-folding cutoff energy E_C is different by about factor of 2 from the electron temperature kT_e when thermal

Comptonization is assumed. In fact, Zdziarski et al. (2000) showed kT_e is constrained as 40–170 keV for Seyfert 1 and 50–170 keV for Seyfert 2. For NGC 4151 kT_e is 50–80 keV. BeppoSAX observations of 6 Seyfert galaxies are examined in detail by Petrucci et al. (2001), and $kT_e=20\text{--}100$ keV was obtained. Perola et al. (2002) studied the BeppoSAX 0.1–200 keV spectra of 9 type 1 AGNs for each, and found the cutoff energies E_C spans from about 80 to more than 300 keV. Molina et al. (2009) investigated the hard X-ray spectra of 36 type 1 AGNs detected with IBIS/ISGRI aboard the INTEGRAL satellite. The mean cutoff energy is around 100 keV. Suzaku have also provided the high quality hard X-ray spectra of several sources. The cutoff energies of 80–160 keV for 4C 50.55 (Tazaki et al., 2010), and 40–100 keV for NGC 5506 (Soldi et al., 2011), are obtained, respectively.

These observations, and the fact that a standard (optically thick geometrically thin) accretion disk can account for a UV bump but fail to explain the X-ray emission, have made the thermal Comptonization model as the most plausible explanation for the primary X-ray emission in radio quiet AGNs. The location of an accretion corona is not obvious, either above the accretion disk (horizontal separation) or inner region very close to the central SMBH where disk is truncated (vertical separation). The latter case is sometimes called as inner hot-flow model, distinguished from the former one. Theoretical and computation studies also have been extensively made. Haardt & Maraschi (1991), who introduced disk-corona (two phase) model to account for X-ray spectra of AGNs, demonstrated that substantial fraction of energy is dissipated within a corona, whereas most of accreting material is retained within the main body of a disk. They introduced a parameter f , which represents a fraction of the gravitational energy dissipated in a corona via buoyancy and reconnection of magnetic fields out of the disk main body. To account for the observed power-law component in X-ray band, they show f should be close to unity. Various effects are considered and taken into account in recent theoretical studies, (e.g., Kawabata & Mineshige (2010); Veledina et al. (2011); Qiao & Liu (2012); Meyer-Hofmeister et al. (2012); Liu et al. (2012)), and numerical simulations are employed, e.g., Kawanaka et al. (2008).

The hard X-ray spectra of radio quiet AGN cited above are mostly broad line Seyfert 1 galaxies (BLS1s). Malizia et al. (2008) provided hard X-ray spectra of 5 narrow line Seyfert 1 galaxies (NLS1s), though some of the sources have larger H_β width than 2000 km/s. They averaged the spectra of 5 NLS1s

and obtained a steeper photon index ($\Gamma = 2.6 \pm 0.3$) and a lower cutoff energy ($E_C = 38_{-10}^{+17}$ keV) than typical BLS1 sources so far observed. NLS1s are considered to have lower mass BH and higher accretion rate (normalized to its critical rate) than those of BLS1s. Therefore, if this trend is confirmed, it will be a key to understand the accretion process in SMBHs with various input parameters.

With this motivation, we study three hard X-ray bright NLS1 sources observed with Suzaku. Hard X-ray spectra of NLS1s have been already obtained for NGC 4051 (Terashima et al., 2009) and Ton S180 (Takahashi et al. (2010); chapter 3 in this thesis), though the cutoff energy could not be well constrained. The three NLS1s studied in this thesis are Mrk 110, SWIFT J212745.6+565636, and IGR J16185–5928. These three have highest hard X-ray (15–195 keV) flux among the NLS1 sources listed in the catalog of the 58 months Swift-BAT all sky hard X-ray survey (Baumgartner et al., 2010), and were included in the Suzaku archive. We adopt cosmological parameters of $H_0 = 70 \text{ km s}^{-1}$, $q_0 = 0.0$, and $\lambda_0 = 0.73$.

4.2 Observations

Table 4.1 lists three targets we study in this paper. The observations of these targets were carried out with the X-ray Imaging Spectrometer (XIS: Koyama et al. (2007)) and the Hard X-ray Detector (HXD: Takahashi et al. (2007); Kokubun et al. (2007)) aboard Suzaku (Mitsuda et al., 2007). The XIS consists of four CCD cameras: three (XIS 0, XIS 2, XIS 3) with front illuminated (XIS-FI) CCDs and one (XIS 1) with a back illuminated (XIS-BI) CCD. XIS 2 was not available after 2006 November 9, and the other three CCDs were used in observations. Furthermore, only XIS 3 camera was available for the Suzaku observation of SWIFT J212745.6+565636 since the XIS 0 camera was not operating properly (Miniutti et al., 2009a; Patrick et al., 2011). The normal full-window clocking mode with the spaced-row charge injection (SCI: Uchiyama et al. (2009)) was employed. The XIS edit mode was either in 3×3 or in 5×5 , and the data of both modes were combined in our analysis. The HXD was operated normally in the observations, and the target was placed at the nominal center of HXD field of view.

We reprocessed the XIS data by using the latest CALDB as of 2010 July. The same data-selection criteria as that used for the archived cleaned event

lists were employed. We further restricted the time interval in which both the XIS and HXD data were available simultaneously for our analysis.

All the Suzaku data in this paper were reduced using the HEASOFT reduction and analysis package (version 6.10). Each XIS source spectrum was extracted from the circular region of $3'$ radius centered upon the source. Each background spectrum was extracted from the circular region of $3'$ radius in which there is no source. In figure 4.1, we showed the source and background regions for Mrk 110. Other sources were taken care in a similar way.

For all the targets, the redistribution matrices and the ancillary response files were made for each XIS spectra using `xisrmfgen` and `xissimarfgen`, respectively. XIS spectra from the FI CCDs were combined by using `mathpha`. Correspondingly, the redistribution matrices and the ancillary response files for the FI CCDs were combined by using `addrmf` and `addarf`, respectively.

We followed the standard data reduction procedure for the Si PIN diode (HXD-PIN) data, including dead-time corrections. For the HXD-PIN non X-ray Background (NXB), we used a simulated event file supplied by the HXD team based on LCFITDT model (Fukazawa et al., 2009). The Cosmic X-ray Background (CXB) component was evaluated and subtracted by using the empirical model by Boldt (1987), i.e., $9.412 \times 10^{-3} (E/1 \text{ keV})^{-1.29} \exp(-E/40 \text{ keV})$ photons $\text{cm}^{-2} \text{ s}^{-1} \text{ keV}^{-1} (2^\circ \times 2^\circ)^{-1}$. We simulated the CXB component with this spectral model and the HXD response file for this uniform diffuse emission, and added to the NXB component to make the total background spectrum. The HXD-PIN response file for a point source at the HXD nominal position, `ae_hxd_pinplate4_20080129.rsp`, was used in the spectral analysis. The result of HXD-PIN data reduction is shown in figure 4.2.

In order to examine the systematic error in the NXB model spectra, we compared them with the NXB spectra obtained when the telescope FOV was occultated by the dark Earth. We obtained such dark Earth data with exposures about 22 ks for both periods of the observations of Mrk 110 and SWIFT J212745.6+565636, while no such data were obtained during the observation of IGR J16185–5928. We summarize the HXD-PIN NXB count rates for the observations of Mrk 110 and SWIFT J212745.6+565636 in table 4.2. We found that the NXB model for Mrk 110 is weaker than that obtained during the Earth occultation by 1%, while that for SWIFT J212745.6+565636 is higher by 2%. Thus, in fitting the X-ray spectra, we evaluated how the systematic errors in the NXB model affect the fitting results by changing the

NXB level by +1% and -2%, for Mrk 110 and SWIFT J212745.6+565636, respectively. For IGR J16185-5928, we performed the spectral fit with the NXB level changing by $\pm 3\%$ to see the effect, as was done in the data analysis of Ton S180 (Takahashi et al., 2010).

4.3 Spectral Analysis

4.3.1 2.5–12 keV X-ray Spectrum

We first apply a single power-law model modified by the Galactic absorption to the 2.5–12 keV energy band. The 4.5–7.5 keV energy band are ignored to avoid the Fe emission line. In figure 4.3 we show the spectral ratios between the data and the model in the 0.25–40 keV energy band. We should note the soft excess structures in Mrk 110 and IGR J16185-5928, while the hard excess structures in SWIFT J212745.6+565636 and IGR J16185-5928.

In figure 4.4 we show the zoom-up the spectral ratio in the 4–7 keV energy band. All targets have the emission-like features around 6.4 keV of the source rest-frame. When we added a Gaussian model, we obtained the acceptable fit of all targets including the 4.5–7.5 keV energy band, as summarized in table 4.3. The line center energies of all targets are consistent with 6.4 keV, i.e., neutral iron K_α line, while the line has a significant width for SWIFT J212745.6+565636. The emission lines observed in Mrk 110 and in IGR J16185-5928 are likely from distant and cold materials such as a molecular torus or an optical broad line region, while that in SWIFT J212745.6+565636 might be from vicinity of the central BH.

4.3.2 2.5–40 keV X-ray Spectrum

We next examine the 2.5–40 keV X-ray spectra using XIS+HXD-PIN data. The detection of the Fe emission line suggests that the hard excess is due to the reflection hump. We hence investigate the strength of this component using a Xspec model, `pexmon` (Nandra et al., 2007). This model includes parameters such as the cutoff energy and the relative strength of the reflection component to the power-law component as well as `pexrav` (Magdziarz & Zdziarski, 1995). However, in this model, the EW of Fe K_α line depends on the photon index of the incident power-law, the inclination of the slab, and the abundance of iron relative to the other elements.

In fitting the X-ray spectrum in the 2.5–40 keV using the `pexmon` model, we allow the photon index of the power-law, cutoff energy E_C , the relative reflection strength R , and the normalization to vary. We note that R is defined as $R = \Omega/2\pi$, where Ω is the solid angle of a cold reflector viewed from an X-ray source. On the other hand, the inclination angle, elemental abundance, and Fe relative abundance to the solar one are fixed at 30° , 1, and 1, respectively. We summarize the result of the spectral fit and the best-fit parameters in figure 4.5 and table 4.4, respectively.

Figure 4.5 shows that the X-ray spectrum of Mrk 110 is reproduced with the `phabs` \times `pexmon` model. Although the X-ray spectrum of IGR J16185–5928 show some deviation from the model in the 15–40 keV range, the deviation is within the systematic uncertainty of HXD-PIN NXB. On the other hand, for SWIFT J212745.6+565636, the model does not reproduce the spectrum not only in the hard energy band but also in the Fe band. In order to improve the fit for SWIFT J212745.6+565636, we introduce a neutral partial covering absorption model, `zpcfabs` and refitted. As a result, we are able to explain the 2.5–40 keV spectrum of SWIFT J212745.6+565636, as shown in figure 4.6 and 4.7.

4.3.3 0.25–40 keV X-ray Spectrum

Extrapolating the model determined in the 2.5–40 keV energy band to the 0.25–40 keV band, excess structures below 1 keV, which should be called as soft X-ray excess, are seen in 3 objects, as shown in figure 4.8. While those of Mrk 110 and IGR J16185–5928 are prominent, that of SWIFT J212745.6+565636 is less remarkable. We add a blackbody model (`zbody`) as an empirical model to represent the soft X-ray excess. This make the fit to the 0.25–40 keV X-ray spectra of SWIFT J212745.6+565636 and IGR J16185–5928 better.

The spectral fit for Mrk 110 is summarized in figure 4.9 and table 4.5. When we add a blackbody model in the soft X-ray excess, the cutoff energy is constrained only with its lower limit of 1040 keV, and the Γ is steeper than that determined in the 2.5–40 keV band. We hence retry the spectral fit with replacing the blackbody model with another power-law (`powerlaw`) or a cutoff power-law (`cutoffpl`). The best-fit model and parameters are summarized in figure 4.9 and table 4.5 as well. In the case of the power-law model, the photon index is much flatter than that determined in the 2.5–40 keV. On the other hand, in the case of the cutoff powerlaw model, the cutoff energy

and the photon index are consistent with those determined in the 2.5–40 keV band. We thus adopt the cutoff power-law model to reproduce the soft excess of Mrk 110.

As mentioned in section 4.2, the NXB model spectra for Mrk 110 and SWIFT J212745.6+565636 differ from the dark Earth spectra by -1% and $+2\%$, respectively. Since the cutoff energy might be affected by the HXD-PIN NXB level estimated, we examine its effect by increasing or decreasing the HXD-PIN NXB level by that amount. For IGR J16185–5928, we test the HXD-PIN NXB level changing by $\pm 3\%$. Each best-fit model and parameter are summarized in figure 4.10, 4.14, 4.18, and table 4.6, 4.7, 4.8, respectively. We find that the cutoff energies of 3 NLS1s are little affected by the HXD-PIN NXB level uncertainty we evaluated.

We have obtained the photon index Γ and the cutoff energy (E_C) with the spectral fit in the 0.25–40 keV band. We can calculate the electron temperature (kT_e) and the optical depth (τ) of the corona by replacing the cutoff power-law model into the thermal Comptonized model (Zdziarski et al., 1996). The optical depth τ is calculated with the following equation (Petrucci et al., 2001):

$$\tau = \sqrt{2.25 + \frac{3}{(kT_e/511 \text{ keV})((\Gamma + 0.5)^2 - 2.25)}} - 1.5. \quad (4.1)$$

We show 90% contours of the optical depth versus the cutoff energy in figure 4.13, figure 4.17, and figure 4.21. The contour plots of Mrk 110 and SWIFT J212745.6+565636 show that both sources have the electron temperature $kT_e < 50$ keV and the optical depth $\tau > 2$ at 90% significant level for 2 interesting parameters. On the other hand, only the lower limit of 150 keV is obtained for IGR J16185–5928.

4.4 Discussion

We have studied the X-ray spectra of 3 NLS1s, Mrk 110, SWIFT J212745.6+565636, and IGR J16185–5928 observed with Suzaku. The wide-band (0.25–40 keV) spectra are reproduced with a model consisting of three components: the power-law component, the reflection component, and the soft X-ray excess component, which is modeled either with a blackbody or cutoff power-law model. We find that for Mrk 110 and SWIFT J212745.6+565636, the cutoff

energies are constrained below 100 keV even when the uncertainty of HXD-PIN NXB model is taken into account. On the other hand, only the lower limit of 240 keV is obtained for IGR J16185–5928. In terms of the electron temperatures of the accretion corona, kT_e is constrained between 10–30 keV for Mrk 110 and SWIFT J2127.4+5654. The optical depth τ and the Compton y parameter are calculated with the equation (4.1) and the following equation (Rybicki & Lightman, 1979):

$$(\Gamma - 1)(\Gamma + 2) - \frac{4}{y} = 0 \quad (4.2)$$

We summarize these parameters obtained for the 3 NLS1s in table 4.9. We compare these results with previous observations of BLS1s and NLS1s, and also with some theoretical models below.

Before focusing on the high-energy cutoff, we have some note on lower energy part. We have modeled the soft X-ray excess with a blackbody or cutoff power-law model for our target in this paper. We previously showed the soft X-ray excess is modeled together with a multi-color disk temperature model plus a reflection from an ionized matter for the NLS1 Ton S180 Takahashi et al. (2010). The multi-color disk temperature of Ton S180 is hence as low as 75 eV, while the blackbody temperatures of the 3 NLS1s in this paper range 110–230 eV. Including an additional reflection component may alter this result, but we leave that for future task. The spectra of the 3 NLS1s are also different at iron K band from that of Ton S180; the line center energies for the 3 NLS1s in this paper are consistent with 6.4 keV, but that for Ton S180 is as high as 6.7 keV. Therefore, the parameters of the additional reflection component may be different from that in the Ton S180 case.

Comparison with Previous Results on BLS1s and NLS1s

We have obtained electron temperatures as low as 10–30 keV for 2 NLS1s in our sample, which are lower than those of BLS1s obtained in previous experiments mentioned in the introduction, for example, 40–170 keV for Seyfert 1 in Zdziarski et al. (2000). On the other hand, two NLS1s among three in our sample, SWIFT J212745.6+565636 and IGR J16185–5928 are included in the five NLS1 sources observed with INTEGRAL by Malizia et al. (2008). The cutoff energies obtained for these two sources by us are consistent with those obtained by Malizia et al. (2008).

In order to examine the systematic difference between the hard X-ray spectral parameters in NLS1 and BLS1 or any kind of trends, we employ the results from the INTEGRAL satellite, for BLS1 by Molina et al. (2009) and for NLS1 by Malizia et al. (2008). We convert the cutoff energy and cutoff the power-law photon index into the thermal Comptonization model parameters, Γ_{Comp} , kT_e , the Compton y parameter, and τ by the same way as described in section 4.3.

We also calculated the mean and weighted mean of these parameters. In calculating, for the lower limit of the cutoff energy, we calculated by the following way. We assumed the best-fit value and its 1σ error to be the half of value adding 511 keV to the lower limit and the difference between the best-fit value and the lower limit, respectively. On the other hand, for the data constrained significantly, we used the value obtained from spectral analysis as the best-fit value and we regarded the mean of the absolute value of "–" error and "+" error as the 1σ error. We calculated other parameters by the same way. For the optical depth τ , since it is clear that when the electron energy is lower limit, τ becomes upper limit from equation (4.1), we assumed the 1σ error to be half of the upper limit.

We summarize the values in table 4.10. The mean and weighted mean of kT_e , y , and τ are shown in table 4.11. The plot of the electron temperature versus the photon index is displayed in Figure 4.23. This plot indicates a trend that NLS1s have lower electron temperatures and steeper power-law index than BLS1s. Nevertheless, a statistical test is not easy with several sources in which only lower limits are obtained, and the limited number of NLS1 sources.

Since we assume the cutoff power-law component is due to thermal Comptonization of soft photons from an accretion disk, the luminosity of these two components are also key parameters. If we assume the modeled soft X-ray excess represents the disk component, as a baseline, we can derive the luminosity of both component from our fitting results for the 3 NLS1s in our sample. On the other hand, for the sample in Malizia et al. (2008) and Molina et al. (2009), since soft X-ray data are not available at least in these papers, the disk (or soft X-ray excess) component are difficult to be evaluated.

We hence attempt to estimate the UV to soft X-ray spectra of those sources by employing the template SED of Seyfert galaxies by Jin et al. (2012). We use the SED template of 5-A and 5-C in Jin et al. (2012) for NLS1 and BLS1,

respectively, and fit them with a two component model, consisting of a UV to soft X-ray excess component (SE) and a power-law component (PL). We show each modeled SED in figure 4.22 and the input parameters in table 4.12. Using this remodeled SED, the flux ratios of the two components ($F_{\text{SE}}/F_{\text{PL}}$) at $E = 0.5 \text{ keV}$ are 3.54 for NLS1 and 7×10^{-3} for BLS1, respectively. Employing this modeled SED, we reproduce the UV to the soft X-ray excess component for the BLS1 in Molina et al. (2009) and NLS1 in Malizia et al. (2008), and derive the luminosities in the 1–500 keV band and 10^{-3} –0.1 keV band. We denote the former as L_{X} and the latter as L_{UV} here. For the 3 NLS1s in our study, we derive L_{X} and L_{UV} from our results of spectral fit. L_{X} , L_{UV} and those ratio are listed in in table 4.13. In the same table, we list the SMBH mass for each object, cited from Masetti et al. (2006, 2008, 2009); Khorunzhev et al. (2012). Note that these masses are derived from SMBH mass and parameters of optical emission line (line width and luminosity) relation empirically and might have uncertainties of a factor of a few. The bolometric luminosity of each object listed in the table is derived from the 2–10 keV luminosity multiplied the bolometric factor of the same energy band. We use the 2–10 keV bolometric factor of 91 (5-A) and 18 (5-C) in Jin et al. (2012) for NLS1s and BLS1s, respectively.

Figure 4.24, 4.25, and 4.26 show kT_e , τ , and y versus Eddington ratio ($L_{\text{bol}}/L_{\text{Edd}}$) for the sample listed in table 4.9, 4.10, and 4.13. The NLS1 data points and those of BLS1, distinguished by colors, distribute almost separately, the former at higher Eddington ratio and the latter at lower Eddington ratio. We find a trend that the electron temperature kT_e is lower for higher Eddington ratio, while the optical depth τ is larger for higher Eddington ratio. On the other hand, the Compton y parameter distributes in narrow range around unity with a faint trend that y is smaller for higher Eddington ratio. Since y is simply calculated from Γ , which is larger for the NLS1 sources on average, it may not be surprising.

We next show the plot of the electron temperature kT_e versus the luminosity ratio $L_{\text{X}}/L_{\text{UV}}$ in figure 4.27. Not as clear as for $L_{\text{bol}}/L_{\text{Edd}}$, but the NLS1 data points distribute at lower $L_{\text{X}}/L_{\text{UV}}$. This indicates that the power-law component with respect to the thermal disk component is weaker for NLS1 sources.

Some of the trend mentioned above are not necessarily highly significant at this point. We apparently need larger sample of NLS1 data. Nevertheless,

it is worth interpreting them with accretion models. On this point, repeated observations of the NGC 4151 with INTEGRAL provided interesting results; the hard X-ray spectrum of this source in its bright state is reproduced with $kT_e=50\text{--}70\text{ keV}$ and $\tau=1.3\text{--}2.6$, while that in its dim state is with $kT_e=180\text{--}230\text{ keV}$ and $\tau=0.3\text{--}0.7$ (Lubiński et al., 2010). NGC 4151 is a typical BLS1, but may show similar trend in one source at different accretion rate.

Comparison with Disk-Corona Models

We attempt to interpret some of the trends inferred above in the frame work of the disk corona model, which is a standard model for radio quiet AGNs. We here assume that the Eddington ratio represents mass accretion rate (normalized to the mass of SMBH), and that is larger for NLS1 than for BLS1.

Lower electron temperature for higher accretion rate is naively interpreted as the consequence of a higher cooling rate, i.e., shorter cooling time. The cooling time of a electron via thermal Comptonization is expressed as $t_C = (3m_e c)/(8\sigma_T u_{\text{ph}})$, where m_e , σ_T , and u_{ph} are the electron mass, the Thomson cross section, and the photon energy density, respectively. Assuming the photon energy density from the accretion disk gets larger for increasing accretion rate, the cooling time gets shorter, resulting in lower temperature. On the other hand, the optical depth is naively proportional to the accretion rate if the geometry of the accretion corona is fixed regardless of accretion rate. Since the the Compton y parameter is approximately proportional to the product of kT_e and τ , that will be constant. This can be the most naive explanation for the trends we obtained.

The above explanation is, however, too much simplified. In fact, theoretical studies claims various feedback mechanism between disk and corona is essential (e.g. Haardt & Maraschi (1991); Stern et al. (1995); Yuan & Zdziarski (2004); Kawanaka et al. (2008); Liu et al. (2012)). Theoretical prediction of the UV to hard X-ray spectra have been presented in number of papers including above, though not necessarily overlap with out NLS1 results. Veledina et al. (2011) present their predication for 2–10 keV power-law index versus the Eddington ratio, in which the power-law index is steeper for higher Eddington ratio, which is consistent with our trend.

The accretion corona is sometime naively illustrated as a large sphere of electrons surrounding a central BH and inner part of geometrically thin accretion disk. However, this is not likely. For example, if we assume a sphere

of electrons that uniformly covers a SMBH of $10^8 M_\odot$ and its accretion disk radiating at the Eddington limit the cooling time is as short as ~ 3.4 s. This is much shorter than light crossing time (light crossing time is $\sim 5.8 \times 10^3$ s, assuming that the SMBH is the Schwarzschild BH). To make rapid X-ray variability, the accretion corona should be more localized. In fact, from variability analysis of Cyg X-1 data, Miyamoto et al. (1988) showed that such simple model fails to explain the time lags they observed.

Comparison with Clumpy Accretion Flow Model

We next compare our results with alternative model to account for UV to X-ray emission. That is an inhomogeneous accretion flow formed proposed by (Ishibashi & Courvoisier, 2009). In this model, a cascade of shocks is expected, where optically thick shocks give rise to optical/UV emission, while optically thin shocks, which are created by expanding clouds overlap at the region close to the central BH, give rise to X-ray emission.

They provided several analytic equations that give observable quantities, such as kT_e and L_X/L_{UV} . They studied several cases or regions, but we adopt the Case B in the Class S in their notation. According to their paper, Class S (large filling factors of the clouds) is appropriate for SMBH with mass lower than $10^8 M_\odot$. Case B is valid where the Compton cooling time scale is shorter than the dynamical (or free fall) time scale.

For the Compton cooling timescale (t_C), we calculate this parameter by using the Eddington ratio and the central BH mass. According to Ishibashi & Courvoisier (2012), the Compton cooling timescale is written as

$$t_C = \frac{6\pi G^2 m_e \zeta^2 M_{\text{BH}}^2}{\sigma_T c^4 \eta \dot{M}}, \quad (4.3)$$

where m_e , η and ζ are the electron mass, the canonical radiative efficiency and the radial distance in unit of the Schwarzschild radius ($R = \zeta R_S = \zeta \frac{2GM_{\text{BH}}}{c^2}$), respectively (Ishibashi & Courvoisier, 2012). M_{BH} and \dot{M} are the central BH mass and the mass accretion rate, respectively. Converting equation (4.3) by using the Eddington ratio ($\lambda_{\text{Edd}} = L_{\text{bol}}/L_{\text{Edd}}$) and the central BH mass, we obtain the following formula:

$$t_C = \frac{3G}{2c^3} \left(\frac{m_p}{m_e} \right)^{-1} \zeta^2 \lambda_{\text{Edd}}^{-1} M_{\text{BH}} [\text{s}], \quad (4.4)$$

where m_p is the proton mass. We see that the characteristic Compton cooling timescale is mainly determined by the central BH mass and the Eddington ratio. When we assume $\zeta = 5$ and calculated the Compton cooling time scale from equation (4.4) for the sources in table 4.13, the Compton cooling timescales are shorter than the free-fall time except for NGC 6814. This is the reason why we adopt the Case B.

According to Ishibashi & Courvoisier (2009), the electron temperature is written as

$$\frac{kT_e}{m_e c^2} \simeq 0.6 f^{2/7} \left(\frac{\eta_{\text{rad}}}{1/3} \right)^{-2/7} \zeta_{UV}^{3/7} \left(\frac{E_p}{1 \text{ MeV}} \right)^{4/7}, \quad (4.5)$$

where f and η_{rad} are the fraction of accreted matter contributing to the optically thin shock and the fraction that the kinetic energy of colliding clumps contributes to the radiation. ζ_{UV} is written as $\zeta_{UV} = \frac{\zeta}{100}$, respectively. E_p is the proton kinetic energy.

Ishibashi & Courvoisier (2009) also mentioned the relative importance of X-ray and UV contributions to the bolometric luminosity and quantified with the luminosity ratio L_X/L_{UV} . In Ishibashi & Courvoisier (2009), L_X/L_{UV} is written as

$$(B) \frac{\langle L_X \rangle}{\langle L_{UV} \rangle} \simeq 0.17 f^{9/7} \left(\frac{\eta_{\text{rad}}}{1/3} \right)^{-9/7} \zeta_{UV}^{10/7} \left(\frac{E_p}{1 \text{ MeV}} \right)^{4/7}. \quad (4.6)$$

For the luminosity ratio, we considered 2 cases separately. As we mentioned, Case B is valid when the Compton cooling timescale is shorter than the free-fall time t_{ff} ($t_{ff} = \sqrt{R^3/2GM_{\text{BH}}}$).

Using equation (4.6), equation (4.5) is represented in

$$(B) \frac{kT_e}{m_e c^2} \simeq 3.53 f^{-1} \left(\frac{\eta_{\text{rad}}}{1/3} \right) \zeta_{UV}^{-1} \frac{\langle L_X \rangle}{\langle L_{UV} \rangle}. \quad (4.7)$$

Equation (4.7) indicates that when we assume the parameters of f , η_{rad} , and ζ , the electron temperature is independent of the accretion rate.

In order to understand the difference of the electron temperature between NLS1s and BLS1s, we draw theoretical predictions over the plot shown in figure 4.27. As we mentioned earlier, we adopt the broadband X-ray luminosity and UV luminosity are in the range of 1–500 keV and 10^{-3} –0.1 keV, respectively. From equation (4.5) and (4.7), the electron temperature is predicted

to follow the relation in either form of

$$\frac{kT_e}{m_e c^2} \sim 0.89 \left(\frac{\zeta}{100} \right)^{1/9} \left(\frac{E_p}{1 \text{ MeV}} \right)^{4/9} \left(\frac{\langle L_X \rangle}{\langle L_{UV} \rangle} \right)^{2/9}, \quad (4.8)$$

$$\frac{kT_e}{m_e c^2} \sim \left(3 \frac{\eta_{\text{rad}}}{f} \right)^{1/10} \left(\frac{E_p}{1 \text{ MeV}} \right)^{2/5} \left(\frac{\langle L_X \rangle}{\langle L_{UV} \rangle} \right)^{3/10}. \quad (4.9)$$

The result is shown in figure 4.28. We first note the value of ζ and $\frac{\eta_{\text{rad}}}{f}$ are very small ($10^{-10} - 1$ and $10^{-12} - 10^{-4}$, respectively) to reproduce the data points. Since $\zeta \sim 100$ and $\frac{\eta_{\text{rad}}}{f} \sim 1$ are the typical values mentioned in Ishibashi & Courvoisier (2009), the model may be needed to reconsider. Nevertheless, leave these absolute values, considering simple analytic approach taken by them, this model may explain a broad trend of the distribution of the data points from the bottom left to the upper right. For example, the difference between BLS1 and NLS1 might be explained with that in $\frac{\eta_{\text{rad}}}{f} \sim 1$.

4.5 Summary in 3 NLS1s

We observed 3 NLS1s, Mrk 110, SWIFT J212745.6+565636, and IGR J16185–5928 with Suzaku and analyzed the 0.25–40 keV X-ray spectra. All of them are reproduced with three components, a power-law component, a reflection component, and a soft X-ray excess component modeled either with a single blackbody or the second cutoff power-law model. We were able to constrain the cutoff energies of Mrk 110 and SWIFT J212745.6+565636 within 100 keV, corresponding to the electron temperatures of 10–30 keV. For IGR J16185–5928, we were only able to constrain the lower limit of 240 keV, which corresponds to the electron temperature of 60 keV. Calculating the weighted mean electron temperatures of NLS1 and BLS1 using the results we obtained in this study and the previous results, we found that the mean electron temperature of NLS1 ($\langle kT_e \rangle = 11 \pm 2 \text{ keV}$) is significantly lower than that of BLS1 ($\langle kT_e \rangle = 22 \pm 3 \text{ keV}$). It is indicated that this trend reflects the fact that since NLS1 has higher accretion rate, the photon energy density of low energy photons from the accretion disk becomes higher than that of BLS1, leading to the Compton cooling becoming more efficiently.

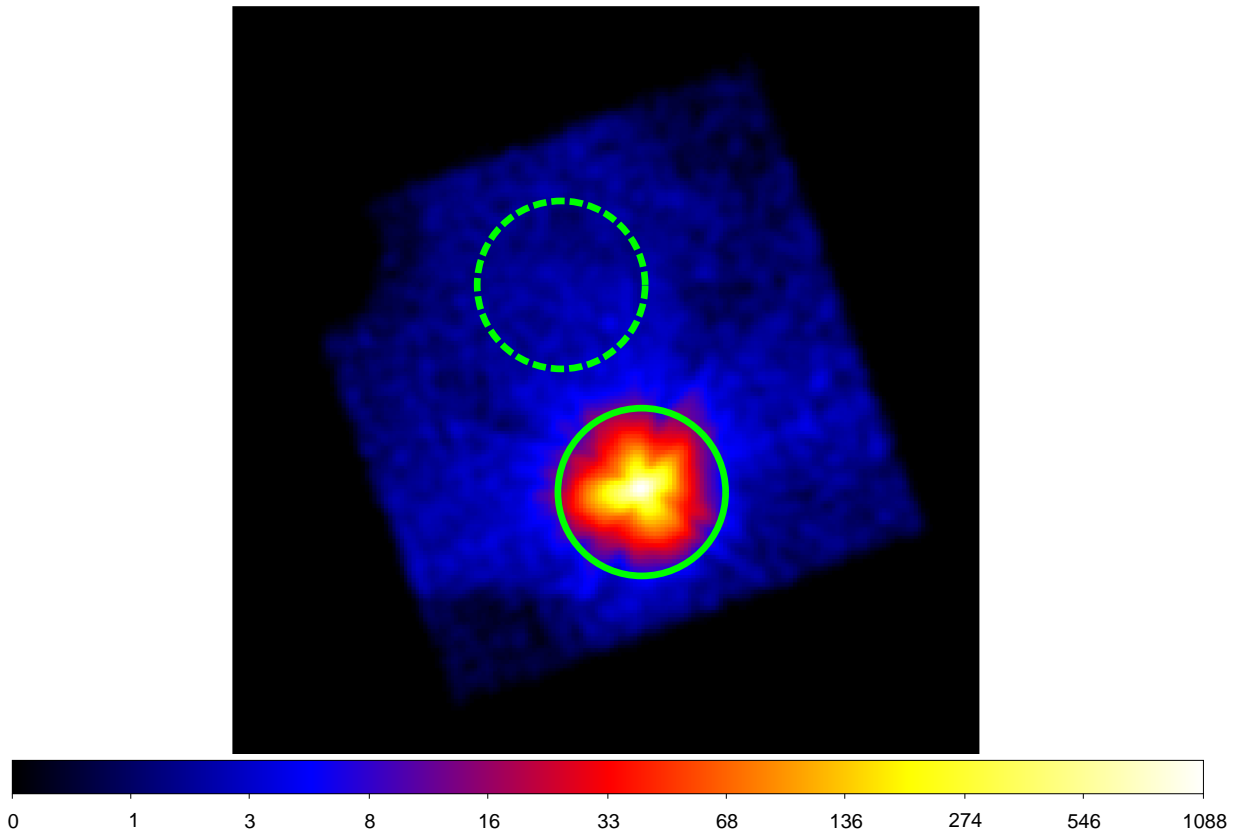


Figure 4.1: The raw image of XIS0+1+3 in the 2.5–8 keV band of Mrk 110. Solid and dashed circles, both of radius $3'$ indicate the source region and the background region, respectively.

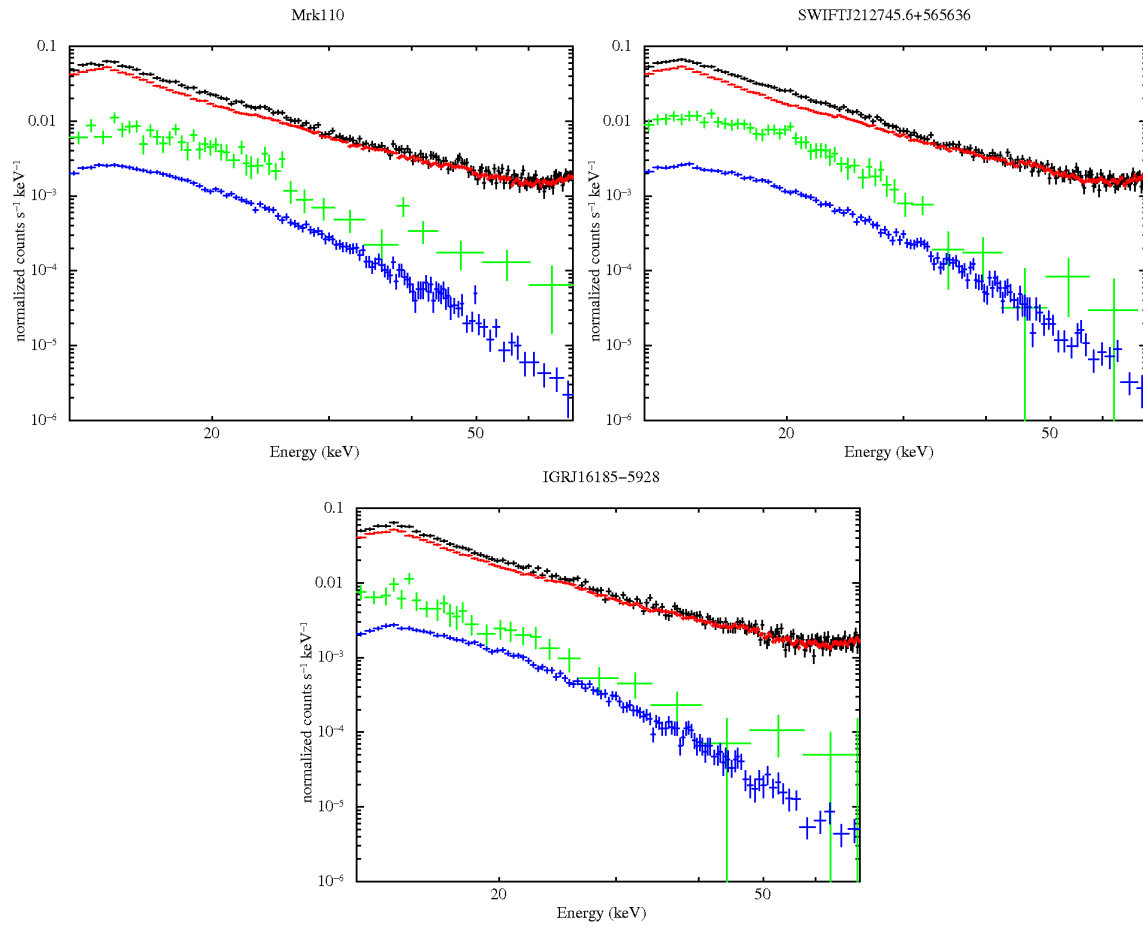


Figure 4.2: The HXD-PIN spectrum for the Suzaku observation of each target. The total spectra are represented in black points. The red points show the NXB spectra. The CXB spectra are shown in blue. The spectra of the targets are shown in green.

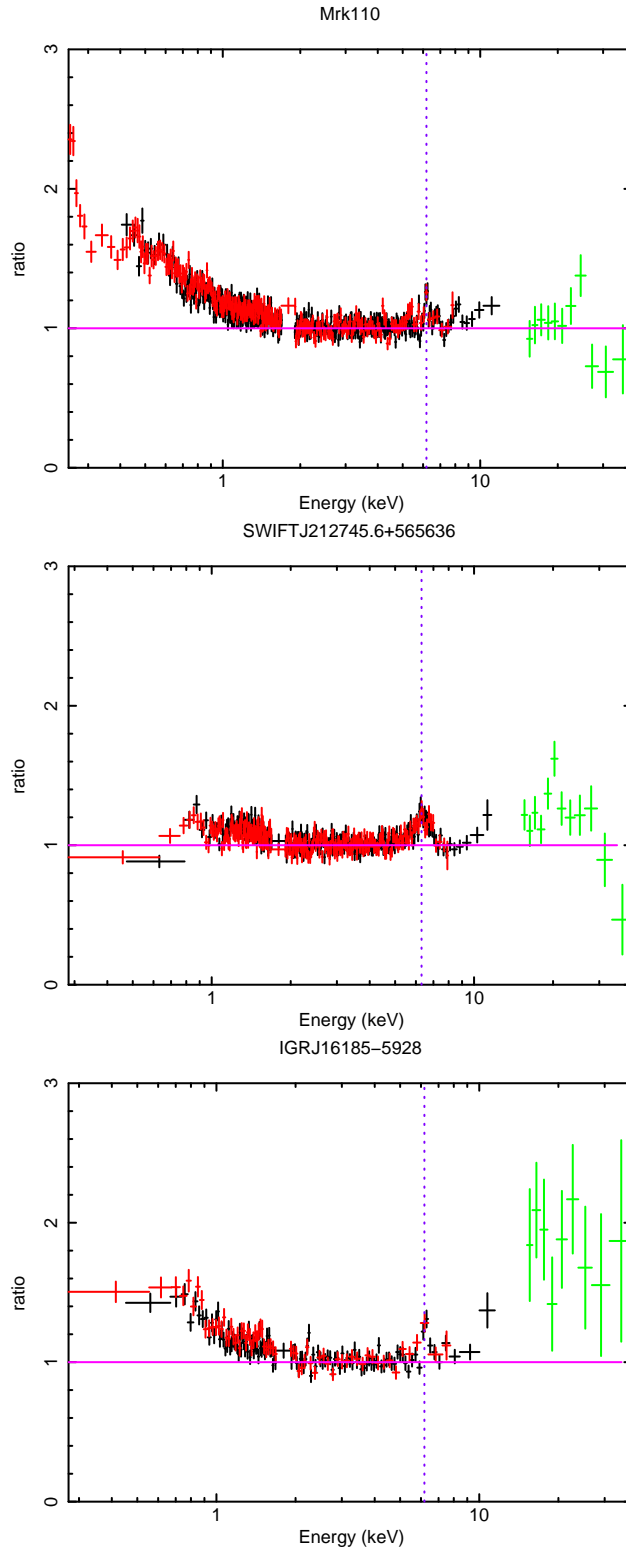


Figure 4.3: Data/model ratios for the three spectra of Mrk 110, SWIFTJ212745.6+565636, and IGR J16185-5928, fitted with a single power-law over the 2.5–4.5 keV and 7.5–12 keV energy ranges.

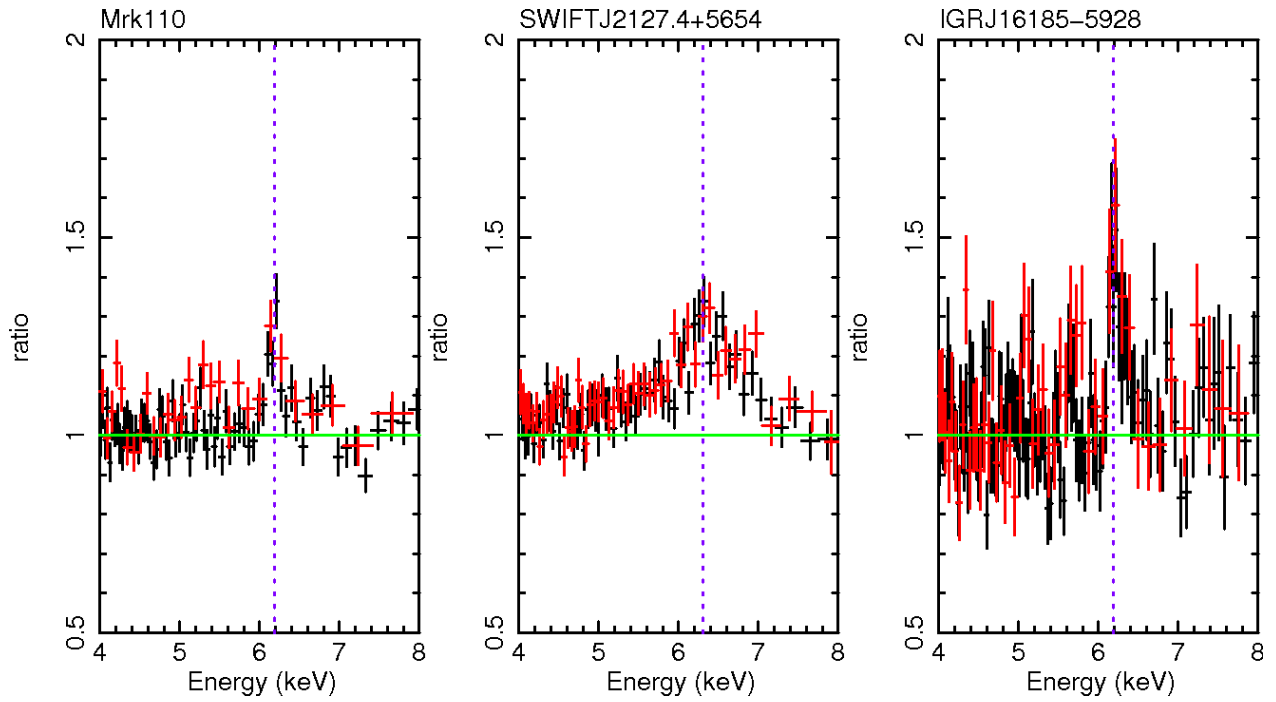


Figure 4.4: The spectral ratio to the single power-law model modified with the Galactic absorption in the 2.5–4.5 keV and 7.5–12 keV energy band. XIS-FI data, XIS-BI data are represented in black, red, respectively. The purple dotted line is the the rest-frame energy of 6.4 keV, which is expected for fluorescence from neutral iron.

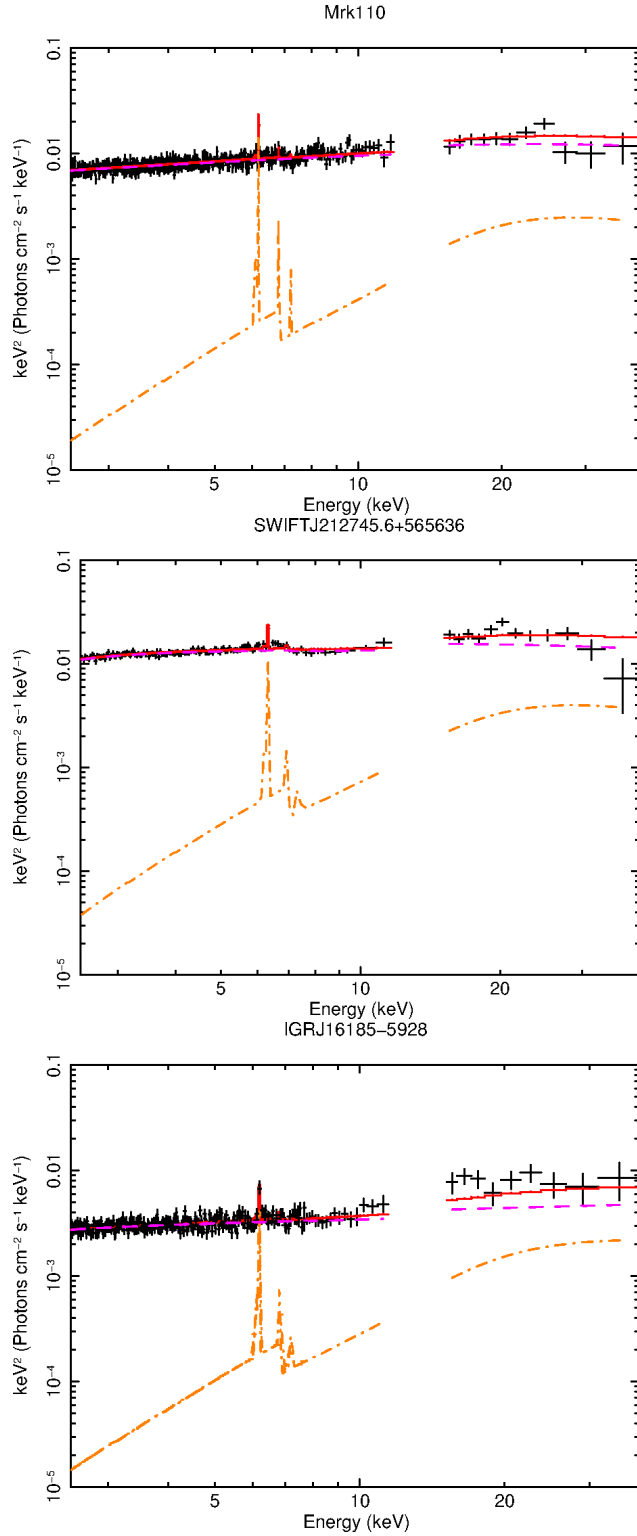


Figure 4.5: The X-ray spectra and the best-fit model with `pexmon` model in the 2.5–40 keV energy band. The unfolded spectra in the form of $E^2 I(E)$ are displayed. The total model is red solid line, the primary component is represented in magenta dashed line, and the orange dot-dashed line shows the reflection component. The best-fit parameters are listed in table 4.4.

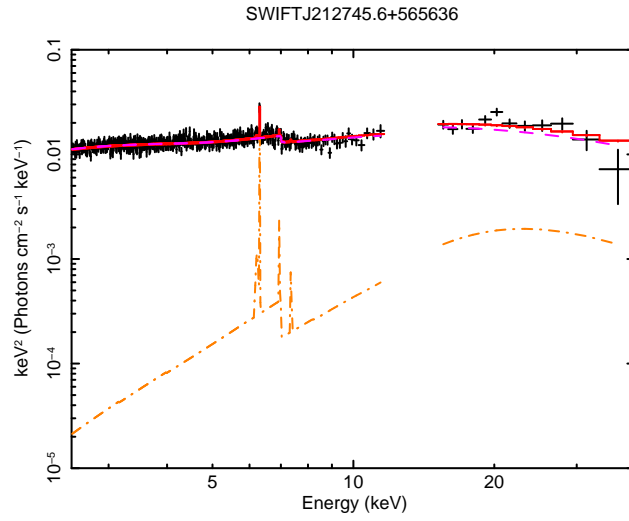


Figure 4.6: The X-ray spectra and the best-fit model with `pexmon` model in the 2.5–40 keV energy band of SWIFT J212745.6+565636. The same colors are used as in figure 4.5. The best-fit parameters are listed in table 4.4.

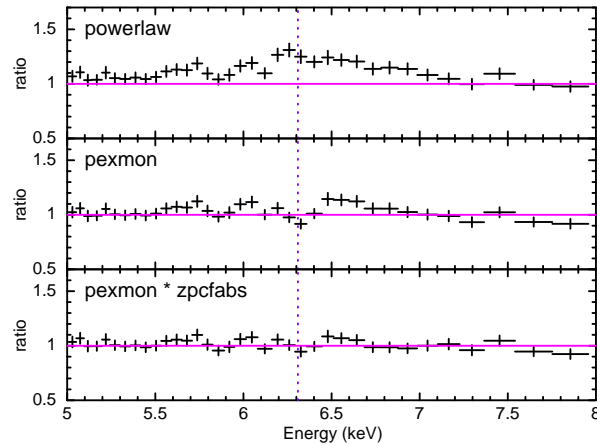


Figure 4.7: Data/model ratio residuals of the spectrum of SWIFT J212745.6+565636, in the Fe K-shell band.

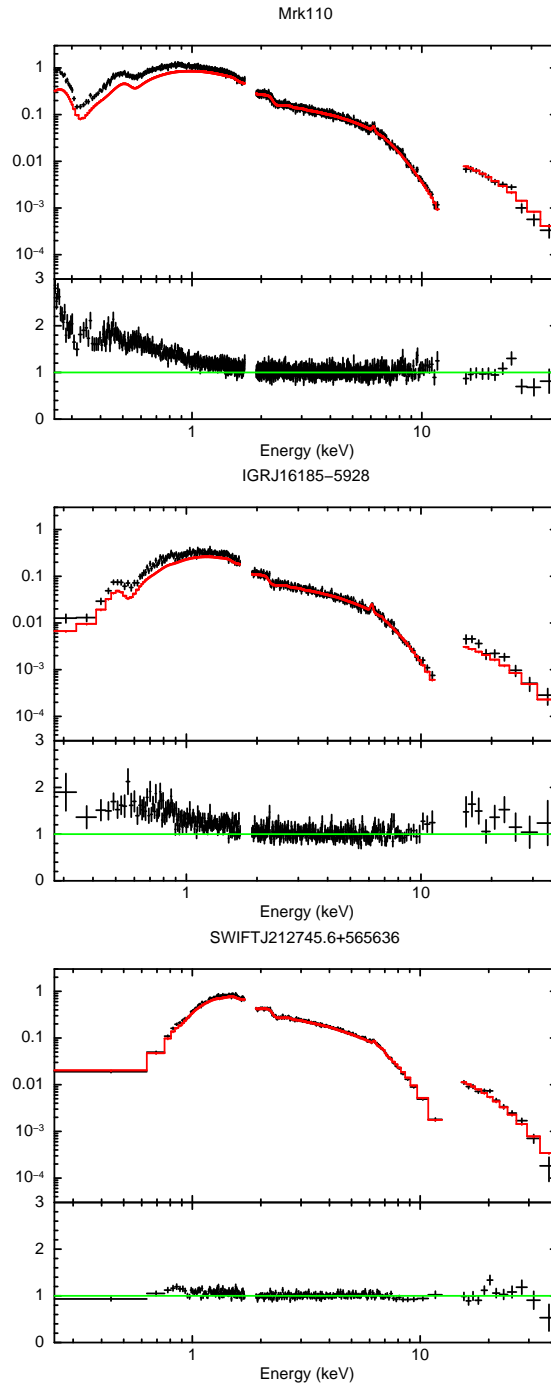


Figure 4.8: (Top) The 0.25–40 keV X-ray spectra and the best-fit model fitted in the 2.5–40 keV energy band with a `pexmon` model. The total model is the red solid line. (Bottom) The data/model ratio.

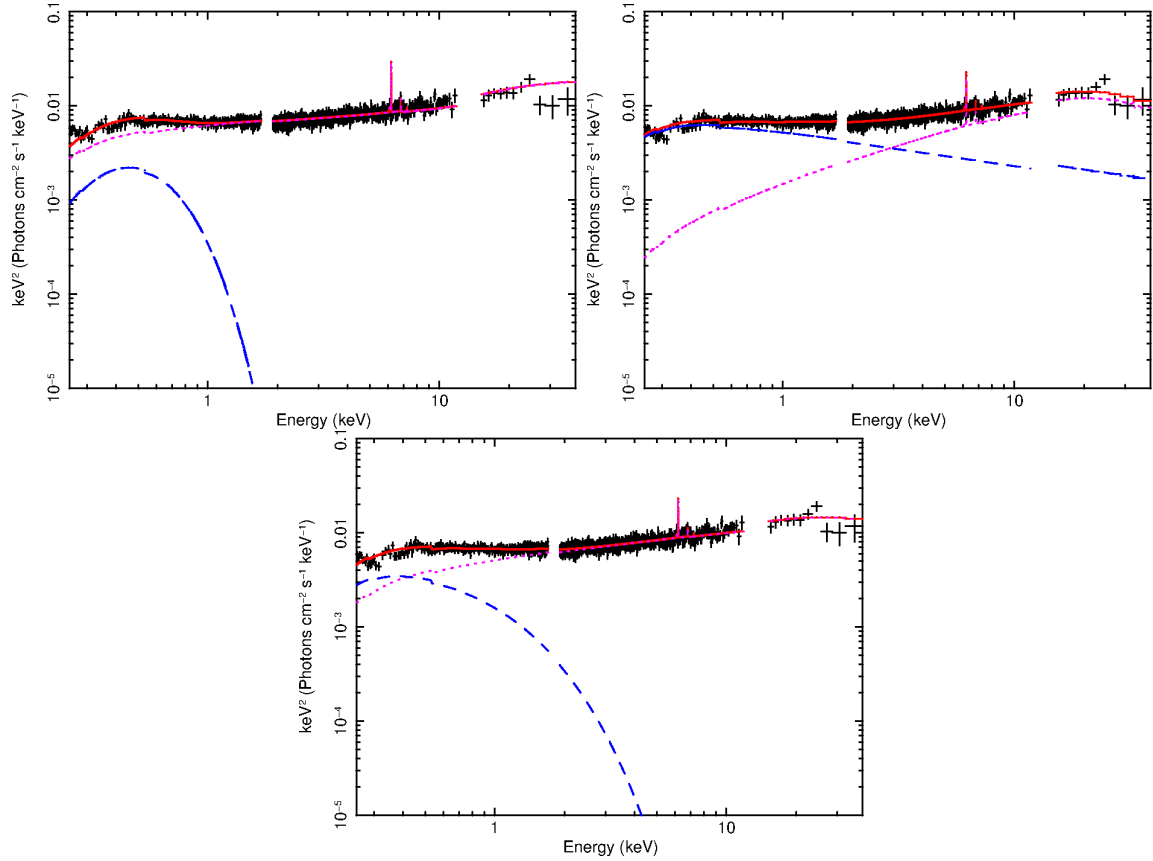


Figure 4.9: The 0.25–40 keV X-ray spectrum and the best-fit model using `pexmon` of Mrk 110. The unfolded spectra in the form of $E^2 I(E)$ are displayed. The total model is red solid line, the continuum component which is the sum of the power-law and its reflection is represented in magenta dotted line. The soft X-ray excess component is modeled with a blackbody, or a power-law, or a cut-off power-law shown in blue dashed lines. The best-fit parameters are listed in table 4.5.

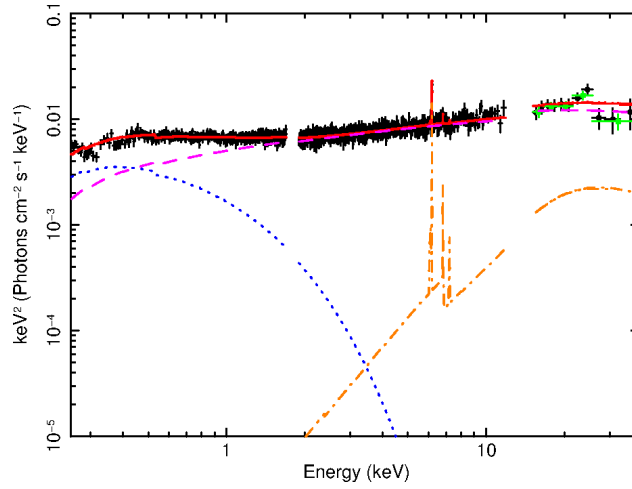


Figure 4.10: The 0.25–40 keV Mrk 110 X-ray spectrum and the best-fit model. Filled circles in black are the HXD-PIN spectrum from which the CXB, and the nominal NXB subtracted. Green squares are the HXD-PIN spectra for which NXB model with alternate normalization by +1% of the NXB.

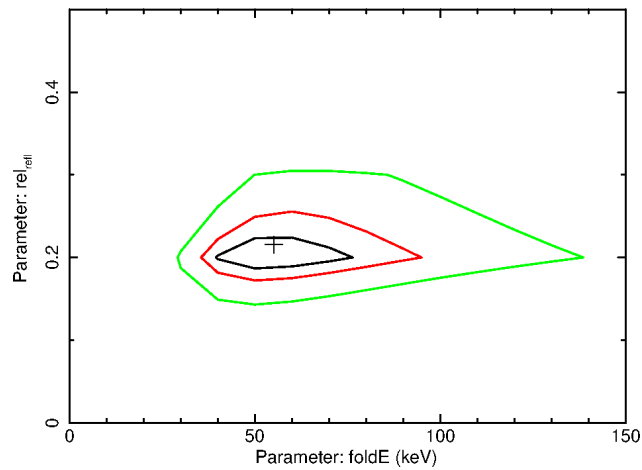


Figure 4.11: The contour plot for the reflection fraction R versus the cutoff energy E_C . The black, red, and green contours are 68%, 90%, and 99% confidence level, respectively.

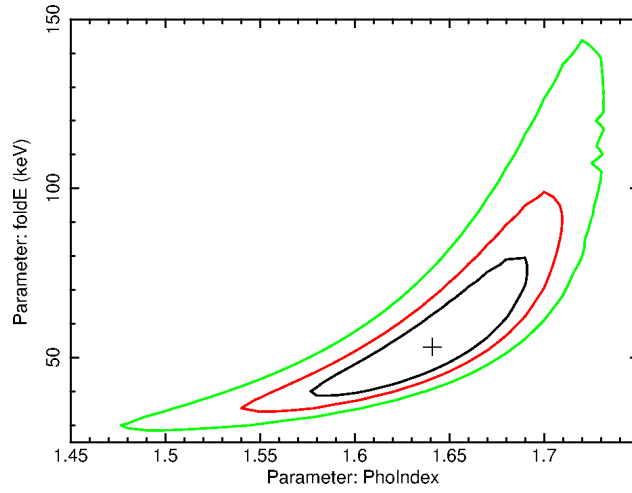


Figure 4.12: The contour plot for the cutoff energy E_C versus the photon index Γ . The same confidence levels as figure 4.11 are used.

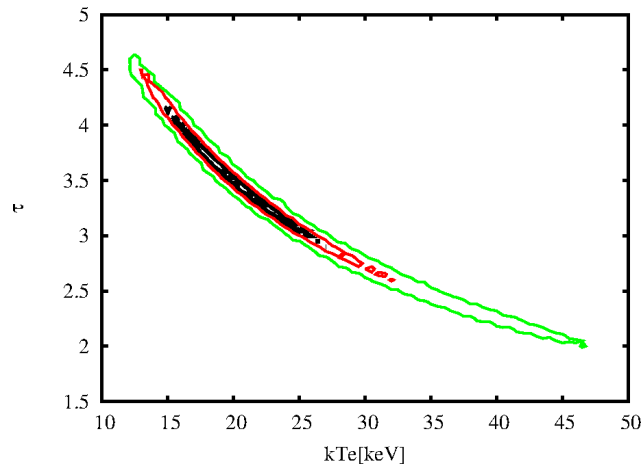


Figure 4.13: The contour plot for the optical depth τ versus the electron temperature kT_e . The same confidence levels as figure 4.11 are used.

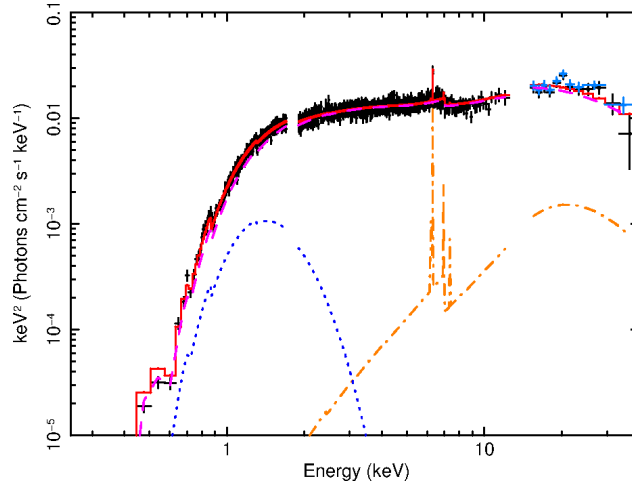


Figure 4.14: The 0.25–40 keV SWIFT J2127.4+5654 X-ray spectrum and the best-fit model. Filled circles in black are the HXD-PIN spectrum from which the CXB, and the nominal NXB subtracted. Light blue triangles are the HXD-PIN spectra for which NXB model with alternate normalization by -2% of the NXB.

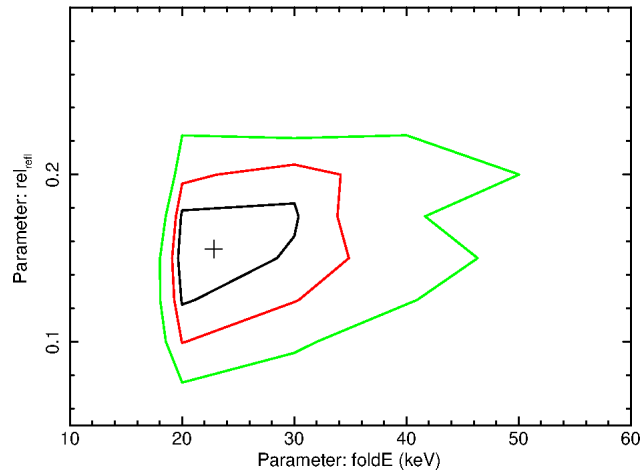


Figure 4.15: The contour plot for the reflection fraction R versus the cutoff energy E_C . The black, red, and green contours are 68%, 90%, and 99% confidence level, respectively.

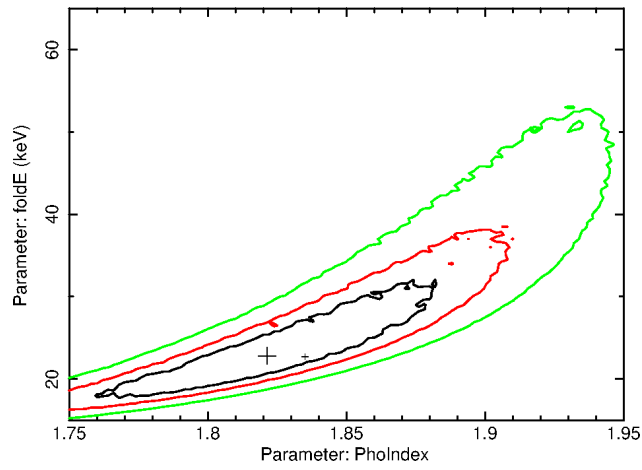


Figure 4.16: The contour plot for the cutoff energy E_C versus the photon index Γ . The same confidence levels as figure 4.11 are used.

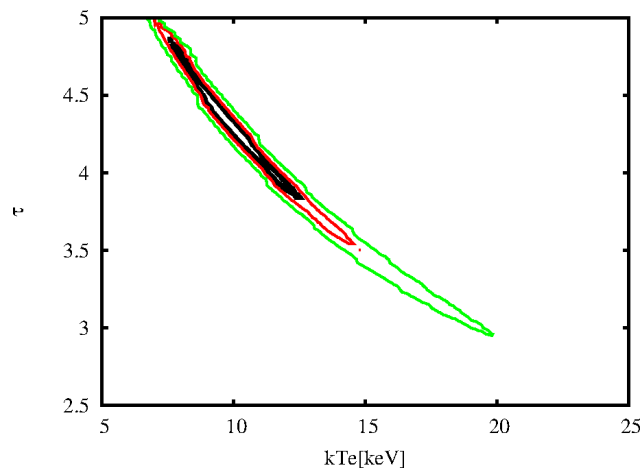


Figure 4.17: The contour plot for the optical depth τ versus the electron temperature kT_e . The same confidence levels as figure 4.11 are used.

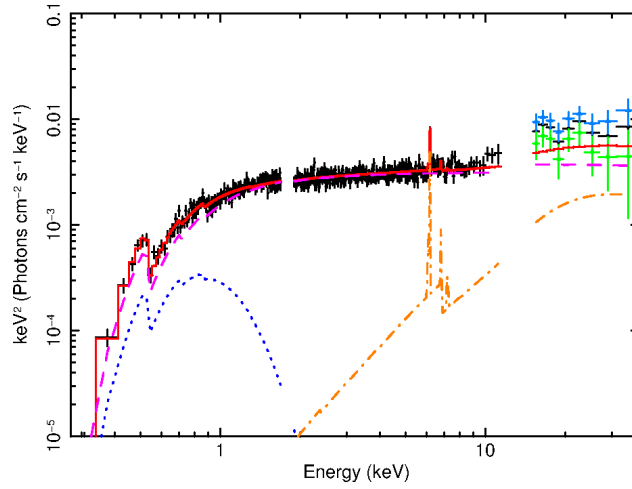


Figure 4.18: The 0.25–40 keV X-ray spectrum and the best-fit model. The blue triangles and green squares are HXD-PIN spectra for which NXB model with changing normalization by -3% and $+3\%$ of the NXB, respectively.

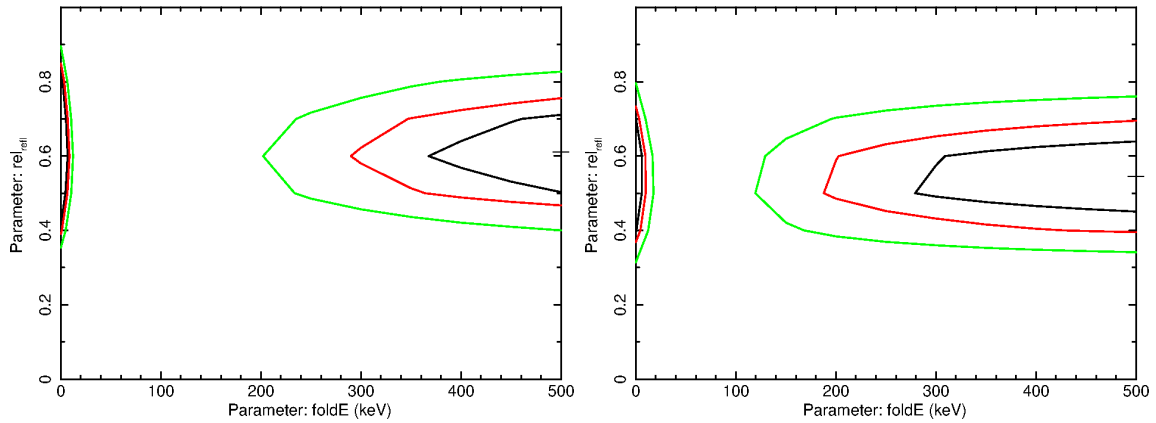


Figure 4.19: The contour plot for the reflection fraction R versus the cutoff energy E_C . The black, red, and green contours are 68%, 90%, and 99% confidence level, respectively.

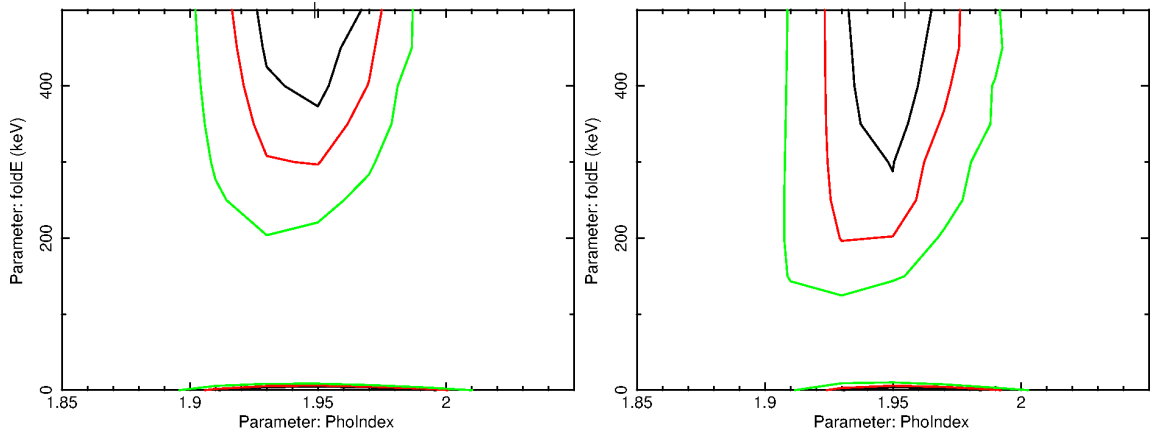


Figure 4.20: The contour plot for the cutoff energy E_C versus the photon index Γ . The same confidence levels as figure 4.11 are used.

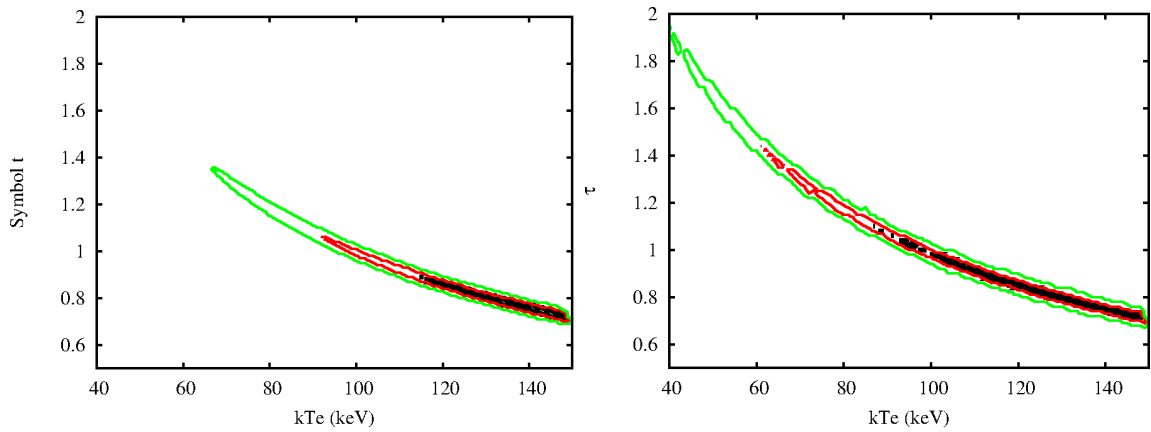


Figure 4.21: The contour plot for the optical depth τ versus the electron temperature kT_e . The same confidence levels as figure 4.11 are used.

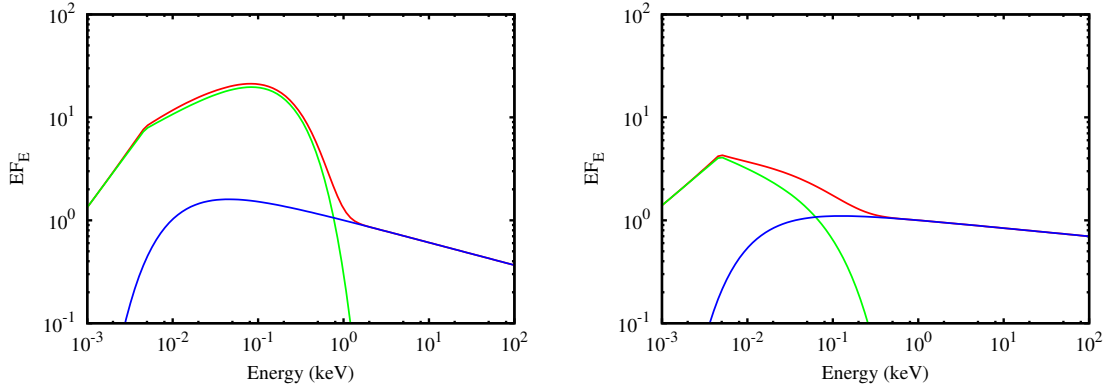


Figure 4.22: The typical SED of NLS1 (left) and BLS1 (right) (Jin et al., 2012). The red solid line shows the total model. The green solid line shows the SE component model. The blue solid line shows the PL component model. EF_E is normalized by the normalization of PL component at 1 keV.

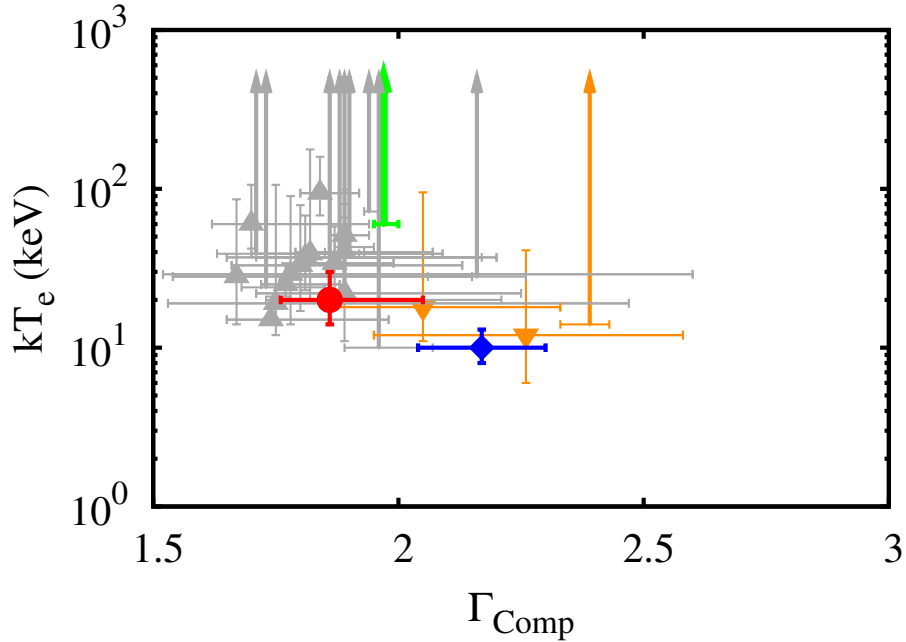


Figure 4.23: The electron temperature kT_e versus the photon index Γ_{Comp} of the Seyfert 1 galaxies. The red filled circle and the blue filled diamond represent Mrk 110 and SWIFT J212745.6+565636, respectively. The green arrow shows the lower limit of IGR J16185–5928. The dark-orange down-triangles are the data of other 2 NLS1s referred from Malizia et al. (2008). The dark-orange upward arrow is the lower limit of IGR J19387–0671 (Malizia et al., 2008). The gray up-triangles, upward-arrows are the data of Molina et al. (2009), lower limit, respectively.

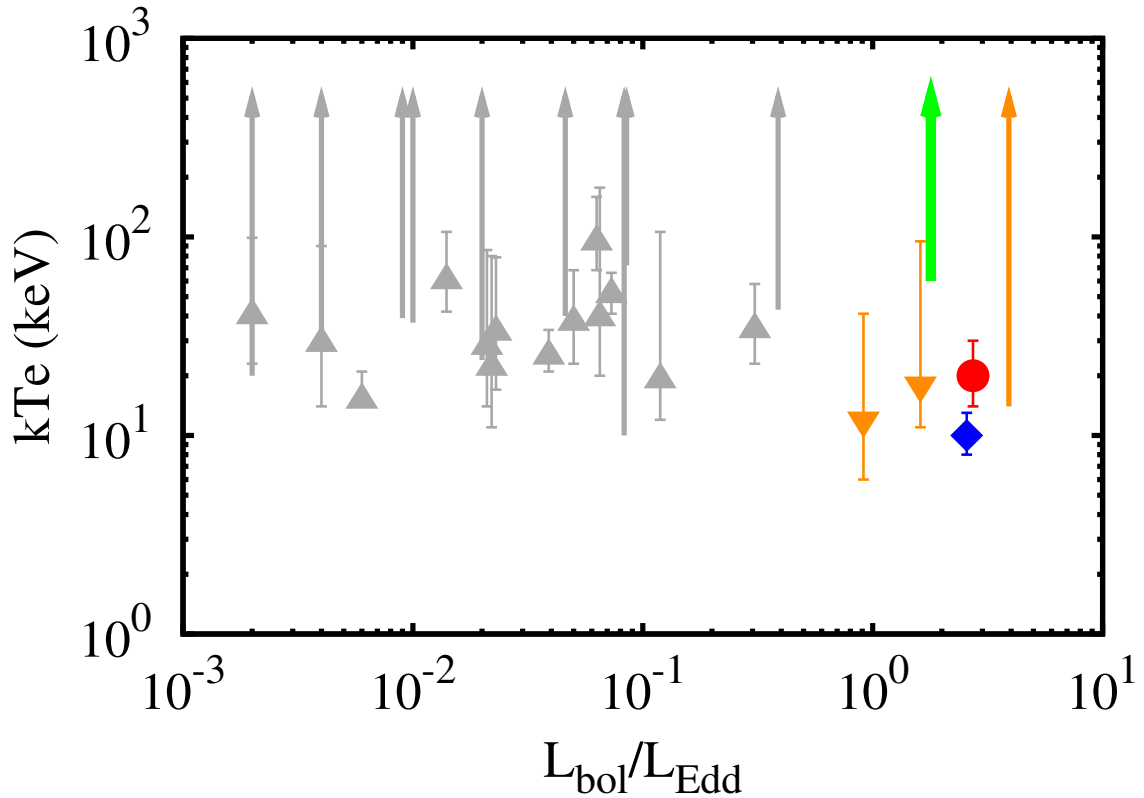


Figure 4.24: The electron temperature kT_e versus the Eddington ratio $L_{\text{bol}}/L_{\text{Edd}}$ of Seyfert 1 galaxies. The red circle and the blue square represent Mrk 110 and SWIFT J212745.6+565636, respectively. The green upward-arrow shows the lower limit of IGR J16185-5928. The orange down-triangles are the data of other 2 NLS1s referred from Malizia et al. (2008). The orange arrow shows the lower limit of IGR J19378-0617 referred from Malizia et al. (2008). The gray up-triangles and upward-arrows are the data of Molina et al. (2009) and the lower limit, respectively.

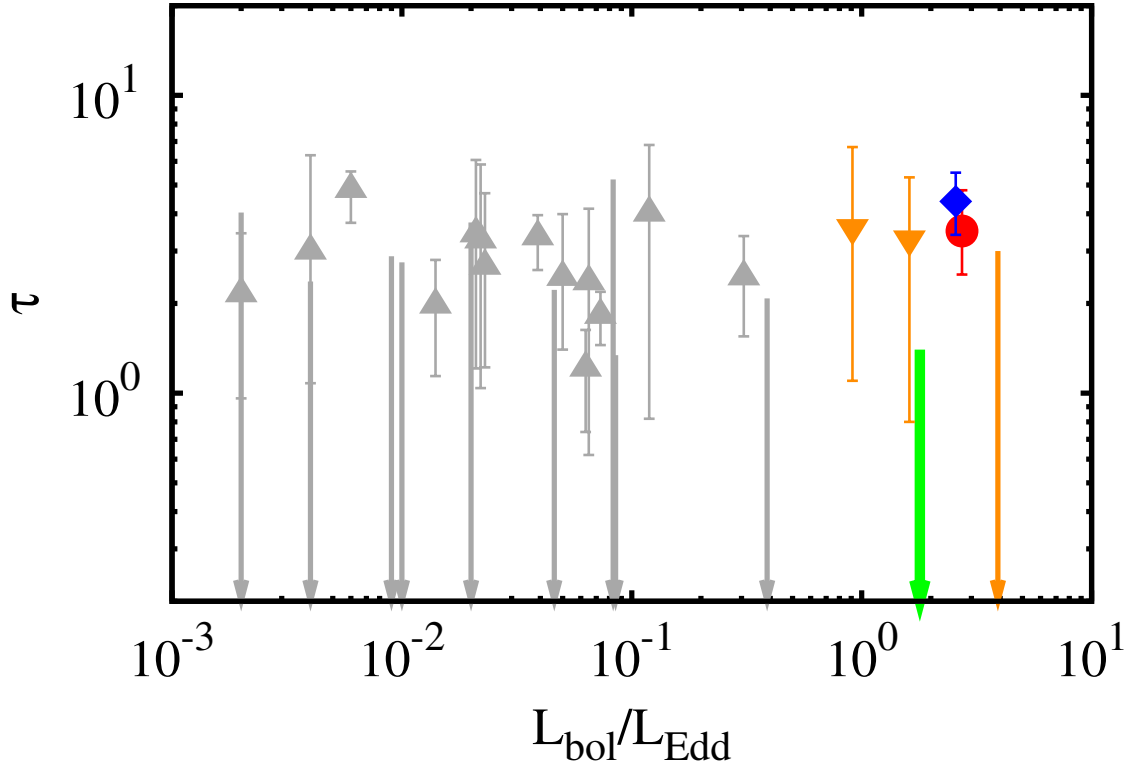


Figure 4.25: The optical depth τ versus the Eddington ratio $L_{\text{bol}}/L_{\text{Edd}}$ of Seyfert 1 galaxies. The red circle, the blue square represent Mrk 110 and SWIFT J212745.6+565636, respectively. The orange down-triangles are the data of other 2 NLS1s referred from Malizia et al. (2008). The orange downward-arrow shows the upper limit of IGR J19378–0671 (Malizia et al., 2008). The gray up-triangles and downward-arrows are the data of Molina et al. (2009) and the upper limit, respectively.

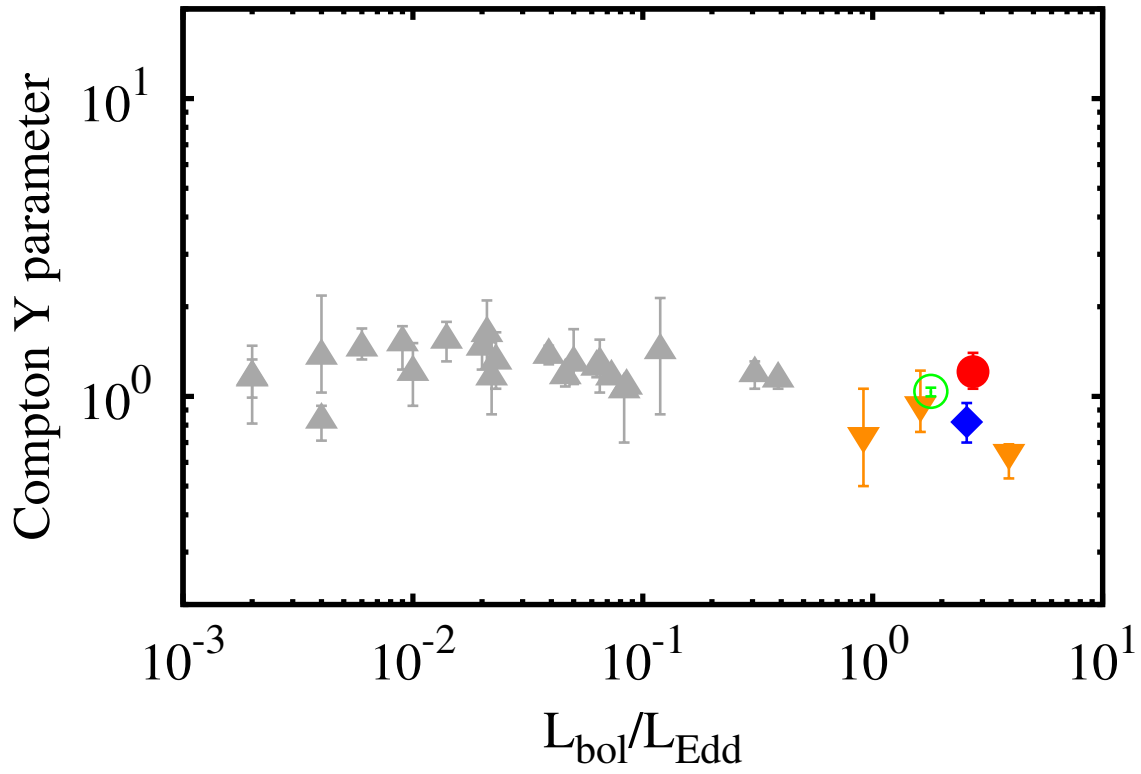


Figure 4.26: The Compton y parameter versus the Eddington ratio $L_{\text{bol}}/L_{\text{Edd}}$ of Seyfert 1 galaxies. The red circle, the blue square, and the green opened circle represent Mrk 110, SWIFT J212745.6+565636, and IGR J16185–5928, respectively. The orange down-triangles are the data of other NLS1s referred from Malizia et al. (2008). The gray up-triangles are the data of Molina et al. (2009)

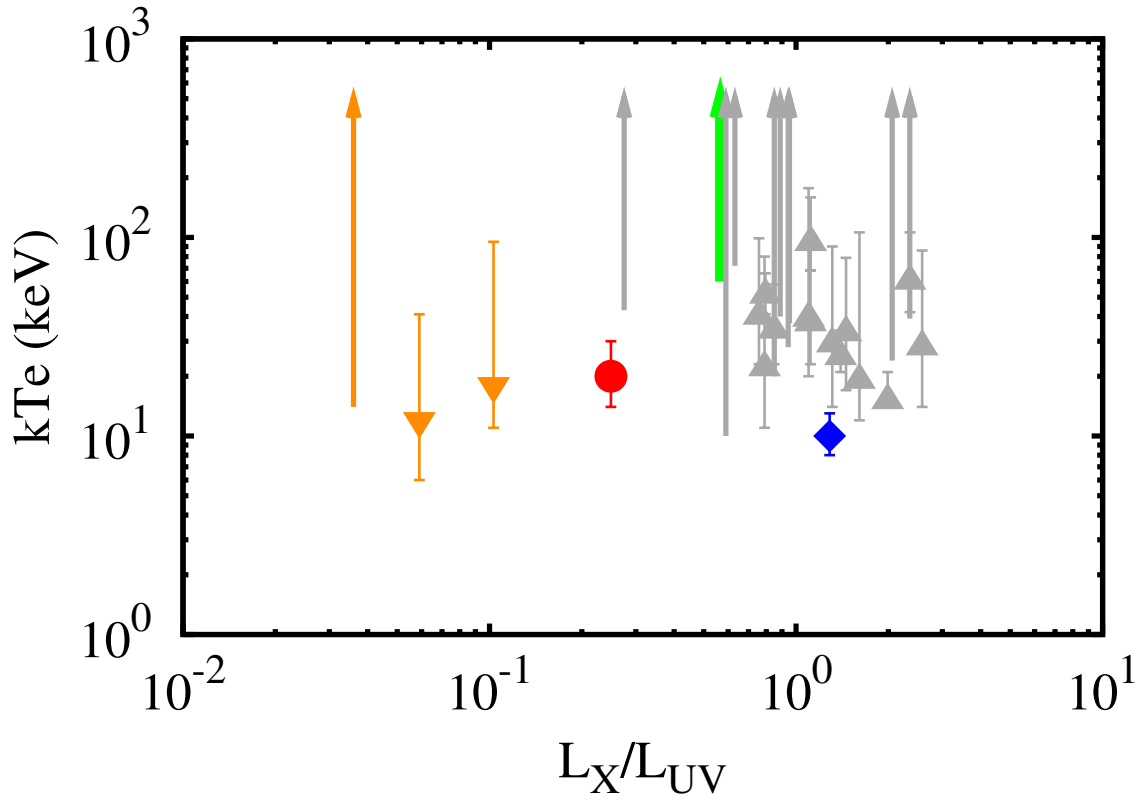


Figure 4.27: The electron temperature kT_e versus the luminosity ratio of L_X/L_{UV} . The red circle and the blue square represent Mrk 110 and SWIFT J212745.6+565636, respectively. The green arrow shows the lower limit of IGR J16185–5928. The orange down-triangles are the data of other 2 NLS1s referred from Malizia et al. (2008). The gray up-triangles, upward-arrows are the data of Molina et al. (2009), lower limit, respectively.

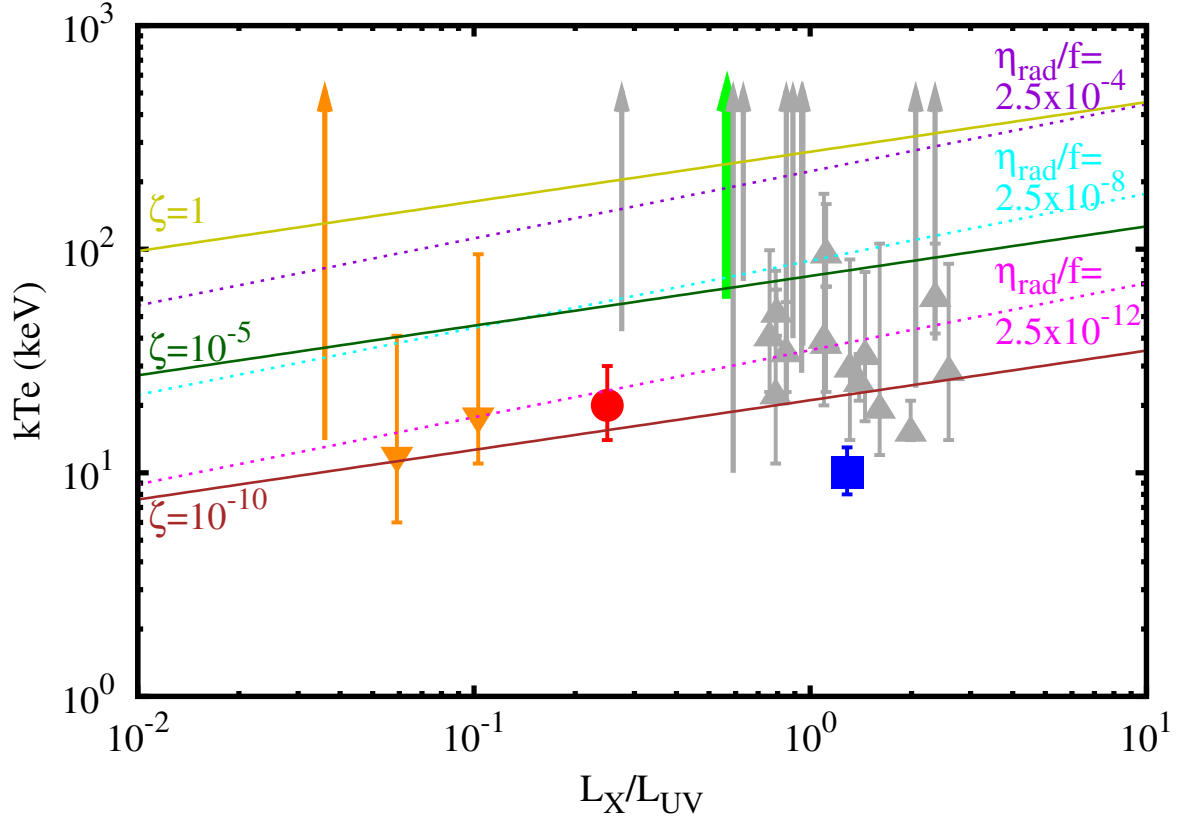


Figure 4.28: The electron temperature kT_e versus luminosity ratio of L_X/L_{UV} . The red circle and the blue square represent Mrk 110 and SWIFT J212745.6+565636, respectively. The green arrow shows the lower limit of IGR J16185–5928. The orange down-triangles are the data of other 2 NLS1s referred from Malizia et al. (2008). The gray up-triangles and upward-arrows are the data of Molina et al. (2009), lower limit, respectively. Solid lines (dark-yellow, dark-dark, and brown) are the expected electron temperatures calculated from equation (4.8) with ζ changing 1, 10^{-5} , and 10^{-10} , respectively. Dotted lines (dark-violet, cyan, and magenta) are the expected electron temperatures calculated from equation (4.9) with $\frac{\eta_{\text{rad}}}{f}$ changing 2.5×10^{-4} , 2.5×10^{-8} , and 2.5×10^{-12} , respectively.

Table 4.1: The Suzaku NLS1 sample

Object	RA(J2000) [h m s]	Dec(J2000) [d m s]	Redshift	$N_{H,Gal}$ [10^{22} cm^{-2}]	Date
Mrk 110	09 25 12.9	+52 17 11	0.0353	0.0147	2007/11/02
SWIFT J212745.6+565636	21 27 44.9	+56 56 40	0.0144	0.786	2007/12/03
IGR J16185–5928	16 18 36.4	–59 27 17	0.0350	0.247	2008/02/09

Table 4.2: The HXD-PIN count rates in the 15–40 keV band during the Earth occultation periods, compared with the NXB model.

Target	Mrk 110	SWIFTJ212745.6+565636
Earth event	0.318 ± 0.004	0.300 ± 0.004
NXB	0.316 ± 0.001	0.306 ± 0.001
ratio	0.01 ± 0.01	-0.02 ± 0.01

Table 4.3: 2.5–12 keV spectral fit

Parameter	Mrk 110	SWIFT J212745.6+565636	IGRJ16185–5928
single power-law model			
Γ	1.72 ± 0.02	2.01 ± 0.02	1.83 ± 0.05
χ^2/dof	879.88/731	1237.5/835	388.36/311
power-law + gaussian model			
Γ	1.74 ± 0.02	2.01 ± 0.02	1.84 ± 0.03
LineE[keV]	$6.39^{+0.02}_{-0.01}$	6.36 ± 0.08	6.43 ± 0.03
σ [keV]	< 0.08	$0.49^{+0.11}_{-0.09}$	< 0.09
EW[eV]	51^{+26}_{-25}	229^{+92}_{-91}	86 ± 52
χ^2/dof	730.16/728	776.54/832	310.65/308

Table 4.4: 2.5–40 keV spectral fit. The inside () is the 1 parameter error taking into the 1 σ systematic uncertainty of the HXD-PIN.

Parameter	Mrk 110	SWIFT J212745.6+565636	IGRJ16185–5928
pexrav+zgauss			
Γ	1.71 ± 0.04	$2.13^{+0.07}_{-0.06}$	1.98 ± 0.07
E_C [keV]	$44^{+58(+245)}_{-13(-18)}$	$29^{+5(+23)}_{-4(-7)}$	$> 110(> 45)$
R	$0.7^{+0.6}_{-0.5}$	$3.7^{+0.9}_{-0.8}$	$1.5^{+0.7}_{-0.8}$
LineE[keV]	6.4(fix)	6.38 ± 0.07	6.4(fix)
σ [keV]	0.01(fix)	$0.18^{+0.17}_{-0.09}$	0.01(fix)
EW [eV]	43^{+21}_{-18}	< 103	65^{+34}_{-37}
χ^2/dof	752.42/747	728.84/838	290.95/314
pexmon			
Γ	$1.71^{+0.03}_{-0.04}$	1.97 ± 0.03	$1.87^{+0.03}_{-0.04}$
E_C [keV]	88^{+60}_{-31}	200^{+1019}_{-95}	> 239
R	0.23 ± 0.05	0.30 ± 0.06	$0.43^{+0.10}_{-0.09}$
χ^2/dof	721.37/748	809.22/841	307.17/315
pexmon \times zpcfabs			
Γ	$2.0^{+0.2}_{-0.1}$
E_C [keV]	43^{+274}_{-19}
R	$0.17^{+0.07}_{-0.06}$
N_H [10^{22}cm^{-2}]	84^{+36}_{-40}
f	0.4 ± 0.1
χ^2/dof	755.06/839

Table 4.5: 0.25–40 keV spectral fit of Mrk 110 using pexmon+soft X-ray excess model (zbbbody, powerlaw, cutoffpl).

Model	Parameter	soft X-ray excess model		
		zbbbody	powerlaw	cutoffpl
pexmon	Γ	$1.852^{+0.004}_{-0.009}$	< 1.17	$1.68^{+0.04}_{-0.08}$
	E_C1 [keV]	> 1040	22^{+3}_{-2}	72^{+42}_{-28}
	R	$0.40^{+0.05}_{-0.06}$	0.19 ± 0.04	0.23 ± 0.05
zbbbody1	kT [eV]	111 ± 3
powerlaw	Γ	$2.36^{+0.03}_{-0.02}$
cutoffpl	Γ	2.0 ± 0.2
	E_C2 [keV]	0.7 ± 0.2
χ^2/dof		1993.33/1709	1813.29/1709	1792.54/1708

Table 4.6: The best-fit parameter of Mrk 110 0.25–40 keV spectral fit.

Parameter	HXD NXB nominal	HXD +1% NXB
Γ_{hard}	$1.66^{+0.05}_{-0.06}$	$1.65^{+0.05}_{-0.08}$
E_C [keV]	65^{+46}_{-21}	55^{+30}_{-18}
R	0.22 ± 0.05	$0.22^{+0.04}_{-0.05}$
Γ_{soft}	$2.1^{+0.1}_{-0.3}$	$2.0^{+0.2}_{-0.1}$
E_C [keV]	0.7 ± 0.2	$0.7^{+0.3}_{-0.1}$
χ^2/dof	1792.39/1708	1794.94/1708

Table 4.7: The best-fit parameter of SWIFT J2127.4+5654 0.25–40 keV spectral fit.

Parameter	HXD NXB nominal	HXD -2% NXB
Γ	$1.80^{+0.08}_{-0.06}$	1.82 ± 0.07
E_C [keV]	20^{+7}_{-4}	23^{+7}_{-5}
R	0.14 ± 0.04	$0.16^{+0.04}_{-0.05}$
kT [eV]	233^{+10}_{-12}	234 ± 11
$N_{\text{H}}[10^{22}\text{cm}^{-2}]$	135^{+22}_{-29}	142^{+26}_{-27}
f	$0.51^{+0.07}_{-0.06}$	$0.51^{+0.08}_{-0.09}$
χ^2/dof	1610.04/1561	1612.21/1561

Table 4.8: The best-fit parameter of IGR J16185–5928 0.25–40 keV spectral fit.

Parameter	HXD NXB nominal	HXD -3% NXB	HXD +3% NXB
Γ	1.96 ± 0.02	$1.82^{+0.06}_{-0.07}$	$1.95^{+0.03}_{-0.02}$
E_C [keV]	> 310	> 348	> 240
R	$0.5^{+0.2}_{-0.1}$	0.6 ± 0.1	$0.52^{+0.15}_{-0.09}$
kT [eV]	146^{+10}_{-9}	149^{+13}_{-11}	149^{+9}_{-13}
χ^2/dof	864.33/816	925.49/816	866.81/816

Table 4.9: The observational parameters such as the photon index Γ_{Comp} , the electron temperature kT_e , the optical depth and the 2–10 keV luminosity. Column (1) : Object name. Column (2) : Power-law photon index Γ_{Comp} . Column (3) : Electron energy kT_e [keV]. Column (4) : Optical depth τ . Column (5) : Compton y parameter. Column (6) : 2–10 keV luminosity

Object	Γ_{Comp}	kT_e [keV]	τ	y	$\log L_{2-10}$
Mrk 110	1.9 ± 0.1	20_{-7}^{+13}	3.5 ± 1.0	1.2 ± 0.1	43.99
SWIFT J212745.6+565636	2.2 ± 0.1	10_{-2}^{+5}	$4.4_{-0.9}^{+0.6}$	0.8 ± 0.1	43.74
IGR J16185–5928	$1.97_{-0.02}^{+0.03}$	> 60	< 1.04	$1.04_{-0.02}^{+0.03}$	43.81

Table 4.10: The observational parameters such as the photon index Γ_{Comp} , the electron temperature kT_e , the optical depth and the 2–10 keV luminosity. Column (1) : Object name. Column (2) : Power-law photon index Γ_{Comp} . Column (3) : Electron energy kT_e [keV]. Column (4) : Optical depth τ . Column (5) : Compton y parameter. Column (6) : 2–10 keV luminosity

Object	Γ_{Comp}	kT_e [keV]	τ	y	$\log L_{2-10}$
Malizia et al. (2008)					
IGR J14552–5133	$2.1^{+0.9}_{-0.1}$	17^{+83}_{-7}	3.3	$0.9^{+1.0}_{-0.1}$	42.66
IGR J16385–2057	$2.3^{+0.8}_{-0.2}$	11^{+30}_{-5}	3.7	$0.7^{+0.6}_{-0.1}$	42.95
IGR J19378–0671	$2.34^{+0.01}_{-0.02}$	> 20	< 2.4	$0.69^{+0.01}_{-0.02}$	43.22
Molina et al. (2009)					
2E 1853.7+1534	$1.75^{+0.82}_{-0.13}$	19^{+90}_{-6}	4.1	$1.42^{+1.87}_{-0.30}$	44.28
4U 0517+17	$1.88^{+0.02}_{-0.03}$	> 41	< 2.1	$1.17^{+0.04}_{-0.04}$	43.18
4U 1344–60	$1.86^{+0.14}_{-0.15}$	> 39	< 2.3	$1.20^{+0.25}_{-0.26}$	43.11
FRL 1146	$1.89^{+0.42}_{-0.11}$	21^{+60}_{-10}	3.3	$1.16^{+0.67}_{-0.18}$	43.43
GRS 1734–292	$1.74^{+0.09}_{-0.04}$	14^{+5}_{-1}	4.9	$1.45^{+0.22}_{-0.08}$	43.53
IC 4329A	$1.89^{+0.03}_{-0.02}$	48^{+14}_{-9}	1.9	$1.16^{+0.04}_{-0.04}$	43.84
IGR J07597–3842	$1.77^{+0.05}_{-0.03}$	24^{+9}_{-4}	3.4	$1.37^{+0.10}_{-0.06}$	43.76
IGR J12415–5750	$1.73^{+0.03}_{-0.04}$	> 28	< 3.2	$1.46^{+0.08}_{-0.10}$	43.11
IGR J16119–6036	$1.89^{+0.18}_{-0.16}$	> 25	< 3.0	$1.16^{+0.28}_{-0.26}$	42.30
IGR J16482–3036	$1.80^{+0.14}_{-0.11}$	32^{+46}_{-14}	2.7	$1.31^{+0.27}_{-0.21}$	43.36
IGR J16558–5203	$2.20^{+0.06}_{-0.06}$	< 511	> 0.2	$0.79^{+0.05}_{-0.05}$	44.04
IGR J17488–3253	$1.71^{+0.10}_{-0.07}$	> 40	< 2.6	$1.51^{+0.24}_{-0.18}$	43.04
IGR J18027–1455	$1.70^{+0.09}_{-0.07}$	58^{+43}_{-16}	2.0	$1.54^{+0.22}_{-0.18}$	43.26
LEDA 168563	$1.82^{+0.28}_{-0.08}$	37^{+145}_{-17}	2.4	$1.28^{+0.54}_{-0.15}$	43.91
MCG +08–11–011	$1.88^{+0.02}_{-0.02}$	< 511	> 0.3	$1.17^{+0.03}_{-0.03}$	44.16
MCG -06-30-015	$1.90^{+0.02}_{-0.03}$	> 43	< 2.0	$1.14^{+0.03}_{-0.04}$	43.71
MR 2251–178	$1.81^{+0.09}_{-0.14}$	36^{+30}_{-13}	2.5	$1.29^{+0.17}_{-0.28}$	44.56
Mrk 50	$1.96^{+0.09}_{-0.06}$	> 17	< 3.6	$1.05^{+0.13}_{-0.09}$	43.08
Mrk 6	$1.67^{+0.24}_{-0.09}$	27^{+58}_{-12}	3.5	$1.62^{+0.69}_{-0.26}$	43.28
NGC 3783	$1.87^{+0.07}_{-0.04}$	33^{+23}_{-10}	2.5	$1.19^{+0.12}_{-0.07}$	43.08

Continued on next page

Table 4.11: The mean and weighted mean of kT_e , y , and τ .

Parameter	NLS1		BLS1	
	mean	weighted mean	mean	weighted mean
kT_e [keV]	45 ± 16	11 ± 2	60 ± 10	22 ± 3
y	0.90 ± 0.07	0.97 ± 0.03	1.12 ± 0.02	1.27 ± 0.06
τ	2.8 ± 0.4	2.6 ± 0.4	2.2 ± 0.3	1.9 ± 0.3

Table 4.12: The input parameters of typical SED.

Parameter	NLS1	BLS1
SE component		
E_{br} [keV]	5×10^{-5}	
Γ_1	0.88	1.3
Γ_2	1.51	2.3
E_C [keV]	0.17	0.1
PL component		
Γ	2.22	2.08
roll E[keV]	0.01	

Table 4.10 continued

Object	Γ_{Comp}	kT_e [keV]	τ	y	$\log L_{2-10}$
NGC 4151	$1.84^{+0.05}_{-0.04}$	89^{+62}_{-24}	1.3	$1.25^{+0.08}_{-0.07}$	42.78
NGC 4593	$1.95^{+0.01}_{-0.01}$	> 69	< 1.4	$1.07^{+0.01}_{-0.01}$	42.78
NGC 6814	$1.89^{+0.12}_{-0.07}$	38^{+58}_{-15}	2.2	$1.15^{+0.20}_{-0.11}$	41.00
SWIFT J0917.2–6221	$1.78^{+0.24}_{-0.23}$	28^{+61}_{-13}	3.1	$1.36^{+0.49}_{-0.48}$	44.00

Table 4.13: The central BH mass and luminosity of Seyfert 1 galaxies used in this work.

Object	$\log M_{\text{BH}}$	$\log L_{\text{Edd}}$	$\log L_{\text{bol}}$	$L_{\text{Edd}}/L_{\text{bol}}$	$(F_{\text{SE}}/F_{\text{PL}})_{0.5 \text{ keV}}$	$\log L_X$	L_{UV}	L_X/L_{UV}
Mrk 110	7.40	45.51	45.97	2.85	0.93	44.25	44.85	0.25
SWIFT J212745.6+565636	7.18	45.29	45.72	2.68	0.18	43.77	43.66	1.29
IGR J16185-5928	7.40	45.51	45.78	1.87	0.41	43.75	44.00	0.57
IGR J14552-5133	6.30	44.41	44.62	1.61	3.53	43.16	44.15	0.10
IGR J16385-2057	6.83	44.95	44.91	0.91	3.53	43.41	44.64	0.06
IGR J19378-0617	6.48	44.59	45.18	3.91	3.53	43.60	45.04	0.04
2E 1853.7+1534	8.35	46.46	45.54	0.12	7×10^{-3}	44.96	44.75	1.61
4U 0517+17	7.65	45.76	44.43	0.05	7×10^{-3}	44.63	44.68	0.88
4U 1344-60	8.24	46.35	44.37	0.01	7×10^{-3}	43.93	43.95	0.95
FRL 1146	8.24	46.35	44.69	0.02	7×10^{-3}	43.80	43.90	0.79
GRS 1734-292	8.90	47.01	44.79	0.01	7×10^{-3}	44.31	44.01	1.99
IC 4329A	8.11	46.23	45.09	0.07	7×10^{-3}	44.38	44.48	0.79
IGR J07597-3842	8.30	46.41	45.01	0.04	7×10^{-3}	44.31	44.16	1.40
IGR J12415-5750	7.96	46.08	44.37	0.02	7×10^{-3}	43.50	43.19	2.06
IGR J16119-6036	8.24	46.35	43.56	0.00	7×10^{-3}	43.65	43.72	0.85
IGR J16482-3036	8.15	46.26	44.62	0.02	7×10^{-3}	43.89	43.73	1.46
IGR J17488-3253	8.24	46.35	44.30	0.01	7×10^{-3}	43.50	43.13	2.35
IGR J18027-1455	8.24	46.35	44.51	0.01	7×10^{-3}	44.24	43.86	2.35
IGR J18259-0706	8.24	46.35	44.37	0.01	7×10^{-3}	44.27	43.95	2.09
LEDA 168563	8.24	46.35	45.17	0.07	7×10^{-3}	44.50	44.46	1.10
MCG +08-11-011	8.24	46.35	45.42	0.12	7×10^{-3}	44.26	44.32	0.86
MCG-06-30-015	7.26	45.37	44.96	0.39	7×10^{-3}	43.25	43.81	0.27
MR2251-178	9.00	47.11	45.81	0.05	7×10^{-3}	45.24	45.19	1.11
Mrk 50	7.30	45.41	44.33	0.08	7×10^{-3}	43.77	44.00	0.59
Mrk 6	8.09	46.20	44.53	0.02	7×10^{-3}	43.94	43.53	2.58
NGC 3783	6.73	44.85	44.33	0.31	7×10^{-3}	43.64	43.71	0.85
NGC 4151	7.12	45.23	44.03	0.06	7×10^{-3}	43.66	43.62	1.12
NGC 4593	6.99	45.10	44.03	0.09	7×10^{-3}	43.26	43.46	0.63
NGC 6814	6.91	45.02	42.26	0.00	7×10^{-3}	42.33	42.45	0.76
SWIFT J0917.2-6221	9.59	47.70	45.26	0.00	7×10^{-3}	44.60	44.48	1.31

Chapter 5

Radio Loud Narrow-Line Seyfert 1 Galaxy RX J1633+4718

5.1 Introduction

The origin of a soft X-ray excess emission in active galactic nuclei (AGNs) has been a long standing problem for more than 20 years. ROSAT detection of number of AGNs with a steep soft X-ray spectrum and their identification with narrow line Seyfert 1 (NLS1) galaxies (Boller et al., 1996) triggered extensive studies of the soft X-ray excess preferentially found in NLS1 galaxies. Following observations have revealed the soft X-ray excess is usually modeled with a blackbody or multi-color disk model with a temperature of 100–200 eV (Walter & Fink, 1993; Leighly, 1999b; Czerny et al., 2003). The first model considered as the origin of the soft X-ray emission is a high energy end of the UV bump, which is considered to be a thermal emission from an accretion disk. Nevertheless, the temperature of 100–200 eV is too high for standard accretion disk around a super massive black hole (SMBH) with mass of 10^6 – $10^8 M_{\odot}$. Alternative accretion disk models or Comptonization on the disk surface may be a solution, but the narrow range of the apparent temperatures have raised a question to the thermal emission from accretion disk model. Instead, a reflection from the blurred ionized accretion disk vicinity of the central BH (Crummy et al., 2006), or relativistic blurring of absorption (Done et al., 2007) have been proposed for the origin of the soft X-ray excess.

We observed a luminous NLS1, Ton S180, with Suzaku and investigated its 0.25–55 keV spectrum (Takahashi et al. (2010) and also in chapter 3). We showed that the soft X-ray excess in this source is explained with a combination of the thermal emission from the accretion disk of which temperature

is as low as 75 eV and a reflection from ionized disk surface component. The disk temperature here is a little higher than that expected from the standard disk model but consistent with a slim-disk with edge-on geometry. Nevertheless, separation of the thermal emission and the reflection component is not easy.

In general, Seyfert galaxies and its sub class NLS1s are radio-quiet (RQ). However, there found some NLS1s of which radio loudness R is greater than 10. These objects are called radio-loud NLS1s (RL-NLS1s). The first systematic study of RL-NLS1s was performed by Komossa et al. (2006). They identified 11 NLS1s as RL among 128 NLS1s in the 11th edition of the Catalogue of Quasars and Active Nuclei (Véron-Cetty & Véron, 2003). They reported that the fraction of RL-NLS1s is $\sim 7\%$ ($R > 10$) and 2%–3% ($R > 100$). Most radio loud NLS1s in their sample have steep radio spectra ($0.4 \leq \alpha \leq 2.1$, where α is a spectral index of $f \propto \nu^{-\alpha}$) in the frequency band 0.33–1.4 or 1.4–4.85 GHz, and the radio emission is compact. They evaluated black hole masses in the range $M_{\text{BH}} \sim (2-10) \times 10^7 M_{\odot}$ for 11 RL-NLS1s, and found they have luminosity very close to or above the Eddington limit. Soft X-ray spectra observed with ROSAT are similar to RQ-NLS1s, with $\Gamma_{\text{soft}} \sim 2$ to 3.5 and $L_{\text{soft}} \sim 10^{44-46} \text{ erg s}^{-1}$. Surprisingly, several RL-NLS1s have been detected in GeV γ rays with Fermi satellite (Abdo et al., 2009a,b; Calderone et al., 2012; D’Ammando et al., 2012). It indicates that at least some RL-NLS1s have similar properties to blazars.

Yuan et al. (2008) systematically studied 23 RL-NLS1s selected from the Sloan Sky Digital Survey (SDSS) data. They searched very RL-NLS1s of which radio loudness is greater than 100 and found 23 such objects from 3300 NLS1s in the Sloan Sky Digital Survey (SDSS) data release 5 (DR5). All the 23 sources are compact in radio; the size is less than a few tens of kpc. Very long baseline interferometry (VLBI) observations of several sources among 23 revealed that they are unresolved or marginally resolved at scales of about tens of parsec. The spectral energy distribution (SED) of some of the sources are similar to those of blazars from radio to soft X-rays. Employing the commonly used relation of black hole mass with H_{β} line width and luminosity, the black hole mass M_{BH} is estimated to be $10^{6-8} M_{\odot}$, which leads to the Eddington ratio $L_{\text{bol}}/L_{\text{Edd}}$ of 0.5–3. They imply that RL-NLS1s are RL-AGNs with lower masses accreting at high rates.

Among the 23 sources studied by Yuan et al. (2008), 14 sources had

been detected in the 0.1–2.4 keV X-ray band. The source RX J1633+4718 (SDSS J163323.58+471859.0) is the brightest one (Yuan et al., 2008). RX J1633+4718 was first detected in the ROSAT all sky survey (RASS) with an exposure of 909 s (Yuan et al., 2008, 2010). This source was later identified in the optical band with a NLS1 at a redshift $z = 0.116$. RX J1633+4718 was observed again with the ROSAT at its pointing mode with an exposure of 3732 s on 1993 July 24. The X-ray flux density corrected for Galactic absorption (0.1–2.4 keV) was $5.44 \times 10^{-12} \text{ erg s}^{-1} \text{ cm}^{-2}$ (Yuan et al., 2008).

Yuan et al. (2010) reported that the X-ray spectrum in the 0.1–2.4 keV energy band of this target cannot be fitted with a simple power-law model but requires a second component. Employing a blackbody model for the second component, the blackbody temperature is 32.5 eV, which could be the lowest among the temperatures of the soft X-ray excess ever measured. Note, however, that their spectral analysis is based on the position sensitive proportional counter (PSPC) aboard the ROSAT and spectral resolution is not necessarily high. In fact, the second component could either be a thin plasma emission model, a power-law model, or the multi-color disk model. When the multi-color disk model is employed, the temperature at the disk inner radius is $kT_{in} \sim 40 \text{ eV}$, which is consistent with that for a SMBH of $3 \times 10^6 M_{\odot}$. On the other hand, they interpreted the flat power-law component in the soft X-ray band is due to the inverse Compton component from the jet, since they have smooth connection from radio and UV (Yuan et al., 2010).

RX J1633+4718 was also observed with the very long baseline interferometry (VLBI) at 1.7 GHz (Doi et al., 2011), 5 GHz (Gu & Chen, 2010), and 8.4 GHz (Doi et al., 2007). These observations showed that this source has a compact structure less than $10''$ milliarcsecond (Doi et al., 2007) and the relativistic jet of which position angle (P.A.) is $\sim 80^{\circ}$ (Gu & Chen, 2010; Doi et al., 2011). The spectral indices derived from the flux densities ($f_{\nu} \propto \nu^{-\alpha}$) were $\alpha = 0.57 \pm 0.20$ at 1.7 GHz (Doi et al., 2011), $\alpha = 0.73$ between 1.6 and 8.4 GHz, and $\alpha = 1.73$ between 5 and 8.4 GHz (Gu & Chen, 2010). Doi et al. (2011) argued that these radio properties cannot generally be attributed to strong Doppler beaming but were associated with compact lobes with a sub-relativistic speed similar to that seen in the compact steep spectrum objects, which are probably an AGN class of young radio galaxies.

The SDSS data provided the optical spectral properties; the width of H β was found to be $909 \pm 43 \text{ km}$ (Yuan et al., 2008). The "thermal" continuum

luminosity at 5100 Å estimated from the $H\beta$ luminosity is $\lambda L_{\lambda 5100} = 2.63 \times 10^{43} \text{ erg s}^{-1}$ (Yuan et al., 2010). The "thermal" bolometric luminosity can then be estimated as $L_{\text{bol}} = 2.6(\pm 0.5) \times 10^{44} \text{ erg s}^{-1}$, adopting the bolometric correction $k = 10 \pm 2$ (1σ) for RQ AGNs (Richards et al., 2006). The BH mass estimated from the broad Balmer line width and the luminosity of either broad line or the "thermal" continuum lies within $M \simeq (2.0 - 3.5) \times 10^6 M_{\odot}$ (Yuan et al., 2010). The estimated Eddington ratio is then $L/L_{\text{Edd}} = 0.69^{+0.73}_{-0.35}$ using the above "thermal" bolometric luminosity (Yuan et al., 2010).

As mentioned above, RXJ1633+4718 have strange X-ray spectrum according to the ROSAT observations. Nevertheless, the source had not been observed with ASCA, Chandra, XMM-Newton, or Suzaku (Mitsuda et al., 2007) for about 20 years. Furthermore, the multi-wavelength spectrum reported in Yuan et al. (2010) is not from simultaneous observations. We hence proposed to observe this source with Suzaku, and planned simultaneous observations in radio, infrared, and optical band. Suzaku X-ray Imaging Spectrometer (XIS) (Koyama et al., 2007) is best for this target with its good energy resolution at soft X-ray band and wide energy range coverage. In order to study variability in various time scales, X-ray observations were performed four times, two in 2011 and two in 2012. For the last two observations, quasi-simultaneous observations in radio band (VLBI network in Japan) and infrared to optical band ("Kanata" 1.5-m telescope) were performed. We adopt cosmological parameters of $H_0 = 70 \text{ km s}^{-1}$, $q_0 = 0.0$, and $\lambda_0 = 0.73$.

5.2 Observation

5.2.1 X-ray

RX J1633+4718 was observed by Suzaku in 2011 and 2012. Table 5.1 summarizes the start time, the end time, and the XIS exposures of each observation. The observation was carried out with the X-ray Imaging Spectrometer (XIS:Koyama et al. (2007)) and the Hard X-ray Detector (HXD:Takahashi et al. (2007); Kokubun et al. (2007)). The target was placed at the nominal center of the XIS field of view. The XIS consists of 4 CCD cameras: three (XIS0, XIS2, XIS3) with front illuminated (XIS-FI) CCDs and one (XIS1) with a back illuminated (XIS-BI) CCD. Since XIS2 was not available after 2006 November 9, the other three CCDs were used. The normal full-window

clocking mode with the spaced-row charge injection (SCI:Uchiyama et al. (2009)) was employed. The XIS edit mode was 3×3 and 5×5 , and the data of both modes were combined in our analysis.

Standard reduction procedures were applied to the XIS data. We extracted the source products from a circle regions of $2'$ radius centered on the source, while the background ones were extracted from the annular regions with inner and outer radii $4'$ and $6'$, respectively. The redistribution matrices and the ancillary response files for spectral analysis were made for each XIS using `xisrmfgen` and `xissimarfgen` (Ishisaki et al., 2007), respectively. XIS spectra from two XIS-FI CCDs were combined by `mathpha`. Correspondingly, the redistribution matrices and the ancillary response files for the XIS-FI CCDs were combined by using `addrmf` and `addarf`, respectively. The source spectra were grouped such that each spectral bin contains at least 50 counts in the spectral fitting.

In making the ancillary response files, we used the following latest contamination files: `ae_contami_xi?_20120719.fits`, which included the CALDB supplied in October 15 in 2012. While the previous files are assumed that `contami` was composed of $C_{24}H_{38}O_4$ and its composition ratio did not have time variability, we assume that the composition ratio has time variability and moreover, we add the Nitrogen for XIS1.

HXD data reduction was also performed to check whether this source has the X-ray emission above 10 keV. We used the HXD data from the 1st, 3rd, and 4th observations, as the HXD was not operated in the 2nd observation. Our analysis shows, there found no significant detection of this source with the HXD. In the case of the 3rd observation, when the X-ray emission in the 0.5–12 keV was the brightest, there was the 5% flux of Non X-ray Background (NXB) left in the 15 – 40 keV energy band when we subtracted the NXB and the Cosmic X-ray Background (CXB) components from the raw flux. Our evaluation of the uncertainty of the NXB model leads to 2.9% NXB for 1σ , and 5% flux means positive detection but with confidence level of about 90%. We also examined whether the X-ray emission above 10 keV was detected during the 1st and 4th observations. However, we found that neither of them were significantly detected. The residuals after subtracting the background components (NXB+CXB) were -0.6% for the 1st and 0.8% for the 4th, respectively. The uncertainties of NXB model were 3% overestimation for the 1st and 5.2% underestimation for the 4th, respectively. Taking into

account the uncertainty of the NXB, there were 4% flux (1st) and 2% flux (4th) of NXB left in the 15–40 keV energy band. Both spectra were able to be explained with the CXB. We here conclude that the hard X-ray emission above 10 keV during Suzaku observations is not highly significant. We thus employ the XIS data in this paper.

5.2.2 Radio

RX J1633+4718 was observed at 8.4 GHz with the Japanese VLBI Network (JVN), a newly-established VLBI network. We used 873 km baseline for Yamaguchi-Hitachi line. The observation dates and telescope participants are listed in table 5.2. Right-circular polarization was received in two frequency bands, 8400–8416 MHz (IF1) and 8432–8448 MHz (IF2), providing a total bandwidth of 32 MHz. The VSOP-terminal system was used as a digital back-end, digitized data in 2-bit quantization were recorded onto magnetic tapes at a data rate of 128 Mbps. Correlation processing was performed using the Mitaka FX correlator (Shibata et al., 1998) at the National Astronomical Observatory of Japan. Since Doi et al. (2007) reported that the flux density of the source was 21.2 mJy at 8.4 GHz, the marginal detection with Yamaguchi-Hitachi baseline was predicted. Thus, the radio observation consists of 2 parts, the former is a phase-compensation, the latter is a self fring-fitting.

RX J1633+4718 is found to have a compact structure less than 10 milli arcsecond from the result of JVN observation (Doi et al., 2007). Although the spatial resolution at 8.4 GHz is predicted 8 mas, the real resolution which we obtained from the spatial frequency distribution was 10.9–17.2 mas. This depends on the effect of changing the baseline seen from the source due to the Earth rotation. In other words, the source was not able to be spatially resolved if we use the spatial resolution composed in this JVN observation. So, we regarded that the relative flux density obtained with the Yamaguchi-Hitachi baseline is the same as that obtained with the single mirror observation.

Data reduction was performed using the Astronomical Image Processing System (AIPS, Greisen (2003)) developed at the US National Radio Astronomy Observatory and Difmap software (Shepherd, 1997). The former was used for the calibration part and the latter was used for the acquisition and the comparison of the correlation amplitude coefficients based on the visibility. The phase-compensation observation was performed by the following schedule: -P.R.-RX J1633+4718-P.R.-..., where P.R. represents the

phase-compensation target, J1633+47 (R.A.=16^h37^m45.1306^s, 47°17'33.831" at J2000 coordinate) referred to the Hitachi antenna. It is noted that we performed the phase-compensation observation for 1 hour and 40 minutes.

While the flux density of RX J1633+4718 was around 20 mJy, the root-mean-square uncertainty was reduced to be around 2–3 mJy with an integration time of 3-5 minutes. Thus we used the last 11 minutes for the self fringing-fitting of the target because it was possible to detect significantly the fringing of the target during the Coherence time at 8 GHz.

5.2.3 Near Infrared and Optical

We performed photopolarimetric observations of RX J1633+4718 simultaneously in the optical B -, V -, and the NIR J -, and K_s -bands in 2012/01/06 and 2012/02/04. We used TRISPEC attached to the 1.5 m Kanata telescope at Higashi-Hiroshima Observatory. TRISPEC is capable of simultaneous three-band (one optical and two NIR bands) imaging or spectroscopy, with or without polarimetry (Watanabe et al., 2005). TRISPEC has one CCD and two InSb arrays.

We also observed in the multi-color photometric mode in the R_C - and I_C -bands during the 2012/01/16 observation using HOWPol (Hiroshima One-shot Wide-field Polarimeter: Kawabata et al. (2008)) attached to a Nasmyth focus of the Kanata telescope. In the observation of RX J1633+4718, unfortunately, HOWPol was not available due to the maintenance of the instrument in the 2012/02/04 observation. Thus, we used only the data in 2012/01/16 for the R_C - and K_s -bands. Table 5.3 presents the observation date, the instrument, the aperture size, and the exposure time of each image.

Thanks to Kanata team of Hiroshima University, we obtained the near infrared and optical spectra. We performed differential photometry, with a standard star, PG 1530+057. Its position is R.A.=15h30m10.737s, Dec=+05d32m26.85s (J2000) and its magnitudes are $B = 14.362$, $V = 14.211$, $R = 14.049$, and $I = 14.012$ (Landolt, 1992). After differential photometry, we calculated the flux, assuming that Vega 0 mag corresponds to the flux with 4020, 3590, 3020, 2380, 1630, and 667 Jy in the B , V , R_C , I_C , J , and K_s bands. The results are summarized in table 5.4. Moreover, we detected the polarization of RX J1633+4718 in the Kanata observation for the first time as shown in figure 5.1. The polarization angle and polarization magnitude were $\sim 120^\circ$ and $\sim 5\%$, respectively. Compared them with the polarizations of surround-

ing sources, the polarization detected in the Kanata observation is likely to be the intrinsic polarization of RX J1633+4718. The possibility that the polarization is due to the host galaxy of RX J1633+4718 is not rejected.

As shown in figure 5.2, RX J1633+4718 resides in one galaxy of a galaxy pair, with the other being a starburst galaxy (Name:SDSS J163323.53+471902.7, R.A.=16h33m23.5s, Dec=+47d19m03s) separated by 4'' (Yuan et al., 2010). Since the aperture radius of Kanata ranges 5'' – 9'' as shown in table 5.3, we measured the integrated fluxes of two galaxies. Then, we had to take into account the host galaxy contribution and the starburst galaxy.

5.3 Spectral Analysis

5.3.1 X-ray spectral analysis with Suzaku

In this section, we consider the time averaged spectra of RX J1633+4718 obtained with Suzaku. We fitted the XIS-FI, XIS-BI spectra using XSPEC v12. All errors quoted in the text and tables are at the 90% confidence level, unless otherwise noted, while those quoted in the figures are at the 68% confidence level. We fix the Galactic absorption and redshift at $N_{\text{H,Gal}} = 1.57 \times 10^{20} \text{ cm}^{-2}$ and $z = 0.116$, respectively. We set the energy ranges of 0.4–12 keV and 0.25–8 keV for the XIS-FI and the XIS-BI spectra, respectively. The XIS spectra between 1.7 keV and 1.9 keV are ignored because of the calibration uncertainty.

We start the spectral analysis by fitting the 0.5–2.4 keV band spectra in the 1st observation with a simple power-law model modified by the Galactic absorption. This fit provide us $\chi^2 = 113.40$ for degree of freedom (dof) = 110, indicating that the spectrum in this band is approximated with a simple power-law with a photon index of 1.57 ± 0.07 . Extrapolating the model to the 0.25–12 keV band, however, shows that the spectra have a soft X-ray excess and a hard X-ray curvature, as shown in figure 5.3. In order to check whether the soft excess and the curvature are seen in the other observations, we compare the best-fit model of the 1st 0.5–2.4 keV spectrum to the 3 spectra in the following observations, without performing any fit. The plot is displayed in figure 5.4. The spectra in the following 3 observations also show the soft excess and the curvature.

We next try to model the X-ray spectra with combinations of 2 components. We approximate the soft X-ray excess with a disk-blackbody (`diskbb`)

or a power-law (`powerlaw`), while the curvature component with a cut-off power-law (`cutoffpl`), a log-parabolic (`logpar`), or a broken power-law (`bknpow`). As a result, any combinations reproduced the 0.25–12 keV X-ray spectra of 4 observations well. We summarize the best-fit parameters in table 5.7. Figure 5.5 shows the data and best-fit model using `diskbb+logpar`. Note that the curvature or cutoff of similar energy that we observed has not yet been observed in this source and any other AGNs.

Figure 5.6 shows the comparison the best-fit model of 4th spectrum with the spectra in the following 3 observations. This figure indicates that the soft X-ray excess is rather stable compared to the hard curvature component. The hard curvature component is the brightest in the 3rd observation and the faintest in the 4th observation. There is about 40% intensity variability among 4 observations.

Fitting the soft X-ray component with disk-blackbody model provides the disk inner temperature and radius. The 90% contour for those two parameters is shown in figure 5.7, in which we assume the BH mass, the inclination angle, and the distance to the source $3 \times 10^6 M_\odot$, 30° , 495 Mpc, respectively. Figure 5.7 indicates that the disk inner temperature and the radius range 50–90 eV and $0.5\text{--}2 R_g$, respectively. As mentioned in section 5.1, the blackbody temperature is typically 100–200 eV for other (mostly radio quiet) AGNs, which is too high for the thermal emission from the accretion disk of a central BH mass of $10^{6-8} M_\odot$. However, in the case of RX J1633+4718, the disk blackbody temperature is similar to that expected for a $3 \times 10^6 M_\odot$ SMBH (20–30 eV).

We show the 90% contours for the hard curvature component as well. Figure 5.8 shows the contour of Γ and E_C when we employ a cutoff power-law (`cutoffpl`) model. Γ and E_C in the 3rd observation are the flattest and the lowest among four observations, while those for other 3 observations are consistent each other. Figure 5.8 also indicates E_C is less than 10 keV for all the observations. Since the cut-off energy E_C of the power-law continuum is observed to be 100–300 keV (Zdziarski et al., 2000; Petrucci et al., 2001; Dadina, 2008) for sample of Seyfert 1 galaxies (mostly BLS1), E_C for RX J1633+4718 is nearly 2 orders of magnitude lower than those.

We next examine whether Fe emission lines are seen in the 6–7 keV band or not. A Gaussian model (`zgauss` in Xspec) is added to `diskbb+logpar` model. As the Fe $K\alpha$ line is not clearly seen for each observation., the line

center energy and the line width is fixed at 6.4 keV and 0.01 keV, respectively. Its normalization is left free. The 90% upper limit for the EW of the line in the 3rd observation is 115 eV. Note that the reflection continuum does not exist or very weak. In fact, when we replaced the `cutoffpl` and the `logpar` model with `pexrav`, which represents the sum of the power-law and reflection component, the relative reflection strength, R , is pegged at 0.

5.3.2 From Infrared to Optical

We here extract the SED of the AGN component of RX J1633+4718 near-infrared and optical band. Table 5.4 summarize the photometric results obtained with Kanata, their raw flux data are plotted in figure 5.9. Since the galactic extinction was not corrected in the Kanata data reduction, we had to correct it. Table 5.5 summarizes the extinction at each band cited from Table 6 in Schlafly & Finkbeiner (2011). We assume the extinction law is parameterized by $R_V = A_V/E(B - V)$, where $R_V = 3.1$. Figure 5.10 represents the comparison between the spectra with the galactic extinction and that without taking into account one. From figure 5.10, we conclude that the spectra between near-infrared and optical are not significantly affected by the galactic extinction. We hence use the spectra without this correction.

RX J1633+4718 pairs with a starburst galaxy and the spatial resolution of Kanata is not able to distinguish them as mentioned in section 5.2.3. The photometry results of Kanata is contaminated by both host galaxies. We need to extract the AGN component by subtracting the both host-galaxy components, by employing the data of IRAS, AKARI, and WISE published in NASA/IPAC Extragalactic Database (NED). In order to build the host-galaxy components of the SED of RX J1633+4718 and SDSS J163323.53+471902.7, we used the template files of SWIRE library (Polletta et al., 2007) in which SED is normalized at 5500 Å. We used them for RX J1633+4718 and SDSS J163323.53+471902.7 by referring the SDSS and 2MASS, data for each galaxy. We calculated the flux density of the template at 5100 Å so as to reproduce the optical spectra shown in Yuan et al. (2008) by combining 6 SED templates files for spiral galaxies supplied by SWIRE library. We found that we should adjust the flux density at 5500 Å to be $12 \times 10^{-17} \text{ erg s}^{-1} \text{ cm}^2 \text{ Å}^{-1}$. In this case, the host-galaxy component of RX J1633+4718 accounts for 20% of the raw flux density at 5100 Å observed with Kanata. We made the template of SDSS J163323.53+471902.7 as well. The flux of this starburst galaxy is sum-

marized in table 5.6. We combined 6 templates for the starburst galaxies in the SWIRE library and adjusted the normalization so as to reproduce the spectrum of the starburst galaxy. We found that the normalization at 5500 Å should be $31 \times 10^{-17} \text{ erg s}^{-1} \text{ cm}^2 \text{ Å}^{-1}$ to reproduce the spectrum well as shown in figure 5.12.

Figure 5.13 shows the SED of RX J1633+4718 and the host-galaxy components of RX J1633+4718 and SDSS J163323.53+471902.7. In the near infrared to optical band, the observed flux with Kanata is significantly higher than the sum of host-galaxy components. On the other hand, the far infrared hump is almost explained with the starburst galaxy component. We show the nucleus SED of RX J1633+4718 with subtracting the host-galaxy components in figure 5.14. In figure 5.14, we add the X-ray and radio fluxes to the nucleus SED. The nucleus component accounts for $\sim 60\%$ of observed flux at B band.

5.4 Discussion

We have investigated the X-ray spectra of RX J1633+4718 obtained with Suzaku and have extracted the optical and infrared SED of the nucleus to make wide band SED from radio to X-rays. The SED (figure 5.14) shows that at least three spectral components are needed to explain, i.e., one component at radio to near infrared, one component at optical to soft X-ray, and one at medium X-ray band. We mainly focus on the latter two components in which X-ray data contribute.

5.4.1 Less variable component from near infrared to soft X-ray band

Although there are no data point in the SED of UV to EUV band, optical data points and soft X-ray data points can have a smooth connection. This component is most likely a thermal emission from a accretion disk. Nevertheless, if we extrapolate the soft X-ray spectrum to the longer wave length, assuming the disk blackbody model is valid over this range, the model underestimate the optical flux about 2 – 3 orders of magnitudes (See Figure 5.16). If we introduce another blackbody component with temperature of 1 eV, the optical flux is reproduced, as shown in figure 5.17. This second blackbody component has a luminosity of $L_{\text{bb}} \sim 2.3 \times 10^{44} \text{ erg s}^{-1}$. Adding the disk blackbody luminosity

of $1.2 \times 10^{44} \text{ erg s}^{-1}$, the total luminosity of $\sim 3.5 \times 10^{44} \text{ erg s}^{-1}$ is obtained. This is very close to the Eddington luminosity of $L_{\text{Edd}} \sim 3.9 \times 10^{44} \text{ erg s}^{-1}$ for $M_{\text{BH}} = 3 \times 10^6 M_{\odot}$.

The second blackbody component might be thermal emission from outer disk, but its origin is not certain. We hence employ an accretion disk model alternative to the standard disk model, called p -free disk model, $T(r) \propto r^{-p}$ (`diskpbb`, Mineshige et al. (1994)). As shown in Figure 5.18, optical to soft X-ray spectrum is reproduced with this model. The parameters we adopted here is $kT_{\text{in}} = 86 \text{ eV}$, $R_{\text{in}} = 0.3R_g$, and $p = 0.5$, where we assume the central BH mass and the inclination angle to be $3 \times 10^6 M_{\odot}$ and 30° , respectively. The luminosity of this p -disk component is $1.2 \times 10^{45} \text{ erg s}^{-1}$, which is about 4 times the Eddington limit. Note also that the disk inner radius r_{in} is derived from $1.25 \times 10^6 / \sqrt{\cos \theta} r_g$ with this model. It is not certain whether this factor is reconciled with the uncertainty in the BH mass estimation by the empirical method using optical line width and luminosity and the inclination angle we have assumed.

Another possibility is this object is radiating at the super-Eddington luminosity. In fact, p -free disk model of $p \sim 0.5$, super-Eddington luminosity, and disk inner radius much smaller than $6r_g$ are the characteristics of an optically thick advection-dominated disk, so-called slim disk (Watarai et al., 2000). The slim disk state is reported in some ultraluminous X-ray sources (ULXs) such as M 81 X-9 (Tsunoda et al., 2006), M 82 X-1 (Okajima et al., 2006), and NGC 1313 (Feng & Kaaret, 2007) and so on. If the accretion disk of RX J1633+4718 is a slim disk state, we can calculate the expected temperature at the disk inner radius by using the following equation (Mineshige et al., 2000):

$$T \sim 2 \times 10^6 \left(\frac{M_{\text{BH}}}{10^5 M_{\odot}} \right)^{-1/4} \left(\frac{r}{r_g} \right)^{-1/2} \text{ [K]}. \quad (5.1)$$

Assuming the central BH mass M_{BH} and the disk inner radius r_{in} to be $M_{\text{BH}} = 3 \times 10^6 M_{\odot}$ and $r_{\text{in}} = 1r_g$, respectively, the disk temperature expected from equation (5.1) is $T \sim 1.2 \times 10^6 \text{ [K]}$, corresponding to $kT_{\text{in}} \sim 104 \text{ eV}$. This value is close to 70-90 eV obtained in the observation. If the mass of the black hole is lower, $M_{\text{BH}} = 3 \times 10^5 M_{\odot}$, r_{in} should be $r_{\text{in}} \sim 3r_g$ to account for the observed luminosity and the disk temperature is expected to be $kT_{\text{in}} \sim 105 \text{ eV}$.

We examined the effect of electron scattering at the surface of the disk as well as Ton S180 discussed in chapter 3. In the case of RX J1633+4718,

the critical temperature calculated from equation (3.1) is $kT_{\text{Comp}} \sim 34 \text{ eV}$, assuming $M_{\text{BH}} = 3 \times 10^6 M_{\odot}$ and $\dot{m} = 1$. Calculating the color correction factor of RX J1633+4718 from equation (3.2), we obtain $f_{\text{col}} \sim 2.2$. Thus the true effective temperature is $kT \sim 28 \text{ eV}$, which is much smaller than that predicted from the standard accretion disk model of $kT \sim 57 \text{ eV}$ (assuming $M_{\text{BH}} = 3 \times 10^6 M_{\odot}$, $\dot{m} = 1$, and $r_{\text{in}} = 6r_g$).

We hence conclude that the optical to soft X-ray spectrum of RX J1633+4718 is best explained with a slim disk radiating at super-Eddington luminosity.

5.4.2 Variable component in the X-ray band

We have modeled the component dominant in the intermediate X-ray band either with a cutoff power-law, log parabola, or broken power-law model. The cutoff energy of 3 to 5 keV was not observed in this source and any other radio quiet AGNs. The origin of this component is completely unknown, but the candidate is Synchrotron self-Compton or thermal Comptonization. The former is often observed in radio-loud AGNs, especially blazars, while the latter is the model for the X-ray power-law component in radio-quiet AGNs.

In the case of the Synchrotron Self Compton

We first assume this component as the Synchrotron self Compton (SSC) component. We employ publicly available Synchrotron self-Compton (SSC) code developed by Krawczynski et al. (2004). The SSC mechanism assumes an isotropic population of high-energy electrons that emit Synchrotron radiation followed by inverse Compton scattering of the Synchrotron photons to higher energies. We include the data from far-infrared to middle-infrared data observed with IRAS, AKARI, and WISE to use as the upper limit of the Synchrotron component. We fixed the bulk Lorentz factor of emitting matter (Γ) and the size of emission region at 10, 0.01 pc, respectively, the value reported in Kubo et al. (1998). Other parameters such as the electron minimum energy (E_{min}), maximum energy (E_{max}), electron energy at break of powerlaw (E_{br}), spectral index of electron spectrum p_1 ($E_{\text{min}} \leq E \leq E_{\text{br}}$), p_2 ($E_{\text{br}} \leq E \leq E_{\text{max}}$) are fixed as well. We allowed the parameters of magnetic field B and the electron energy density to vary to approximate the data normalization.

We summarize the result of the SSC model fitting in figure 5.19 and table 5.9. It is clear that the SSC model is not able to reproduce the steep curvature seen above 2 keV. In order to reproduce the curvature, we allow the parameters of E_{\min} , E_{\max} , E_{br} , p_1 , and p_2 to be free. Figure 5.20 and table 5.10 summarizes the result of this fit. Although the steep curvature is explained with the SSC model, the electron energy distribution is very narrow, almost mono-energetic. Physically this is not likely. Furthermore, compared with the high-frequency-peaked blazar 1ES 0229+200, which has the narrowest electron distribution among the extreme blazars known to date ($E_{\min} = 2 \times 10^{11}$ eV, $E_{\text{br}} = 3.2 \times 10^{13}$ eV, and $E_{\max} = 10^{14}$ eV, Kaufmann et al. (2011)), the electron distribution of RX J1633+4718 is narrower by 3 orders of magnitude.

We thus conclude that the intermediate energy X-ray component with curvature is difficult to be explained with the SSC model .

In the case of the inverse Compton from the accretion disk

Another interpretation of the intermediate energy X-ray component with curvature is the inverse Compton scattering of soft photons from the accretion disk by thermal electrons in an accretion corona surrounding the central BH. As mentioned above, the electron temperature is lower than nearly 2 orders of magnitude than for BLS1 sources. We have shown that the two NLS1 sources among three we studied have the cutoff energy of 10-30 keV. We interpret this with effective Compton cooling with larger mass accretion rate. Naively, we can regard the RL-NLS1 RX J1633+4718 as its extreme case. Interestingly, the Compton y parameter for RX J1633+4718 is $1.3_{-0.2}^{+0.3}$ and not so much different from that of NLS1s and BLS1s.

We further examine the X-ray spectra of RX J1633+4718 by using a thermal Comptonization model (`compTT` in Xspec, Titarchuk (1994); Titarchuk & Lyubarskij (1995); Hua & Titarchuk (1995)). We first attempt to fit the whole 0.25–12 keV spectrum with one `compTT` component, but fail to reproduce the spectrum. Two components of `compTT` with different τ and kT_e cannot reproduce the spectra, either. It is found that an extra soft X-ray thermal component, for which disk blackbody is employed, is needed. The results of the spectral fit is shown in figure 5.21 and table 5.11. The electron temperatures are $2.7_{-0.7}^{+188}$ keV and $0.64_{-0.05}^{+9.26}$ keV, though loosely constrained. The necessity of the disk blackbody component suggests that the accretion

corona model that uniformly covers the accretion disk cannot account for the observations. As inferred from the Compton cooling time, the corona should be localized and likely highly inhomogeneous. Moreover, the fact that no apparent reflection component is observed and disk thermal component is observed barely, are the evidence that the accretion corona is localized on small area on the disk.

Although one may consider possible absorption in such a low temperature corona (Hayashida et al., 2007), the ion temperature and ionization temperature should be much higher than the electron temperature in the corona.

5.4.3 Contribution of the thermal bremsstrahlung

We also examine how the bremsstrahlung cooling contribute. We consider a homogeneous corona of $kT_e = 1.5 \text{ keV}$ and $\tau = 10$ within an accretion disk which inner radius is $10 R_g$. We assume $M_{\text{BH}} = 3 \times 10^6 M_\odot$. In this case, the electron number density of the corona is $n_e \sim 3.5 \times 10^{12} \text{ cm}^{-3}$. Then, the power per unit volume emitted by thermal bremsstrahlung ϵ^{ff} is obtained by the following equation (Rybicki & Lightman, 1979; Beckmann & Shrader, 2012):

$$\epsilon^{ff} \equiv \frac{dW}{dt dV} = 1.8 \times 10^{-25} \left(\frac{kT_e}{1 \text{ eV}} \right)^{1/2} n_e^2 [\text{erg s}^{-1} \text{ cm}^{-3}]. \quad (5.2)$$

From equation (5.2), we obtain $\epsilon^{ff} \sim 83 \text{ erg s}^{-1} \text{ cm}^{-3}$. Integrating dV , the total power is $2.9 \times 10^{40} \text{ erg s}^{-1}$. Thus, for the case of RX J1633+4718, we found that the bremsstrahlung cooling is much smaller than the Compton cooling of about $10^{43} \text{ erg s}^{-1}$.

5.4.4 What makes the X-ray spectra of RL-NLS1 RX J1633+4718 unique ?

We have interpret the strange X-ray spectra of RX J1633+4718 with two components; one is bare emission from a slim disk radiating at super-Eddington luminosity, the other is thermal Comptonization component but with extremely low electron temperature of a few keV. Either component is expected to appear in high accretion state. Comparing the corresponding properties of (general) NLS1s, RX J1633+4718 might be an extreme case of NLS1s, probably due to higher accretion rate.

It is not certain its relation to the radio loudness, i.e., cause or result. As suggested by Yuan et al. (2010), jets might blow out significant part of the accretion corona, and hence bare disk is seen. We need physical model to examine this hypothesis. In any case, RX J1633+4718 provides challenges for the accretion physics from various aspects.

5.5 Summary in RX J1633+4718

We observed the RL-NLS1, RX J1633+4718 with Suzaku in 2011 July 1, 18 and 2012 January 13 and February 5. In 2012 observations, we performed the quasi-simultaneous multiwavelength observations with Kanata and VLBI. The X-ray spectra we obtained is modeled with a combination of a disk blackbody model which disk inner temperature and radius are $kT_{in} \sim 60$ eV and $R_{in} \sim 1 R_g$, and a cutoff power-law model which photon index and cutoff energy are $\Gamma \sim 1.3$ and $E_C \sim 5$ keV. The multiwavelength spectrum from near infrared to soft X-ray is reproduced with the disk blackbody model of $kT_{in} \sim 86$ eV, $R_{in} \sim 0.3 R_g$, and $p = 0.5$, leading to the first AGN to detect the emission from the slim disk. On the other hand, for the power-law component, it is difficult to explain the curvature of few keV with a Synchrotron self Compton model unless the electron energy distribution is mono-energetic. When we regard it as the inverse Compton scattering from the accretion corona with the electron temperature 1.5 keV, it is indicated that the Compton cooling becomes more efficiently than normal NLS1s. Moreover, the bare radiation from the disk requires that the accretion corona does not uniformly cover the accretion disk but should be localized and likely highly inhomogeneous.

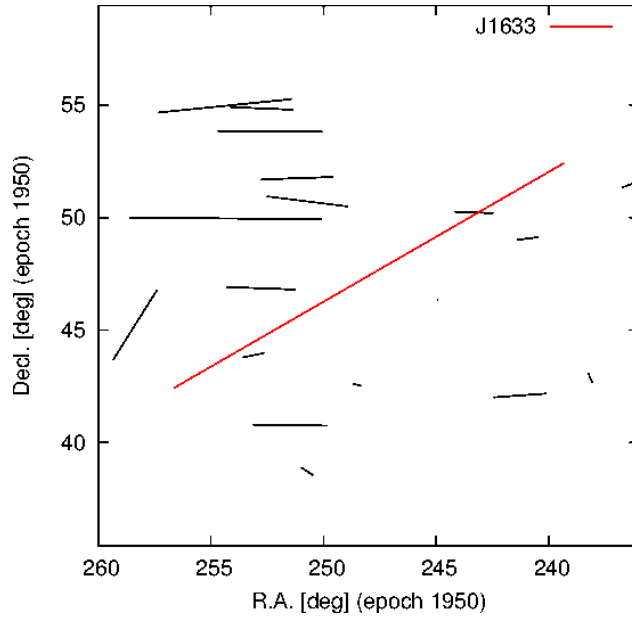


Figure 5.1: The polarization of RX J1633+4718 (red). The black lines are the polarizations observed previously. The polarization angle and magnitude are $\sim 120^\circ$ and $\sim 5\%$, respectively.

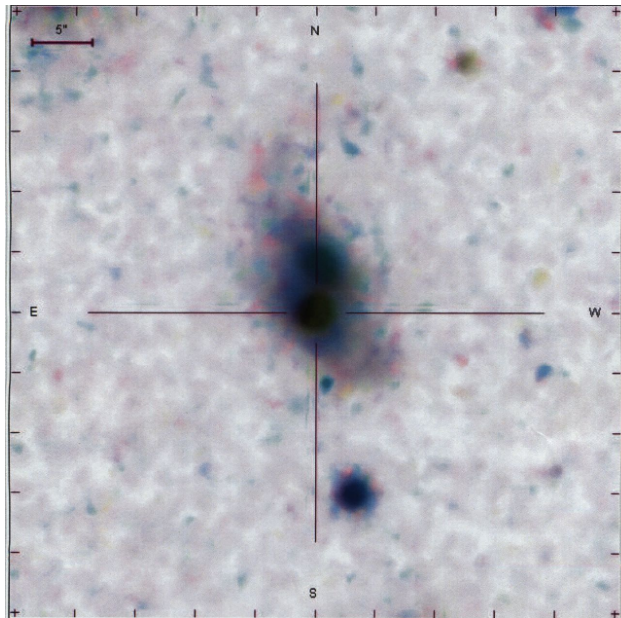


Figure 5.2: The SDSS image of RX J1633+4718.

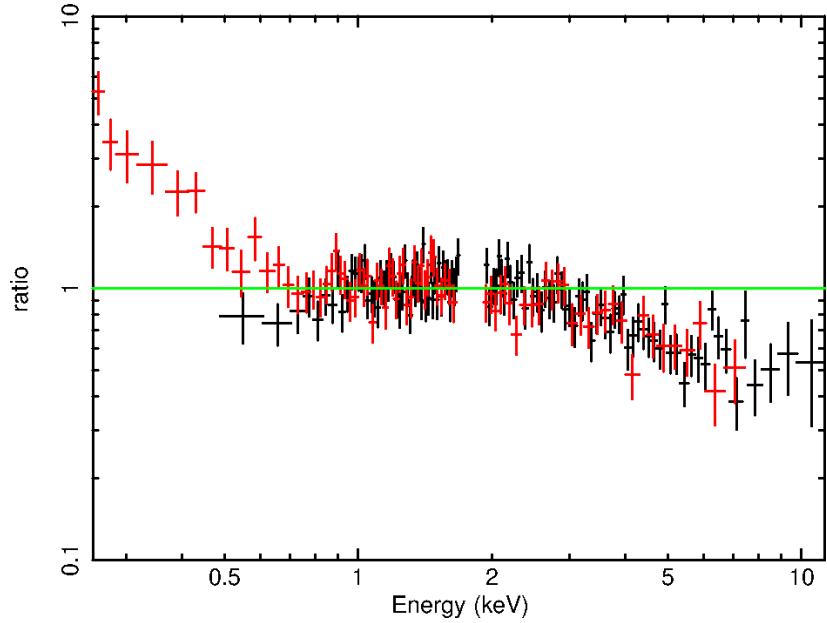


Figure 5.3: The 1st Suzaku XIS spectra of RX J1633+4718 as a ratio to an absorbed power-law model of photon index $\Gamma = 1.52 \pm 0.07$. There is an excess below the 0.5 keV and a curvature above the 2 keV.

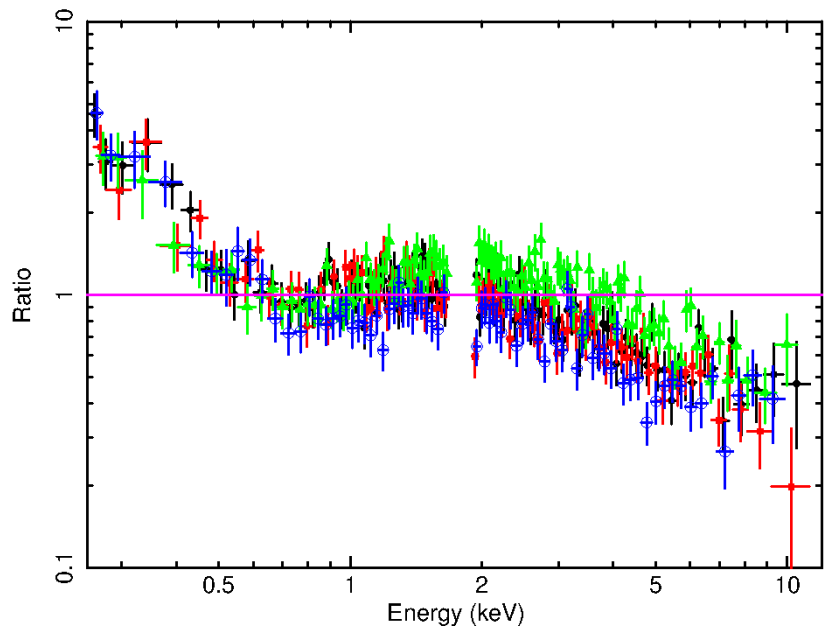


Figure 5.4: The spectral profiles of RX J1633+4718 fitted in the 1st 0.5–2.4 keV range with a simple power-law model of $\Gamma = 1.52 \pm 0.07$. Data of 1st, 2nd, 3rd, and 4th are shown in circles (black), squares (red), triangles (green), and opened circles (blue), respectively.

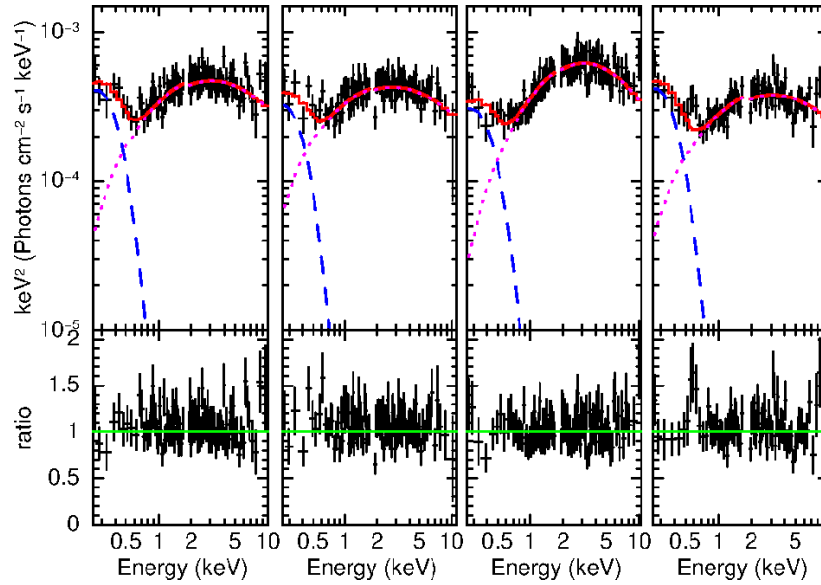


Figure 5.5: (top)The spectra in the 0.25–12 keV and the best fit model. The unfolded spectra in the form of $E^2 I(E)$ are displayed. Black points with error bars are the data from the XIS. The XIS-BI spectrum above 1.9 keV and the XIS-FI spectrum below 1.7 keV are not displayed for clarity. The model curve for the total is plotted in red lines (solid), while the cut-off powerlaw continuum in magenta (dotted), the disk blackbody component in blue (dashed), respectively. (bottom)The data/model ratio.

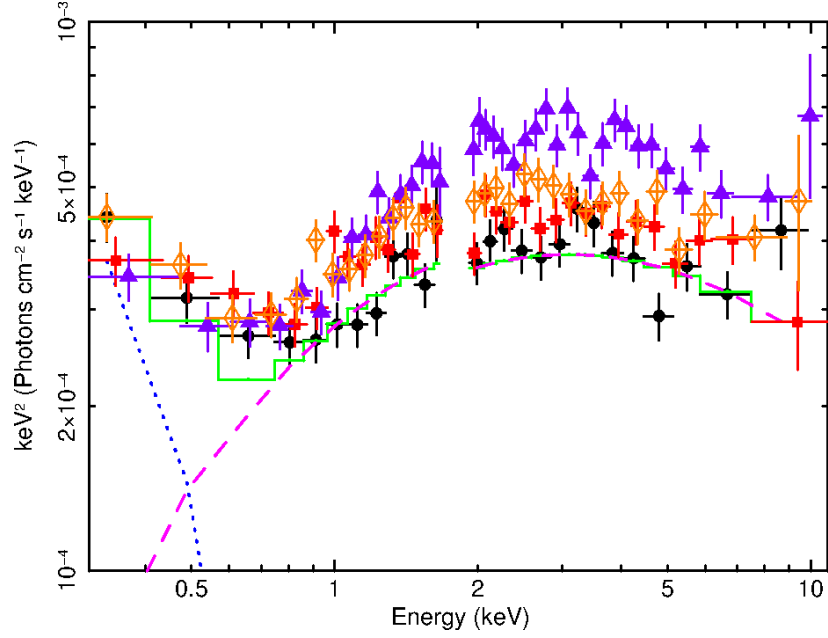


Figure 5.6: The overplot of RX J1633+4718 X-ray spectra (Orange:1st, Red:2nd, Purple:3rd, Black:4th). The green solid line, blue dotted line, magenta dashed line are the total model, the disk-blackbody component, log-parabolic component fitted with the 4th spectrum, respectively.

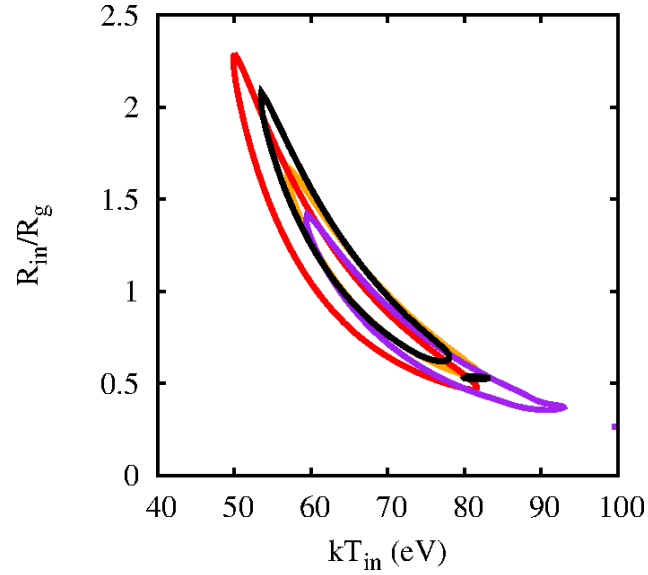


Figure 5.7: 90% confidence contours for the disk inner radius normalized by the gravitational radius versus the disk inner temperature. The orange, red, purple, and black colors represent the observation ID (Orange:1st, Red:2nd, Purple:3rd, Black:4th).

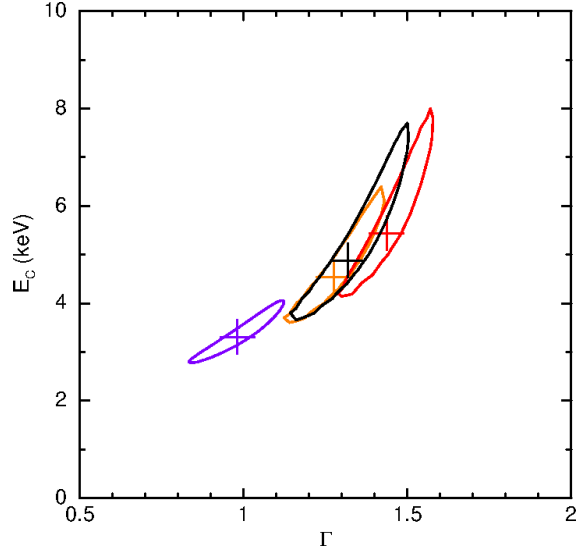


Figure 5.8: 90% confidence contours for the cutoff energy E_C versus the photon index Γ . The same colors as figure 5.7 are used.

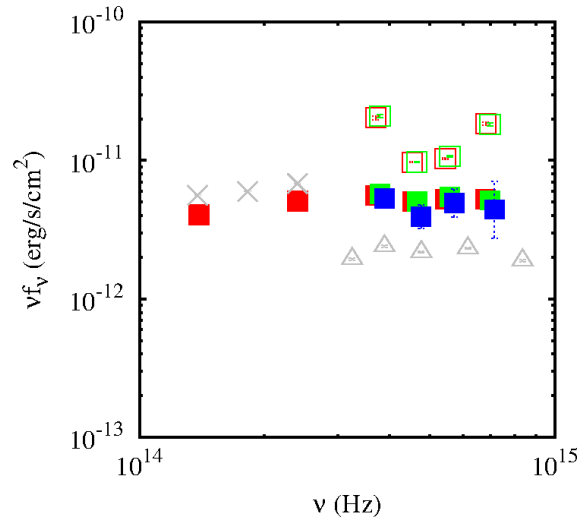


Figure 5.9: Near infrared to Optical SED of RX J1633+4718. Red, green, and blue squares are the 2012/01, 2012/02, and 2012/10 observational data with Kanata, respectively. Opened and filled squares are before/after correct calibration of Kanata, respectively. Gray crosses and triangles are 2MASS and SDSS(PSF) data, respectively.

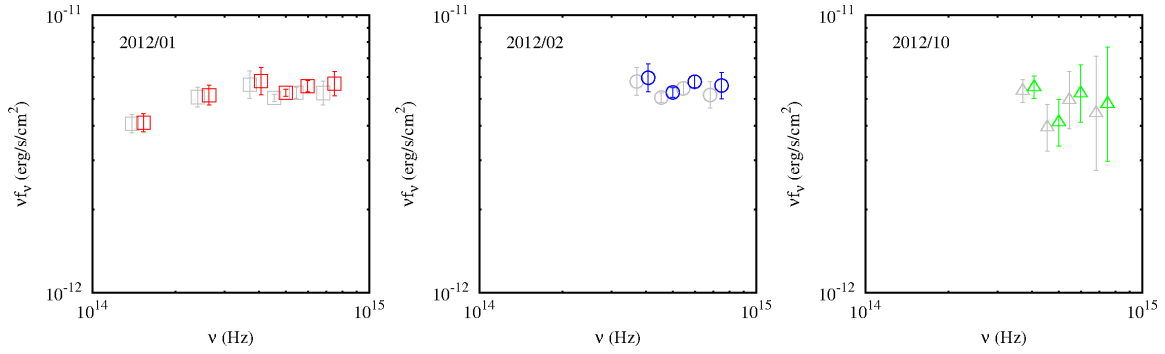


Figure 5.10: Near-infrared to optical spectra of RX J1633+4718 observed with Kanata. Gray data points are the same as figure 5.9. The colored data points are the spectra with taking into the galactic extinction. The squares, circles, and triangles represent the data of 2012/01, 2012/02, and 2012/10, respectively.

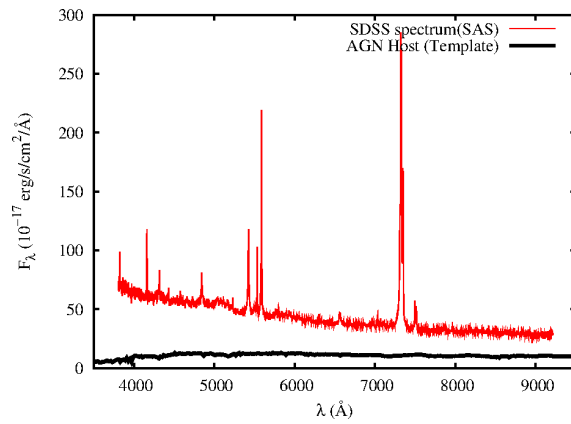


Figure 5.11: SDSS spectrum of RX J1633+4718. The red spectrum shows the rest-frame spectrum. The black curves shows the host-galaxy component of RX J1633+4718 combining the 6 spiral templates supplied by SWIRE library.

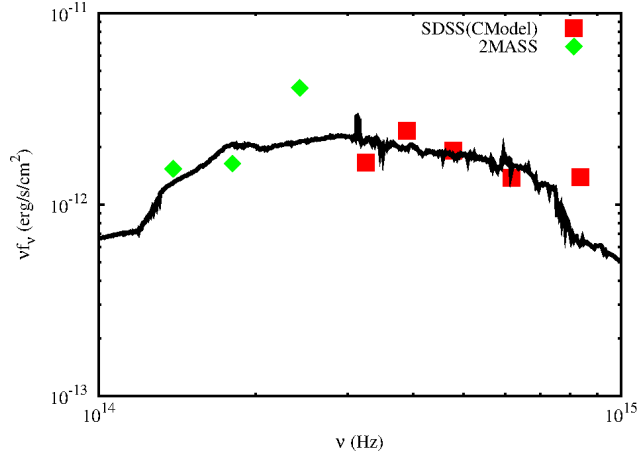


Figure 5.12: Near infrared to optical SED of starburst galaxy, SDSS J163323.53+471902.7. Red squares and green diamonds are the SDSS data and 2MASS data, respectively.

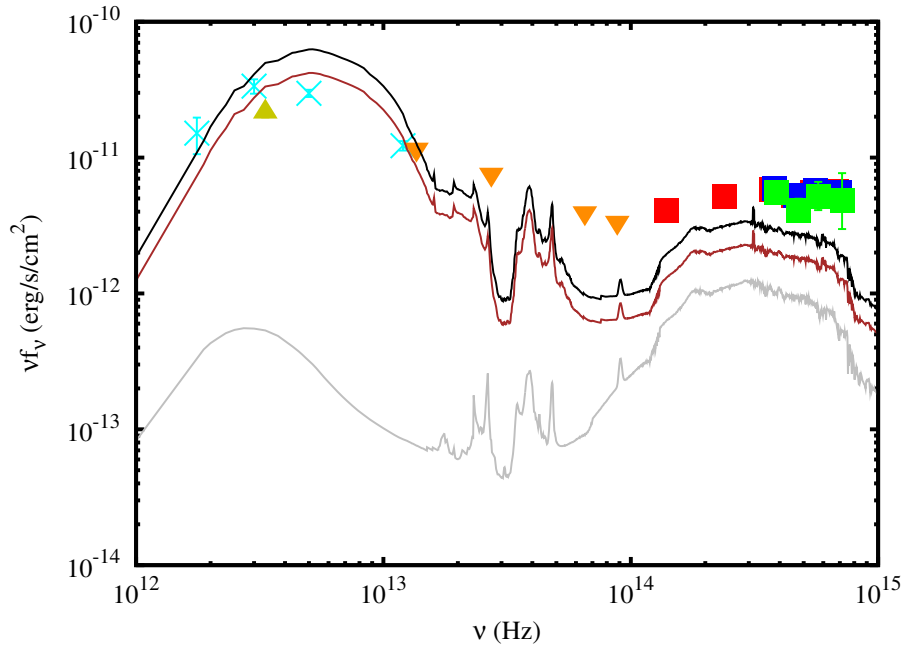


Figure 5.13: Far infrared to optical SED of RX J1633+4718 and the templates flux of both RX J1633+4718 and SDSS J163323.53+471902.7. Red, blue and green squares represent the Kanata data in 2012/01, 2012/02, and 2012/10, respectively. Orange down-triangles are the WISE data points. The IRAS and AKARI data points are represented in cyan crosses and yellow up-triangles data, respectively. The host-galaxy components of RX J1633+4718 and SDSS J163323.53+471902.7 are shown in gray and brown solid line, respectively. The black solid line is the sum of RX J1633+4718 and SDSS J163323.53+471902.7 host-galaxy components.

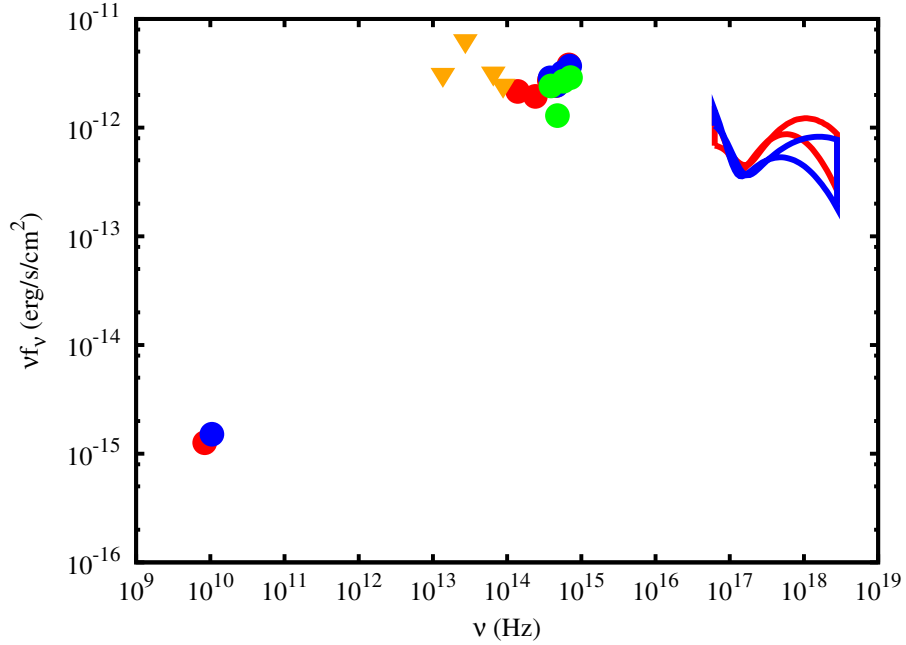


Figure 5.14: Radio to X-ray SED of RX J1633+4718. The host-galaxy components of RX J1633+4718 and SDSS J163323.53+471902.7 are subtracted. Red, blue circles or curves are the data in 2012/01, 2012/02, respectively. While green data points are the one in 2012/10, orange down-triangles are the same as those in figure 5.13.

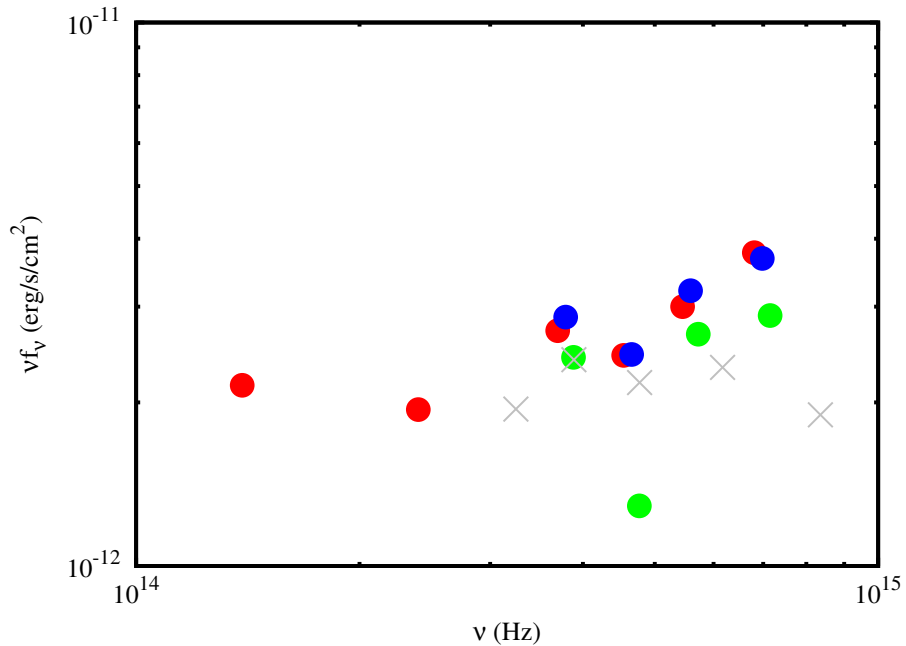


Figure 5.15: Near infrared to optical spectrum of RX J1633+4718 subtracted the both host-galaxy components. While red, blue, green data points are the Kanata observational data, the gray crosses are the SDSS (PSF) spectrum.

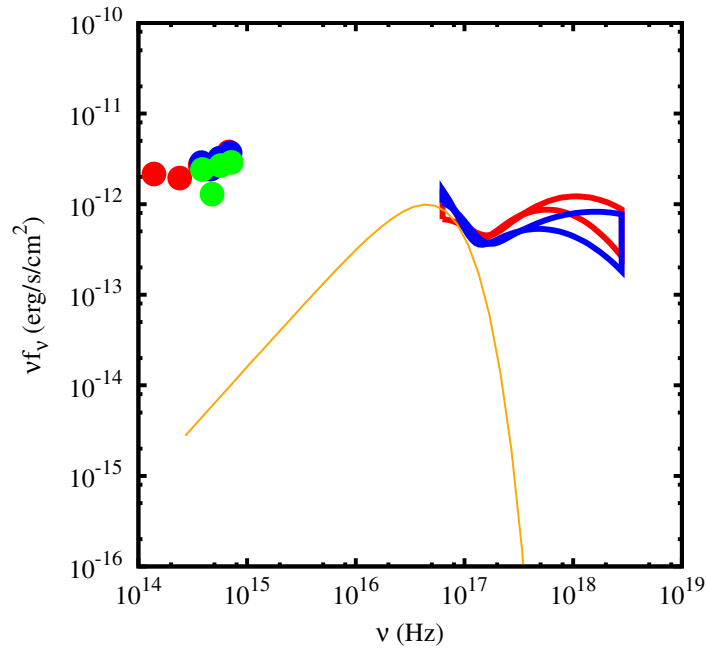


Figure 5.16: Optical to X-ray SED of RX J1633+4718. Red:2012/01, Blue:2012/02, Orange solid line:disk-blackbody model assuming $kT_{in} = 78$ eV, $p = 0.75$, and $R_{in} = 0.6R_g$, $M_{BH} = 3 \times 10^6 M_{\odot}$, $\theta = 30^\circ$, respectively.

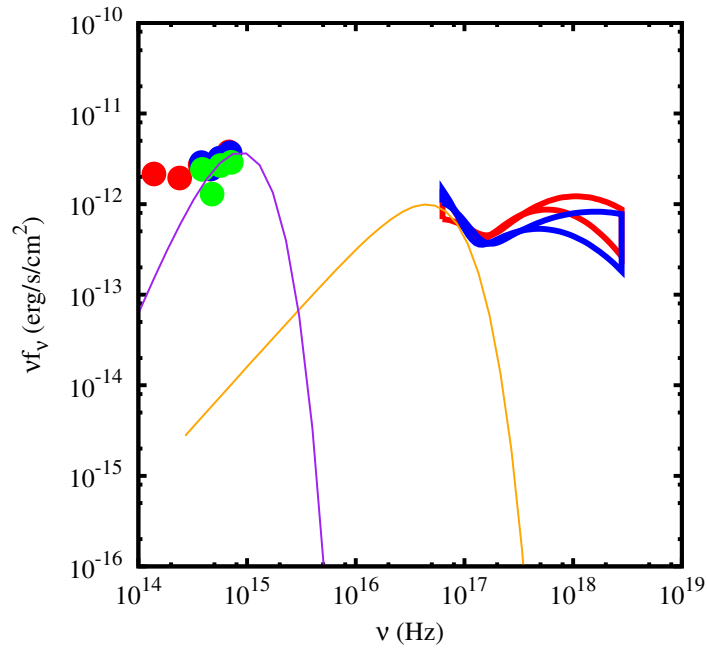


Figure 5.17: The same figure as figure 5.16, but we add the single blackbody model (purple) which temperature is 1 eV.

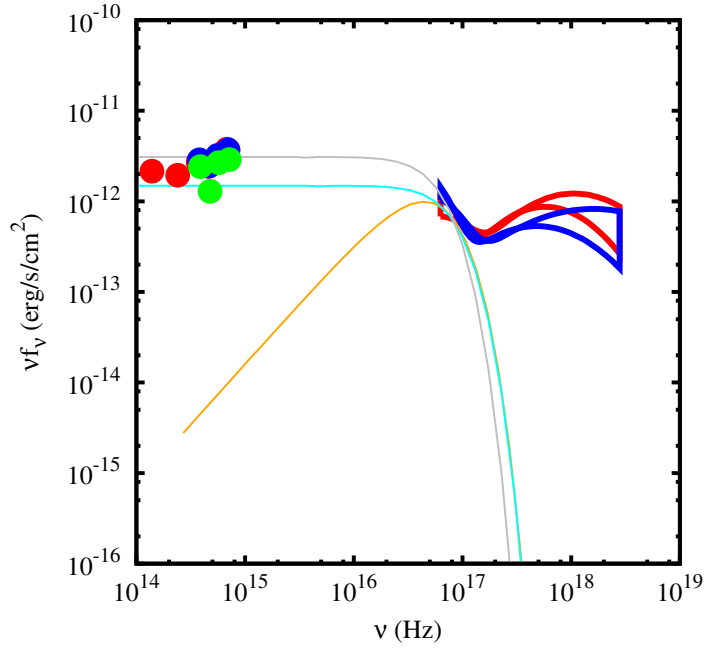


Figure 5.18: The same figure as figure 5.16, but we add the disk blackbody model, which is accretion disk, powerlaw dependence for $T(r)$ (cyan). We assume the disk inner temperature, radius, and the radial dependence of the disk temperature (p , where $T \propto r^{-p}$) are 86 eV, $0.3 R_g$, and 0.5, respectively. The gray solid curve is the upper limit of the disk blackbody model which is powerlaw dependence for $T(r)$ at 90% confidence level.

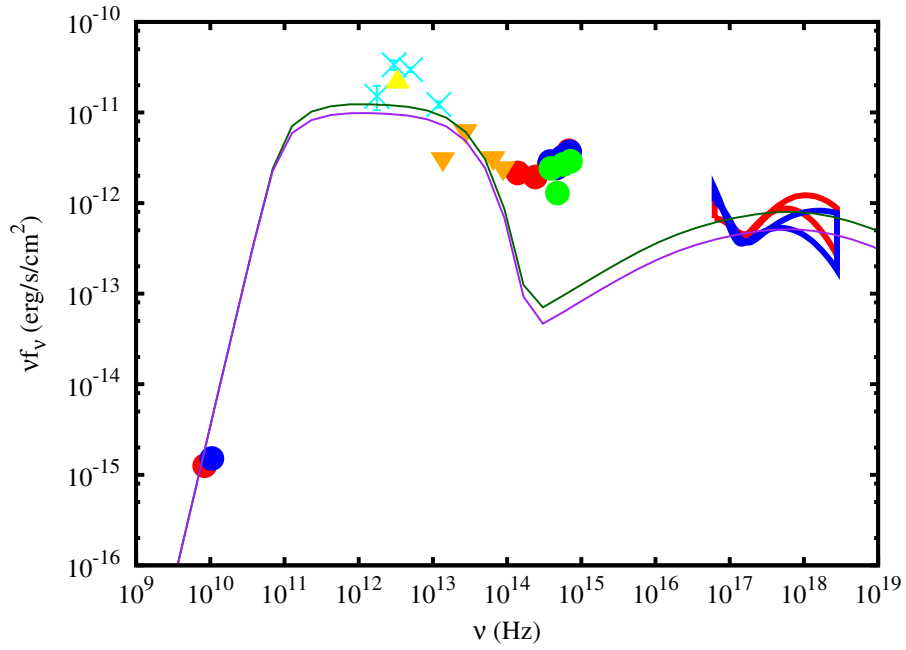


Figure 5.19: Radio to X-ray SED of RX J1633+4718. In the near-infrared and optical band, we subtracted the host galaxy components of RX J1633+4718 and starburst galaxy. Red, blue and green squares represent the Kanata data in 2012/01, 2012/02, and 2012/10, respectively. Orange down-triangles are the WISE data points. The IRAS and AKARI data points are represented in cyan crosses and yellow up-triangles data, respectively. The input parameters are listed in table 5.9.

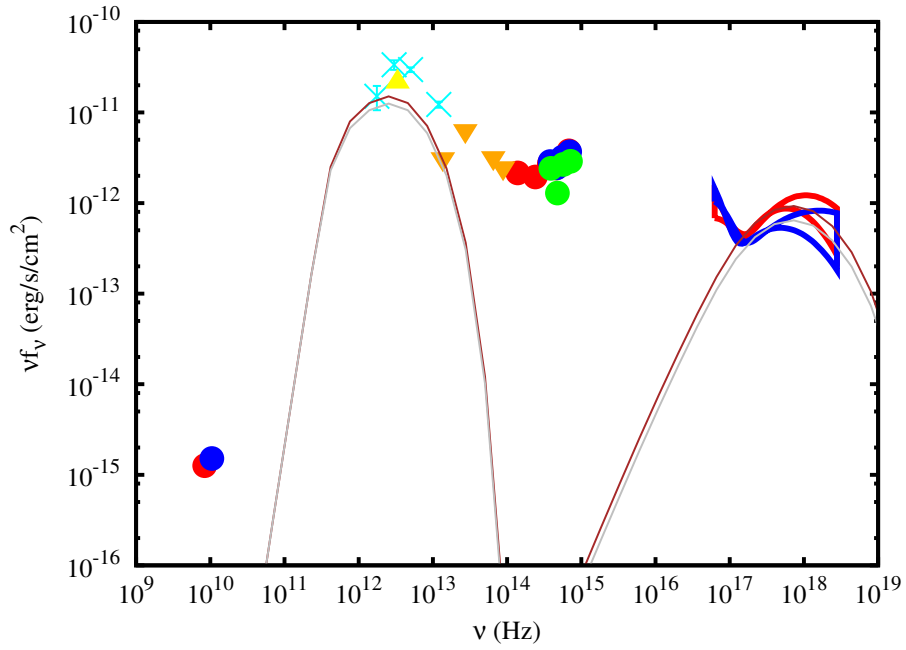


Figure 5.20: Radio to X-ray SED of RX J1633+4718. In the near-infrared and optical band, we subtracted the host galaxy components of RX J1633+4718 and starburst galaxy. Red, blue and green squares represent the Kanata data in 2012/01, 2012/02, and 2012/10, respectively. Orange down-triangles are the WISE data points. The IRAS and AKARI data points are represented in cyan crosses and yellow up-triangles data, respectively. The input parameters are listed in table 5.10.

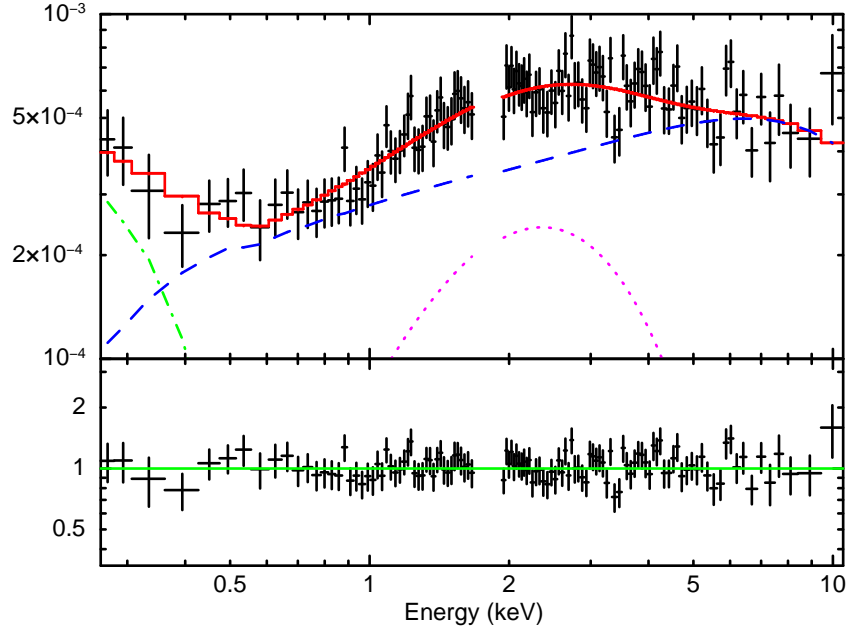


Figure 5.21: The 0.25–12 keV spectrum and the best-fit model with two Comptonization of soft photons in a hot plasma (`compTT`) and a disk blackbody. The unfolded spectrum in the form of $E^2 I(E)$ is displayed. Black points with error bars are the data from the XIS. The XIS-BI spectrum above 1.9 keV and the XIS-FI spectrum below 1.7 keV are not displayed for clarity. The total model curve is plotted in a red line. The magenta dotted line and blue dashed line are the Comptonization models for the soft X-ray excess component and hard curvature component (magenta: $kT_e = 0.64^{+0.26}_{-0.05}$ keV, blue: $kT_e = 2.7^{+188.0}_{-0.7}$ keV), respectively. The green dot-dashed line shows the disk blackbody model ($kT_{in} = 53^{+26}_{-30}$ eV). The bottom panel shows the data/model ratio.

Table 5.1: Suzaku observation log of RX J1633+4718

Obs_ID	Start(UT)	Stop(UT)	XIS exposures (ks)
706027010	2011 Jul 01 19:41:23	2011 Jul 02 20:18:15	34
706027020	2011 Jul 18 12:06:54	2011 Jul 19 10:30:12	38
706027030	2012 Jan 13 20:59:37	2012 Jan 14 19:56:16	38
706027040	2012 Feb 05 16:16:04	2012 Feb 06 18:00:21	35

Table 5.2: VLBI observation log of RX J1633+4718

Obs_ID	u12016a	u12037a
Observation Date	2012/01/16	2012/02/06
Time (UT)	01:00-03:00	00:00-02:00
Telescope	Yamaguchi32 m, Hitachi32 m	
Observing frequency (MHz)	IF1:8400-8416, IF2:8432-8448	

Table 5.3: Kanata observation log of RX J1633+4718

Observation Date	2012/01/16	2012/02/04	2012/10/16
Time (UT)	18:30-19:30		
Instrument	HOWPol	HOWNIR	HOWPol
aperture radius	9.0''	5.8''	9.0''
Band	Exposure Time (s)		
<i>B</i>	600	...	600
<i>V</i>	240	...	360
<i>R_C</i>	240	...	240
<i>I_C</i>	480	...	240
<i>J</i>	...	600	...
<i>K_s</i>	...	600	...

Table 5.4: Kanata observation results

Band	Magnitude (in units of Vega)		
	2012/01/16	2012/02/04	2012/10/16
<i>B</i>	16.79 ± 0.11	16.81 ± 0.12	16.98 ± 0.51
<i>V</i>	16.43 ± 0.05	16.39 ± 0.06	16.50 ± 0.26
<i>R_C</i>	16.09 ± 0.03	16.08 ± 0.04	16.36 ± 0.21
<i>I_C</i>	15.49 ± 0.12	15.46 ± 0.12	15.54 ± 0.10
<i>J</i>	14.72 ± 0.09
<i>K_s</i>	13.40 ± 0.08

Table 5.5: The galactic extinction determined in Schlafly & Finkbeiner (2011). Column(1):Bandpass observed with Kanata. Column(2):wavelength. Column(3):Relative extinction to $E(B - V)$. Column(4):The extinction at each wavelength assuming $R_V = 3.1$.

Band	λ (μm)	$A_{\text{Band}}/E(B - V)$	A_{Band} (mag)
(1)	(2)	(3)	(4)
B	0.44	2.971	0.084
V	0.55	2.118	0.060
R_C	0.66	1.606	0.045
I_C	0.81	1.177	0.033
K_s	1.25	0.610	0.017

Table 5.6: Near infrared to Optical flux of SDSS J163323.53+471902.7.

Band	ν [10^{14} Hz]	νf_ν [10^{-13} erg/s/cm ²]	Instrument
u	8.36	2.38	SDSS
g	6.17	4.12	SDSS
r	4.77	5.20	SDSS
i	3.89	6.85	SDSS
z	3.25	5.92	SDSS
j	2.43	40.59	2MASS
h	1.80	16.34	2MASS
k	1.39	15.35	2MASS

Table 5.7: Spectral fit to the time averaged in the 0.25–12 keV spectra of RX K1633+4718

Model	parameter	1 st	2 nd	3 rd	4 th
diskbb	kT_{in} [eV]	63 ± 10	59^{+13}_{-14}	60^{+16}_{-15}	62^{+12}_{-11}
cutoffpl	Γ	1.3 ± 0.1	1.5 ± 0.1	1.0 ± 0.1	$1.3^{+0.1}_{-0.2}$
	E_C [keV]	$4.5^{+1.4}_{-0.9}$	5^{+2}_{-1}	$3.3^{+0.5}_{-0.4}$	5^{+2}_{-1}
	χ^2/dof	171.90/158	193.52/166	195.47/208	137.91/136
diskbb	kT_{in} [eV]	70 ± 10	66^{+13}_{-12}	78^{+18}_{-15}	68^{+13}_{-11}
logpar	$\Gamma_{1\text{keV}}$	1.4 ± 0.1	1.5 ± 0.10	1.1 ± 0.1	1.4 ± 0.1
	$b(\text{curvature})$	0.67 ± 0.15	0.6 ± 0.1	1.0 ± 0.1	0.6 ± 0.2
	χ^2/dof	165.89/158	188.78/166	184.94/208	134.54/136
diskbb	kT_{in} [eV]	60 ± 11	70^{+17}_{-15}	62^{+19}_{-16}	60 ± 12
bknpow	Γ_1	$1.56^{+0.07}_{-0.23}$	1.3 ± 0.2	$1.23^{+0.10}_{-0.11}$	1.5 ± 0.1
	E_{break} [keV]	$2.6^{+0.1}_{-0.2}$	$1.3^{+0.2}_{-0.1}$	2.1 ± 0.2	$2.3^{+0.6}_{-0.4}$
	Γ_2	$2.2^{+0.3}_{-0.8}$	2.03 ± 0.05	$2.17^{+0.08}_{-0.07}$	$2.2^{+0.2}_{-0.1}$
	χ^2/dof	168.51/157	190.94/165	181.90/207	131.59/135
powerlaw	Γ	$5.4^{+1.3}_{-0.8}$	6^{+2}_{-1}	$5.7^{+1.4}_{-1.0}$	$5.4^{+1.2}_{-0.8}$
cutoffpl	Γ	$1.25^{+0.15}_{-0.17}$	1.4 ± 0.1	1.0 ± 0.1	1.3 ± 0.2
	E_C [keV]	$4.4^{+1.5}_{-0.9}$	5^{+2}_{-1}	$3.2^{+0.6}_{-0.4}$	5^{+2}_{-1}
	χ^2/dof	177.04/158	196.01/166	196.48/209	139.47/136
powerlaw	Γ	$4.6^{+0.9}_{-0.7}$	$4.9^{+1.3}_{-0.9}$	$4.4^{+0.8}_{-0.7}$	$4.7^{+0.8}_{-0.7}$
logpar	$\Gamma_{1\text{keV}}$	1.2 ± 0.2	$1.4^{+0.1}_{-0.2}$	0.9 ± 0.2	$1.2^{+0.2}_{-0.3}$
	$b(\text{curvature})$	0.8 ± 0.2	0.6 ± 0.2	1.1 ± 0.2	$0.8^{+0.3}_{-0.2}$
	χ^2/dof	170.28/158	191.55/166	182.97/208	134.16/136
	Γ	6^{+2}_{-1}	$4.5^{+1.3}_{-0.9}$	5^{+2}_{-1}	$5.3^{+1.2}_{-0.9}$
bknpow	Γ_1	$1.55^{+0.08}_{-0.47}$	$1.1^{+0.3}_{-0.5}$	$1.2^{+0.1}_{-0.2}$	$1.5^{+0.1}_{-0.3}$
	E_{break} [keV]	$2.5^{+0.3}_{-0.9}$	1.4 ± 0.1	2.0 ± 0.2	2.3 ± 0.5
	Γ_2	$2.2^{+0.1}_{-0.2}$	2.01 ± 0.06	$2.17^{+0.08}_{-0.07}$	$2.2^{+0.2}_{-0.1}$
	χ^2/dof	172.79/157	192.13/165	180.02/207	132.24/135

Table 5.8: The best-fitting parameters for 0.25–12 keV data modeled with a p -free disk model (diskpbb in Xspec) and a log-parabolic (logpar in Xspec). We used the 2012/01 and 2012/02 semi simultaneous data from Near infrared to X-ray.

parameter	3 rd	4 th
kT_{in} [eV]	86^{+23}_{-18}	73^{+16}_{-13}
p	0.5(fix)	
K	633^{+2129}_{-485}	1883^{+4921}_{-1330}
$\Gamma_{1\text{keV}}$	1.0 ± 0.1	$1.38^{+0.13}_{-0.14}$
$b(\text{curvature})$	1.0 ± 0.1	$0.63^{+0.19}_{-0.18}$
$L_{\text{bol}}[10^{45} \text{ erg s}^{-1}]$	1.2	1.6
χ^2/dof	183.93/208	134.14/136

Table 5.9: Parameters used to the models described in figure 5.19.

Parameter	2012/01	2012/02
G		10
θ		5
$B[\text{G}]$		0.175
$R[\text{pc}]$		0.03
$d[\text{erg cm}^{-3}]$	0.0125	0.01
$\log(E_{min}/eV)$		3.5
$\log(E_{max}/eV)$		9
$\log(E_{br}/eV)$		8
p_1		2
p_2		3

Table 5.10: Parameters used to the models described in figure 5.20.

Parameter	2012/01	2012/02
G		10
θ		5
$B[\text{G}]$		0.4
$R[\text{pc}]$		0.01
$d[\text{erg cm}^{-3}]$	0.009	0.0075
$\log(E_{min}/eV)$		8.15
$\log(E_{max}/eV)$		8.5
p		4.1

Table 5.11: The best-fit parameters of the 2 Comptonization models and the disk blackbody model.

parameter	best-fit value
$kT_{in}[\text{eV}]$	53_{-30}^{+26}
$kT_{e1}[\text{keV}]$	$2.7_{-0.7}^{+188.0}$
τ_1	7_{-4}^{+8}
$kT_{e2}[\text{keV}]$	$0.64_{-0.05}^{+0.26}$
τ_2	199_{-185}^{+0}
χ^2/dof	179.93/205

Chapter 6

Summary

We have studied Suzaku observations of Narrow Line Seyfert 1 Galaxies (NLS1s). Among the various X-ray spectral components in radio quiet AGNs, our main interest is on its primary emission, i.e., power-law component and soft thermal emission from accretion disk. NLS1s sources could be good example of high accretion state of SMBHs.

We first presented the results from Suzaku observation of the luminous NLS1, Ton S180. We obtained wide-band (0.25–55 keV) X-ray spectra for the first time and found the broad iron K line centered at 6.7 keV. We reproduce the soft X-ray excess component with a combination of the reflection model and the disk blackbody model. The inner disk temperature is obtained as 75 eV, which is much lower than previously considered, and a general problem that the disk temperature derived from a soft X-ray excess is too high is reconciled, at least in this source.

We next studied three hard X-ray bright NLS1s with Suzaku. Measurement of the high energy cutoff in a power-law component is the aim of our observations. Among three, Mrk 110 and SWIFT J212745.6+565636 show the cutoff energies of 20–100 keV, which is significantly smaller than typical values of 100–300 keV for BLS1s, although IGR J16185–5928 in our sample shows a cutoff energy higher than 240 keV. We show a trend that NLS1s (high accretion rate sources) have lower cutoff energies, i.e., electron temperatures of accretion corona, than BLS1s. In the framework of thermal Comptonization in a corona, this is interpreted as shorter cooling time at higher accretion rate.

We then performed quasi-simultaneous radio, optical, and X-ray observations of the radio loud NLS1 RX J1633+4718. The X-ray spectra are explained with two components; one is soft X-ray thermal component and the

other is a power-law component but with a cutoff energy of 3–5 keV. The former component and optical emission are simultaneously reproduced with a p -disk model of $p \sim 0.5$, which represents a slim disk. The luminosity of this component is super Eddington as is seen in some ULX sources, but for the first time in AGNs. On the other hand, the power-law with a cutoff component is difficult to explain with a SSC model unless electrons are mono-energetic. We hence interpret this component with thermal Comptonization in a corona, but with extremely low electron temperature. We speculate this source is an extreme case of NLS1 (i.e. high accretion rate) class. In this source reflection component is not apparent and the thermal disk component is observed in its bare form. These might be related the production of jets in this source.

These X-ray (and partly optical and radio) observations of NLS1s sources have provided unique opportunity to examine SMBH radiating at high accretion rate. The key results of our observations are summarized in figure 6.1, 6.2, 6.3, 6.4, and 6.5. These figures include the data of Ton S180 and RX J1633+4718 in addition to the plots discussed in chapter 4. From figure 6.1, it is clear that RX J1633+4718 is obviously special case among NLS1s. Figure 6.2–6.4 show that while the electron temperature of NLS1 is lower than that of BLS1, the Compton y parameter does not differ significantly. For the optical depth τ , it is seen that NLS1 has slightly higher optical depth than BLS1.

In order to examine statistically, we calculate the weighted means of these parameters. When we calculated them by the same way described in chapter 4, we obtained the following results. For the electron temperature, the weighted mean of NLS1 (including Ton S180 and RX J1633+4718) is lower ($\langle kT_e \rangle = 1.6 \pm 0.1$ keV) than that of BLS1 ($\langle kT_e \rangle = 22 \pm 3$ keV). Even if we exclude the data of RX J1633+4718, the weighted mean of NLS1 is $\langle kT_e \rangle = 10 \pm 2$ keV and remains lower than that of BLS1. For the Compton y parameter, the weighted means of NLS1 and BLS1 are $\langle y \rangle_{\text{NLS1}} = 0.83 \pm 0.02$ (including RX J1633+4718) and $\langle y \rangle_{\text{BLS1}} = 0.97 \pm 0.03$, respectively. The difference between NLS1 and BLS1 is not clearly seen. For the optical depth τ , NLS1 is $\langle \tau \rangle_{\text{NLS1}} = 4.9 \pm 0.4$ (including RX J1633+4718) and BLS1 $\langle \tau \rangle_{\text{BLS1}} = 1.9 \pm 0.4$, respectively. This is because RX J1633+4718 has high optical depth of about 10. When we exclude the data of RX J1633+4718, the weighted mean of NLS1 becomes $\langle \tau \rangle_{\text{NLS1}} = 2.8 \pm 0.4$, which is slightly higher than that of BLS1. Thus, we statistically confirm that the weighted

mean electron temperature kT_e of NLS1 is significantly lower than that of BLS1. For the Compton y parameter, the difference is not clearly seen between NLS1 and BLS1. The optical depth τ of NLS1 is slightly higher than that of BLS1 if we exclude RX J1633+4718. We summarize the means and weighted means of NLS1 and BLS1 in table 6.1.

We summarize the observational properties of NLS1s compared with BLS1 as follows:

- (1) High Eddington ratio close to or above the Eddington ratio,
- (2) Small luminosity ratio L_X/L_{UV} ,
- (3) Low electron temperature kT_e of the accretion corona.

(1) means that NLS1 has a higher accretion rate than BLS1. (2) indicates that the disk inner radius of NLS1 is smaller than the innermost stable circular orbit (ISCO) and the disk inner temperature is higher than that predicted from the standard accretion disk model. These indications might be caused by the high accretion rate. Since the photon energy density from the accretion disk gets larger for increasing the accretion rate as discussed in chapter 4, the luminosity of NLS1 irradiating the corona is higher than that of BLS1. This causes the corona of NLS1 to cool more efficiently than BLS1, owing to the Compton cooling. The cooler corona produces few hard X-ray photons, leading to (3). For the accretion corona, as discussed in chapter 4, it should be localized to explain the rapid X-ray variability. This assumption is able to explain the detection of the bare disk emission of RX J1633+4718.

From the above indications, we suggest that the central region of NLS1 as follows. Since NLS1 has the high accretion rate close to or above the Eddington ratio, the central advection-dominated accretion flow (ADAF) zone disappears (Narayan, 1996; Esin et al., 1997) and the disk becomes slim disk (Watarai et al., 2000). The accretion corona is not homogeneous but localized above the disk. The central state of NLS1 is similar to the very high state of BH X-ray binary. For RX J1633+4718, which is an extreme case, the height of disk is larger than that of normal NLS1. From a few keV electron temperature and no reflection component, the accretion corona is more localized. This might be because the production of the jets suppresses the activity of the corona.

Table 6.1: The mean and weighted mean of kT_e , y , and τ for NLS1s and BLS1s.

Parameter	NLS1		BLS1	
	mean	weighted mean	mean	weighted mean
	Including RX J1633+4718			
kT_e [keV]	34 ± 11	1.6 ± 0.2	60 ± 10	22 ± 3
y	0.94 ± 0.07	0.83 ± 0.02	1.12 ± 0.02	1.27 ± 0.06
τ	4.9 ± 0.4	5.9 ± 0.3	2.2 ± 0.3	1.9 ± 0.3
	Excluding RX J1633+4718			
kT_e [keV]	53 ± 17	11 ± 2
y	0.87 ± 0.06	0.83 ± 0.02
τ	2.8 ± 0.6	2.3 ± 0.4

6.1 Future Prospects

We have obtained hard X-ray spectra of NLS1s from 5 sources and found some trends with employing BLS1 data. Apparently we need more sample for the NLS1, hopefully with higher accuracy. That will be possible with new generation hard X-ray telescope such as NuStar and ASTRO-H. ASTRO-H is also good for simultaneous observations of soft X-ray high resolution spectrum. Although the accretion corona is assumed to be fully ionized, inhomogeneous flow might cause cooler component and some absorption features might be observed.

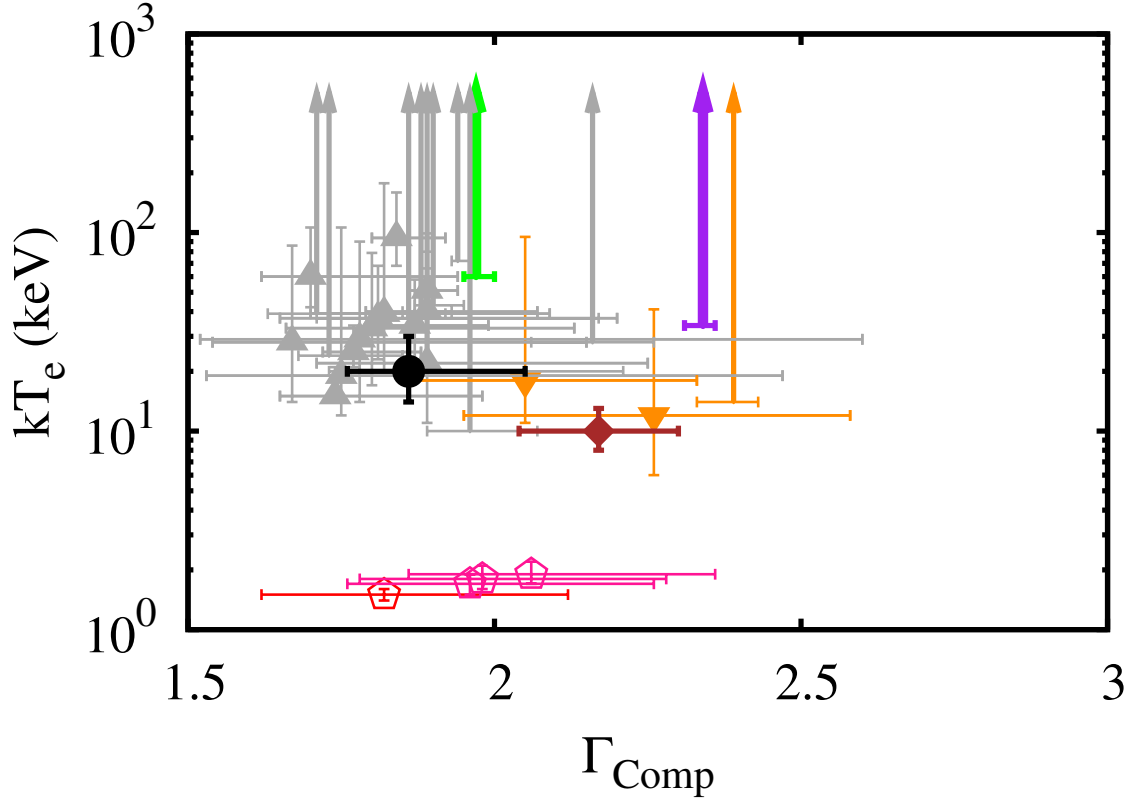


Figure 6.1: The electron temperature kT_e versus the photon index Γ_{Comp} of the power-law. The black filled circle and the brown filled diamond represent Mrk110 and SWIFT J212745.6+565636, respectively. The points of RX J1633+4718 are shown in red opened pentagon (3^{rd}) and dark-pink opened pentagons (1^{st} , 2^{nd} , 4^{th}). The purple and green arrows show the lower limit of Ton S180 and IGR J16185–5928, respectively. The dark-orange down-triangles are the data of other 2 NLS1s referred from Malizia et al. (2008). The dark-orange upward arrow is the lower limit of IGR J19387–0671 (Malizia et al., 2008). The gray up-triangles, upward-arrows are the data of Molina et al. (2009), lower limit, respectively.

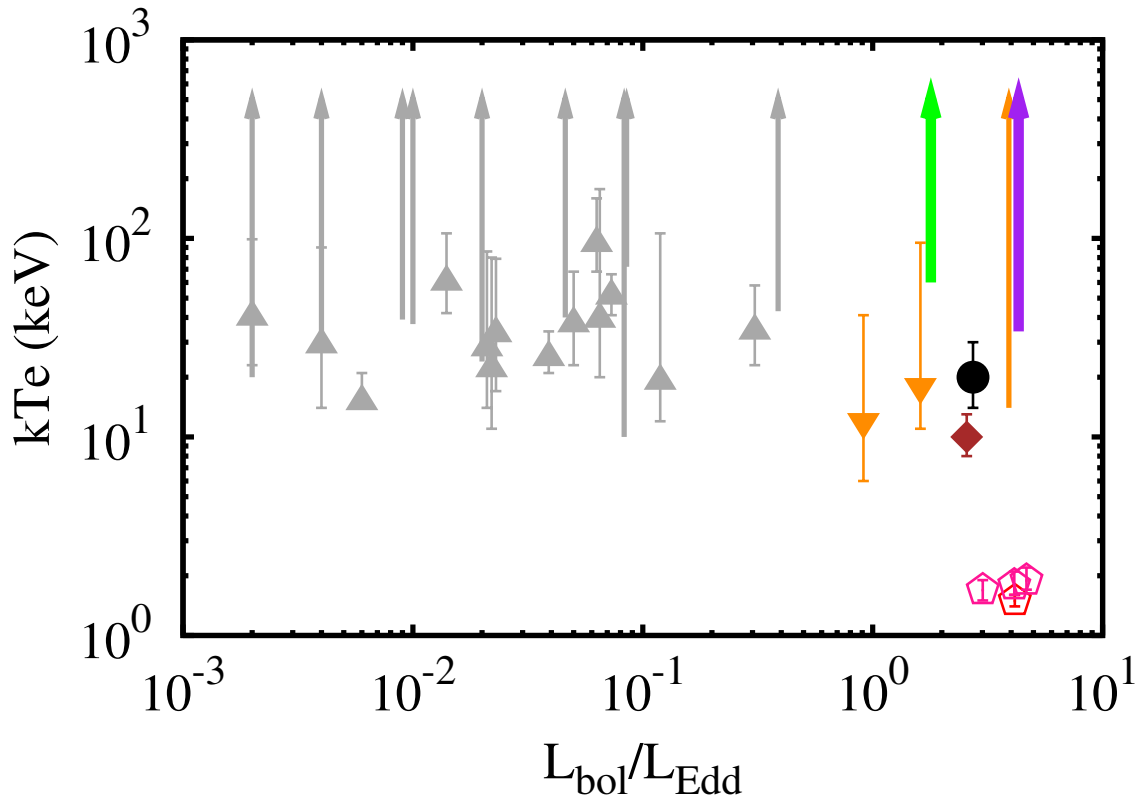


Figure 6.2: The electron temperature kT_e versus the Eddington ratio ($L_{\text{bol}}/L_{\text{Edd}}$) plot for Seyfert 1 galaxies used in this work. The black filled circle and the brown filled diamond represent Mrk 110 and SWIFT J212745.6+565636, respectively. While the 3rd point of RX J1633+4718 is shown in red opened pentagon, the 1st, 2nd, and 4th points are displayed in dark-pink opened pentagons. The purple and green arrows show the lower limit of Ton S180 and IGR J16185–5928, respectively. The dark-orange down-triangles are the data of other 2 NLS1s referred from Malizia et al. (2008). The dark-orange upward arrow is the lower limit of IGR J19387–0671 (Malizia et al., 2008). The gray up-triangles, upward-arrows are the data of Molina et al. (2009), lower limit, respectively.

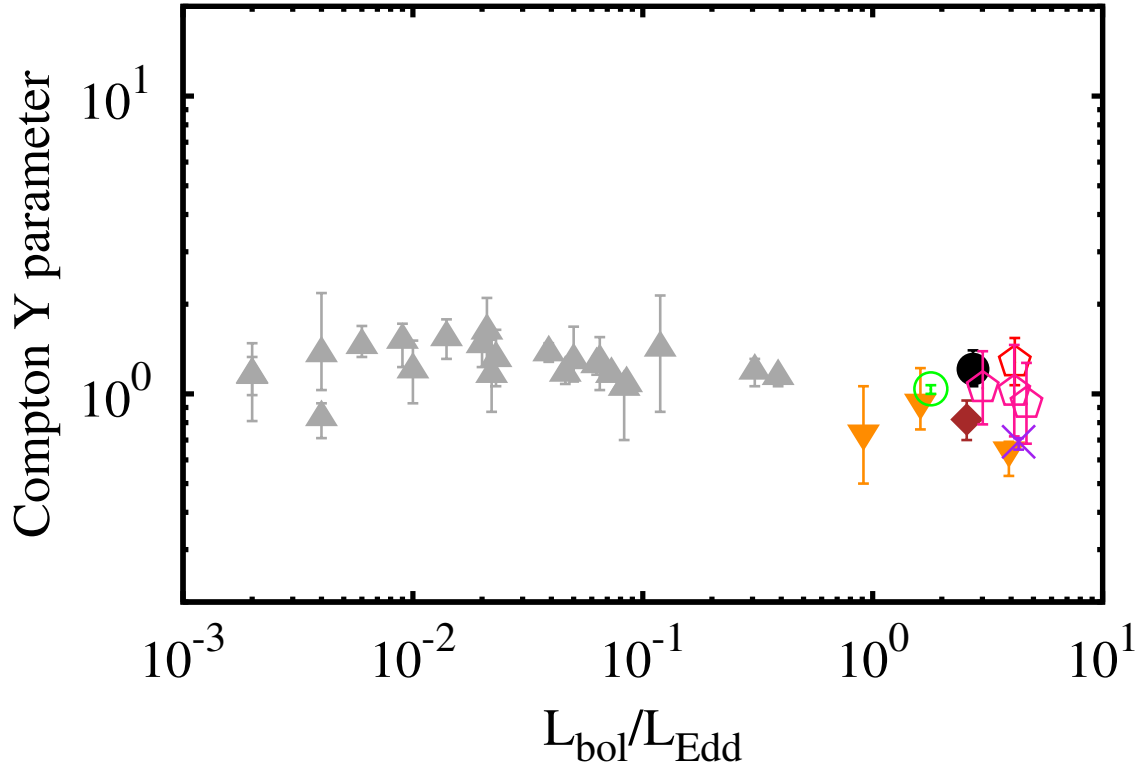


Figure 6.3: The Eddington ratio ($L_{\text{bol}}/L_{\text{Edd}}$) versus the Compton y parameter plot for Seyfert 1 galaxies used in this work. The black filled circle, the blue filled square, and the green opened circle represent Mrk 110, SWIFT J212745.6+565636, and IGR J16185–5928, respectively. The points of Ton S180 is shown in purple cross. The data of RX J1633+4718 is displayed in red opened pentagon (3^{rd}) and dark-pink opened pentagons (1^{st} , 2^{nd} , and 4^{th}), respectively. The dark-orange down-triangles are the data of other NLS1s referred from Malizia et al. (2008). The gray up-triangles are the data of Molina et al. (2009), respectively.

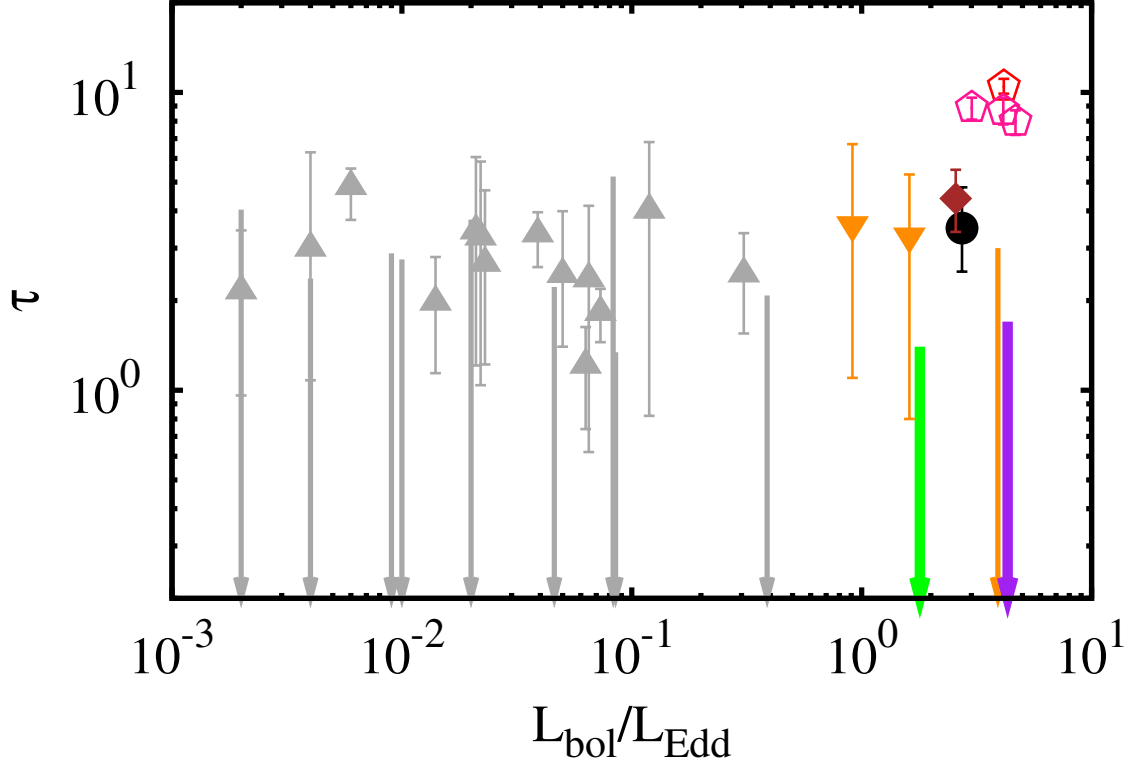


Figure 6.4: The optical depth τ versus the Eddington ratio ($L_{\text{bol}}/L_{\text{Edd}}$) plot for Seyfert 1 galaxies used in this work. The black filled circle and the blue filled diamond represent Mrk 110 and SWIFT J212745.6+565636, respectively. While the 3rd point of RX J1633+4718 is shown in red opened pentagon, the 1st, 2nd, and 4th points are displayed in dark-pink opened pentagons. The purple and green arrows show the lower limit of Ton S180 and IGR J16185–5928, respectively. The dark-orange down-triangles and the dark-orange arrow are the data of other 2 NLS1s and the lower limit of IGR J19387–0671 referred from Malizia et al. (2008). The gray up-triangles and downward-arrows are the data of Molina et al. (2009) and upper limit, respectively.

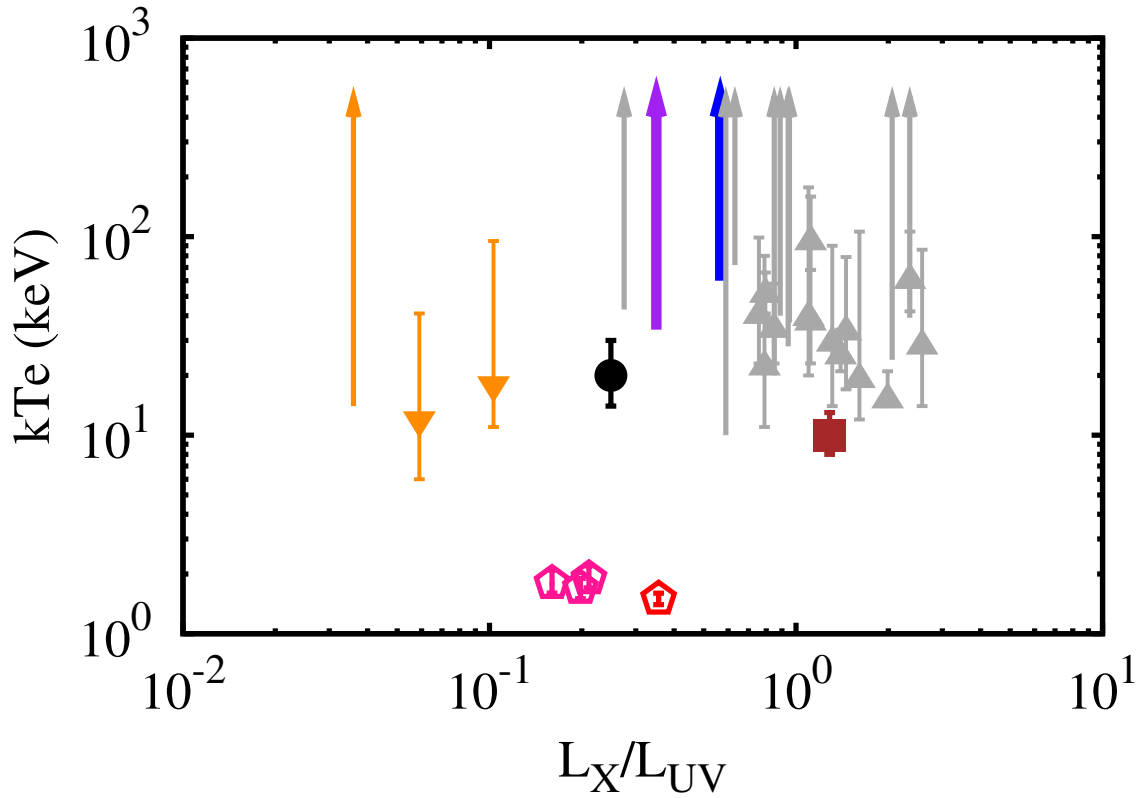


Figure 6.5: The electron temperature kT_e versus the luminosity ratio of L_X/L_{UV} . The black filled circle and the brown filled diamond represent Mrk 110 and SWIFT J212745.6+565636, respectively. While the 3rd point of RX J1633+4718 is shown in red open pentagon, the 1st, 2nd, and 4th points are displayed in dark-pink open pentagons. The purple and green arrows show the lower limit of Ton S180 and IGR J16185–5928, respectively. The dark-orange down-triangles are the data of other 2 NLS1s referred from Malizia et al. (2008). The dark-orange upward arrow is the lower limit of IGR J19387–0671 (Malizia et al., 2008). The gray up-triangles, upward-arrows are the data of Molina et al. (2009), lower limit, respectively.

Acknowledgments

First of all, I would like to thank Prof. Kiyoshi Hayashida (Osaka University) for his advice and comments. He supported my studies for all sides, such as the basic of astrophysics, analysis of active galactic nuclei, calibration of XIS, and statistical considerations. I want to thank Prof. Hiroshi Tsunemi (Osaka University) and Prof. Katsuji Koyama (Kyoto University) as well. They gave various useful advice and comments in the spectral analysis.

I express my gratitude to Prof. Yuichi Terashima (Ehime University) and Prof. Yoshihiro Ueda (Kyoto University). They offered me an opportunity to study 3 NLS1s, Mrk 110, SWIFT J212745.6+565636, and IGR J16185–5928 and provided a lot of useful comments.

I want to give my thanks to Prof. Hiroshi Akitaya (Hiroshima University) and Ryosuke Itoh (Hiroshima University), who are members of Kanata 1.5 m telescope team and Prof. Kenta Fujisawa (Yamaguchi University), who is a member of Japanese VLBI network (JVN) team. They cooperated the quasi-simultaneous observations of RX J1633+4718 and gave us the radio, the near infrared, and the optical data.

I am grateful to Drs. Naohisa Anabuki (Osaka University) and Drs. Hiroshi Nakajima (Osaka University). They held the seminars to be useful for astrophysical study.

I want to thank Prof. Yutaka Fujita (Osaka University) He offered me an opportunity to study the opened cluster Westerlund 2. In this study, I was able to study the Suzaku HXD data analysis and use it to advantage.

Finally, I wish to thank all of members in X-ray Astronomy Group in Osaka University and XIS team.

Bibliography

- Abdo, A. A., Ackermann, M., Ajello, M., et al. 2009a, *ApJ*, 699, 976
- . 2009b, *ApJ*, 707, L142
- Antonucci, R. R. J., & Miller, J. S. 1985, *ApJ*, 297, 621
- Arnaud, K. A., Branduardi-Raymont, G., Culhane, J. L., et al. 1985, *MNRAS*, 217, 105
- Awaki, H., Kunieda, H., Tawara, Y., & Koyama, K. 1991, *PASJ*, 43, L37
- Bachev, R., Grupe, D., Boeva, S., et al. 2009, *MNRAS*, 399, 750
- Baumgartner, W. H., Tueller, J., Markwardt, C., & Skinner, G. 2010, in *Bulletin of the American Astronomical Society*, Vol. 42, AAS/High Energy Astrophysics Division #11, 675
- Beckmann, V., & Shrader, C. R. 2012, *Active Galactic Nuclei*
- Boldt, E. A. 1987, in *NASA Conference Publication*, Vol. 2464, *NASA Conference Publication*, ed. R. Ramaty, T. L. Cline, & J. F. Ormes, 339–378
- Boller, T., Brandt, W. N., & Fink, H. 1996, *A&A*, 305, 53
- Brandt, W. N., Mathur, S., & Elvis, M. 1997, *MNRAS*, 285, L25
- Burwitz, V., Haberl, F., Neuhäuser, R., et al. 2003, *A&A*, 399, 1109
- Calderone, G., Ghisellini, G., Colpi, M., & Dotti, M. 2012, *MNRAS*, 424, 3081
- Comastri, A., Fiore, F., Guainazzi, M., et al. 1998, *A&A*, 333, 31
- Crummy, J., Fabian, A. C., Gallo, L., & Ross, R. R. 2006, *MNRAS*, 365, 1067

Czerny, B., & Elvis, M. 1987, *ApJ*, 321, 305

Czerny, B., Nikołajuk, M., Róžańska, A., et al. 2003, *A&A*, 412, 317

Dadina, M. 2008, *A&A*, 485, 417

D’Ammando, F., Orienti, M., Finke, J., et al. 2012, *MNRAS*, 426, 317

Davis, S. W., Done, C., & Blaes, O. M. 2006, *ApJ*, 647, 525

Dickey, J. M., & Lockman, F. J. 1990, *ARA&A*, 28, 215

Doi, A., Asada, K., & Nagai, H. 2011, *ApJ*, 738, 126

Doi, A., Fujisawa, K., Inoue, M., et al. 2007, *PASJ*, 59, 703

Done, C., Davis, S. W., Jin, C., Blaes, O., & Ward, M. 2012, *MNRAS*, 420, 1848

Done, C., Gierliński, M., Sobolewska, M., & Schurch, N. 2007, in *Astronomical Society of the Pacific Conference Series*, Vol. 373, *The Central Engine of Active Galactic Nuclei*, ed. L. C. Ho & J.-W. Wang, 121

Esin, A. A., McClintock, J. E., & Narayan, R. 1997, *ApJ*, 489, 865

Fabian, A. C., Ballantyne, D. R., Merloni, A., et al. 2002, *MNRAS*, 331, L35

Feng, H., & Kaaret, P. 2007, *ApJ*, 660, L113

Ferrarese, L., & Ford, H. 2005, *Space Sci. Rev.*, 116, 523

Ferrarese, L., & Merritt, D. 2000, *ApJ*, 539, L9

Fink, H. H., Walter, R., Schartel, N., & Engels, D. 1997, *A&A*, 317, 25

Forman, W., Jones, C., Cominsky, L., et al. 1978, *ApJS*, 38, 357

Fukazawa, Y., Mizuno, T., Watanabe, S., et al. 2009, *PASJ*, 61, 17

Gebhardt, K., Kormendy, J., Ho, L. C., et al. 2000, *ApJ*, 543, L5

George, I. M., & Fabian, A. C. 1991, *MNRAS*, 249, 352

Gierliński, M., & Done, C. 2004, *MNRAS*, 349, L7

Graham, A. W. 2008, *ApJ*, 680, 143

- Greisen, E. W. 2003, *Information Handling in Astronomy - Historical Vistas*, 285, 109
- Grupe, D., Komossa, S., Gallo, L. C., et al. 2008, *ApJ*, 681, 982
- Grupe, D., & Mathur, S. 2004, *ApJ*, 606, L41
- Gu, M., & Chen, Y. 2010, *AJ*, 139, 2612
- Gültekin, K., Richstone, D. O., Gebhardt, K., et al. 2009, *ApJ*, 698, 198
- Haardt, F., & Maraschi, L. 1991, *ApJ*, 380, L51
- Hayashida, K. 2000, *New A Rev.*, 44, 419
- Hayashida, K., Miyamoto, S., Kitamoto, S., Negoro, H., & Inoue, H. 1998, *ApJ*, 500, 642
- Hayashida, K., Anabuki, N., Gallo, L., et al. 2007, *Progress of Theoretical Physics Supplement*, 169, 269
- Hua, X.-M., & Titarchuk, L. 1995, *ApJ*, 449, 188
- Ishibashi, W., & Courvoisier, T. J.-L. 2009, *A&A*, 495, 113
- . 2012, *A&A*, 540, L2
- Ishisaki, Y., Maeda, Y., Fujimoto, R., et al. 2007, *PASJ*, 59, 113
- Jin, C., Ward, M., & Done, C. 2012, *MNRAS*, 425, 907
- Kaspi, S., Smith, P. S., Netzer, H., et al. 2000, *ApJ*, 533, 631
- Kato, S., Fukue, J., & Mineshige, S. 2008, *Black-Hole Accretion Disks — Towards a New Paradigm —*
- Kaufmann, S., Wagner, S. J., Tibolla, O., & Hauser, M. 2011, *A&A*, 534, A130
- Kawabata, K. S., Nagae, O., Chiyonobu, S., et al. 2008, in *Society of Photo-Optical Instrumentation Engineers (SPIE) Conference Series*, Vol. 7014, *Society of Photo-Optical Instrumentation Engineers (SPIE) Conference Series*
- Kawabata, R., & Mineshige, S. 2010, *PASJ*, 62, 621

- Kawaguchi, T. 2003, *ApJ*, 593, 69
- Kawanaka, N., Kato, Y., & Mineshige, S. 2008, *PASJ*, 60, 399
- Kazanas, D., Fukumura, K., Behar, E., Contopoulos, I., & Shrader, C. 2012, *The Astronomical Review*, 7, 030000
- Khorunzhev, G. A., Sazonov, S. Y., Burenin, R. A., & Tkachenko, A. Y. 2012, *Astronomy Letters*, 38, 475
- Kokubun, M., Makishima, K., Takahashi, T., et al. 2007, *PASJ*, 59, 53
- Komossa, S., Voges, W., Xu, D., et al. 2006, *AJ*, 132, 531
- Komossa, S., & Xu, D. 2007, *ApJ*, 667, L33
- Koyama, K., Maeda, Y., Sonobe, T., et al. 1996, *PASJ*, 48, 249
- Koyama, K., Tsunemi, H., Dotani, T., et al. 2007, *PASJ*, 59, 23
- Krawczynski, H., Hughes, S. B., Horan, D., et al. 2004, *ApJ*, 601, 151
- Kubo, H., Takahashi, T., Madejski, G., et al. 1998, *ApJ*, 504, 693
- Landolt, A. U. 1992, *AJ*, 104, 340
- Leighly, K. M. 1999a, *ApJS*, 125, 297
- . 1999b, *ApJS*, 125, 317
- Liu, J. Y., Liu, B. F., Qiao, E. L., & Mineshige, S. 2012, *ApJ*, 754, 81
- Lubiński, P., Zdziarski, A. A., Walter, R., et al. 2010, *MNRAS*, 408, 1851
- Lynden-Bell, D. 1969, *Nature*, 223, 690
- Magdziarz, P., & Zdziarski, A. A. 1995, *MNRAS*, 273, 837
- Malizia, A., Bassani, L., Bird, A. J., et al. 2008, *MNRAS*, 389, 1360
- Marshall, H. L. 1994, in *IAU Symposium, Vol. 159, Multi-Wavelength Continuum Emission of AGN*, ed. T. Courvoisier & A. Blecha, 105–110
- Masetti, N., Morelli, L., Palazzi, E., et al. 2006, *A&A*, 459, 21
- Masetti, N., Mason, E., Morelli, L., et al. 2008, *A&A*, 482, 113

- Masetti, N., Parisi, P., Palazzi, E., et al. 2009, *A&A*, 495, 121
- McHardy, I. M., Papadakis, I. E., Uttley, P., Page, M. J., & Mason, K. O. 2004, *MNRAS*, 348, 783
- Merritt, D., & Ferrarese, L. 2001, *ApJ*, 547, 140
- Meyer-Hofmeister, E., Liu, B. F., & Meyer, F. 2012, *A&A*, 544, A87
- Middleton, M., Done, C., & Gierliński, M. 2007, *MNRAS*, 381, 1426
- Miller, L., Turner, T. J., & Reeves, J. N. 2009, *MNRAS*, 399, L69
- Mineshige, S., Hirano, A., Kitamoto, S., Yamada, T. T., & Fukue, J. 1994, *ApJ*, 426, 308
- Mineshige, S., Kawaguchi, T., Takeuchi, M., & Hayashida, K. 2000, *PASJ*, 52, 499
- Miniutti, G., Panessa, F., de Rosa, A., et al. 2009a, *MNRAS*, 398, 255
- Miniutti, G., Ponti, G., Greene, J. E., et al. 2009b, *MNRAS*, 394, 443
- Miniutti, G., Fabian, A. C., Anabuki, N., et al. 2007, *PASJ*, 59, 315
- Mitsuda, K., Bautz, M., Inoue, H., et al. 2007, *PASJ*, 59, 1
- Miyamoto, S., Kitamoto, S., Mitsuda, K., & Dotani, T. 1988, *Nature*, 336, 450
- Miyoshi, M., Moran, J., Herrnstein, J., et al. 1995, *Nature*, 373, 127
- Molina, M., Bassani, L., Malizia, A., et al. 2009, *MNRAS*, 399, 1293
- Murashima, M., Kubota, A., Makishima, K., et al. 2005, *PASJ*, 57, 279
- Mushotzky, R. F. 1984, in *High Energy Astrophysics and Cosmology*, ed. G. F. Bignami & R. A. Sunyaev, 157
- Nandra, K., O'Neill, P. M., George, I. M., & Reeves, J. N. 2007, *MNRAS*, 382, 194
- Narayan, R. 1996, *ApJ*, 462, 136
- Okajima, T., Ebisawa, K., & Kawaguchi, T. 2006, *ApJ*, 652, L105

- Osterbrock, D. E., & Pogge, R. W. 1985, *ApJ*, 297, 166
- Panessa, F., de Rosa, A., Bassani, L., et al. 2011, *MNRAS*, 417, 2426
- Patrick, A. R., Reeves, J. N., Porquet, D., et al. 2011, *MNRAS*, 411, 2353
- Perola, G. C., Matt, G., Cappi, M., et al. 2002, *A&A*, 389, 802
- Peterson, B. M. 1993, *PASP*, 105, 247
- . 1997, *An Introduction to Active Galactic Nuclei*
- Peterson, B. M., McHardy, I. M., Wilkes, B. J., et al. 2000, *ApJ*, 542, 161
- Petrucchi, P. O., Haardt, F., Maraschi, L., et al. 2001, *ApJ*, 556, 716
- Polletta, M., Tajer, M., Maraschi, L., et al. 2007, *ApJ*, 663, 81
- Pounds, K. A., Done, C., & Osborne, J. P. 1995, *MNRAS*, 277, L5
- Qiao, E., & Liu, B. F. 2012, *ApJ*, 744, 145
- Reeves, J., Done, C., Pounds, K., et al. 2008, *MNRAS*, 385, L108
- Reeves, J. N., O'Brien, P. T., Braitto, V., et al. 2009, *ApJ*, 701, 493
- Reid, M. J., Readhead, A. C. S., Vermeulen, R. C., & Treuhaft, R. N. 1999, *ApJ*, 524, 816
- Reynolds, C. S., Fabian, A. C., Brenneman, L. W., et al. 2009, *MNRAS*, 397, L21
- Richards, G. T., Lacy, M., Storrie-Lombardi, L. J., et al. 2006, *ApJS*, 166, 470
- Romano, P., Turner, T. J., Mathur, S., & George, I. M. 2002, *ApJ*, 564, 162
- Ross, R. R., & Fabian, A. C. 2005, *MNRAS*, 358, 211
- Ross, R. R., Fabian, A. C., & Mineshige, S. 1992, *MNRAS*, 258, 189
- Rózańska, A., Czerny, B., Siemiginowska, A., Dumont, A.-M., & Kawaguchi, T. 2004, *ApJ*, 600, 96
- Rybicki, G. B., & Lightman, A. P. 1979, *Radiative processes in astrophysics*

- Salpeter, E. E. 1964, *ApJ*, 140, 796
- Schlafly, E. F., & Finkbeiner, D. P. 2011, *ApJ*, 737, 103
- Seyfert, C. K. 1943, *ApJ*, 97, 28
- Shakura, N. I., & Sunyaev, R. A. 1973, *A&A*, 24, 337
- Shepherd, M. C. 1997, in *Astronomical Society of the Pacific Conference Series*, Vol. 125, *Astronomical Data Analysis Software and Systems VI*, ed. G. Hunt & H. Payne, 77
- Shibata, K. M., Kamenno, S., Inoue, M., & Kobayashi, H. 1998, in *Astronomical Society of the Pacific Conference Series*, Vol. 144, *IAU Colloq. 164: Radio Emission from Galactic and Extragalactic Compact Sources*, ed. J. A. Zensus, G. B. Taylor, & J. M. Wrobel, 413
- Shimura, T., & Takahara, F. 1993, *ApJ*, 419, 78
- Singh, V., Shastri, P., & Risaliti, G. 2011, *A&A*, 533, A128
- Soldi, S., Beckmann, V., Gehrels, N., de Jong, S., & Lubiński, P. 2011, in *Narrow-Line Seyfert 1 Galaxies and their Place in the Universe*
- Stern, B. E., Poutanen, J., Svensson, R., Sikora, M., & Begelman, M. C. 1995, *ApJ*, 449, L13
- Takahashi, H., Hayashida, K., & Anabuki, N. 2010, *PASJ*, 62, 1483
- Takahashi, T., Abe, K., Endo, M., et al. 2007, *PASJ*, 59, 35
- Tanaka, Y., Nandra, K., Fabian, A. C., et al. 1995, *Nature*, 375, 659
- Tazaki, F., Ueda, Y., Ishino, Y., et al. 2010, *ApJ*, 721, 1340
- Terashima, Y., Gallo, L. C., Inoue, H., et al. 2009, *PASJ*, 61, 299
- Titarchuk, L. 1994, *ApJ*, 434, 570
- Titarchuk, L., & Lyubarskij, Y. 1995, *ApJ*, 450, 876
- Tremaine, S., Gebhardt, K., Bender, R., et al. 2002, *ApJ*, 574, 740
- Tsunoda, N., Kubota, A., Namiki, M., et al. 2006, *PASJ*, 58, 1081

- Turner, T. J., George, I. M., & Nandra, K. 1998, *ApJ*, 508, 648
- Turner, T. J., & Miller, L. 2009, *A&A Rev.*, 17, 47
- Turner, T. J., Miller, L., Kraemer, S. B., Reeves, J. N., & Pounds, K. A. 2009, *ApJ*, 698, 99
- Turner, T. J., George, I. M., Yaqoob, T., et al. 2001, *ApJ*, 548, L13
- Turner, T. J., Romano, P., Kraemer, S. B., et al. 2002, *ApJ*, 568, 120
- Uchiyama, H., Ozawa, M., Matsumoto, H., et al. 2009, *PASJ*, 61, 9
- Urry, C. M., & Padovani, P. 1995, *PASP*, 107, 803
- Uttley, P., McHardy, I. M., Papadakis, I. E., Guainazzi, M., & Fruscione, A. 1999, *MNRAS*, 307, L6
- Vaughan, S., Boller, T., Fabian, A. C., et al. 2002, *MNRAS*, 337, 247
- Veledina, A., Vurm, I., & Poutanen, J. 2011, *MNRAS*, 414, 3330
- Véron-Cetty, M.-P., & Véron, P. 2003, *A&A*, 412, 399
- Walter, R., & Fink, H. H. 1993, *A&A*, 274, 105
- Wandel, A., & Petrosian, V. 1988, *ApJ*, 329, L11
- Wang, T., & Lu, Y. 2001, *A&A*, 377, 52
- Watanabe, M., Nakaya, H., Yamamuro, T., et al. 2005, *PASP*, 117, 870
- Watarai, K.-y., Fukue, J., Takeuchi, M., & Mineshige, S. 2000, *PASJ*, 52, 133
- Watson, M. G., Schröder, A. C., Fyfe, D., et al. 2009, *A&A*, 493, 339
- Wisotzki, L., Dreizler, S., Engels, D., Fink, H.-H., & Heber, U. 1995, *A&A*, 297, L55
- Xu, D., Komossa, S., Zhou, H., Wang, T., & Wei, J. 2007, *ApJ*, 670, 60
- Yamada, T. T., Mineshige, S., Ross, R. R., & Fukue, J. 1994, *PASJ*, 46, 553
- Yuan, F., & Zdziarski, A. A. 2004, *MNRAS*, 354, 953
- Yuan, W., Liu, B. F., Zhou, H., & Wang, T. G. 2010, *ApJ*, 723, 508

Yuan, W., Zhou, H. Y., Komossa, S., et al. 2008, ApJ, 685, 801

Zdziarski, A. A., Johnson, W. N., & Magdziarz, P. 1996, MNRAS, 283, 193

Zdziarski, A. A., Poutanen, J., & Johnson, W. N. 2000, ApJ, 542, 703

Zel'dovich, Y. B., & Novikov, I. D. 1964, Soviet Physics Doklady, 9, 246